

CHARACTERIZATION OF SHRINKAGE BEHAVIOR IN CONCRETE MATERIALS
USING CURE REFERENCE METHOD

By

TZU-CHAU CHEN

A DISSERTATION PRESENTED TO THE GRADUATE SCHOOL
OF THE UNIVERSITY OF FLORIDA IN PARTIAL FULFILLMENT
OF THE REQUIREMENTS FOR THE DEGREE OF
DOCTOR OF PHILOSOPHY

UNIVERSITY OF FLORIDA

2009

© 2009 Tzu-Chau Chen

To my dearest parents, wife and son

ACKNOWLEDGMENTS

First of all, I give my heartfelt appreciation to my dear parents for their endless love, support, and encouragement throughout my life. They encourage me to believe in myself, and in my dreams. Their love has meant more than words can express. I dedicate this study especially to them. Also, I would like to express my extreme thanks to my wife for her love and understanding. When I was chained in the lab working on my research or chained to my desk writing the dissertation, she took care of Samuel, our beloved son, and did the house chores.

Moreover, I have my profound appreciation to Dr. Peter Ifju, my mentor, advisor and committee chair, for his guidance and patience throughout my doctoral study. His continued support and insights made this task much easier. And I really appreciate Weiqi Yin, one of the doctoral students in our laboratory, for the automated analysis system he developed. Furthermore, I want to give my thanks to Chris Ferraro and Charles Ishee in FDOT for their financial support and assistance.

Finally, I would like to give my thanks to all other committee members, Dr. Bhavani Sankar, Dr. Nicolae Cristescu, and Dr. Mang Tia, for their valuable suggestions and comments on my research.

TABLE OF CONTENTS

	<u>page</u>
ACKNOWLEDGMENTS	4
LIST OF FIGURES	8
ABSTRACT	12
CHAPTER	
1 INTRODUCTION	14
1.1 Background.....	14
1.2 Literature Review	15
1.2.1 Shrinkage Behavior in Concrete Materials.....	16
1.2.1.1 Autogeneous shrinkage	17
1.2.1.2 Drying shrinkage	18
1.2.2 Experimental Techniques	18
1.2.2.1 Non full-field measurements	19
1.2.2.2 Full-field measurements	19
1.2.3 Numerical Simulation.....	20
1.2.3.1 Moisture diffusion modeling.....	20
1.2.3.2 Shrinkage modeling.....	21
1.2.3.3 Inverse method	21
1.3 Research Objectives.....	23
2 METHODOLOGY	25
2.1 High Sensitivity Moiré Interferometry	25
2.2 Cure Reference Method.....	28
2.2.1 Methodology of CRM	28
2.2.2 Replication of Grating	29
2.2.2.1 Silicone rubber grating based method without epoxy layer	30
2.2.2.2 Aluminized epoxy grating based method.....	30
2.2.2.3 Silicone rubber grating based method with epoxy layer	31
2.3 Automated Fringe Analysis	34
3 SHRINKAGE MEASUREMENTS OF CONCRETE	39
3.1 Introduction.....	39
3.2 Chamber Setup.....	40
3.2.1 Humidity Control.....	40
3.2.2 Temperature Control	41
3.3 Experimental Setups	41
3.3.1 PEMI I.....	41
3.3.2 PEMI II.....	43

3.4	Experimental Results	44
3.4.1	Drying Condition Effect (Temperature and Humidity)	44
3.4.2	W/C ratio and Size Effects	61
3.4.3	Aggregate Effect.....	61
3.4.3.1	Fine aggregate	62
3.4.3.2	Coarse aggregate	67
3.4.4	Autogenous Shrinkage Measurements in Sealed Conditions	70
3.4.4.1	Sealed cement paste specimens	70
3.4.4.2	Sealed mortar specimen	75
3.4.5	Ring Test for Crack Investigation	77
3.4.6	Swelling test	79
3.5	Conclusion & Discussion	80
4	NUMERICAL MODELING	82
4.1	Introduction.....	82
4.2	Model Description	84
4.2.1	Axisymmetric Model.....	84
4.2.2	Materials Properties.....	84
4.2.3	Initial Condition:	84
4.2.4	Boundary Condition	85
4.3	Inverse Method	85
4.4	Validation of Model.....	89
4.4.1	Different Surrounding Humidity	89
4.4.2	Ring Test	92
4.4.3	Square Shape	94
4.4.4	Expansion on Day 1.....	96
4.4.4.1	In-plane deformation measurement.....	96
4.4.4.2	Out-of-plane displacement simulation	98
4.4.5	Reinforced Concrete	98
4.5	Stress Development Prediction.....	103
4.5.1	Free Shrinkage.....	103
4.5.2	Restrained Shrinkage.....	105
4.6	Results and Discussions.....	107
5	CONCLUSIONS & FUTURE WORKS	109
5.1	Conclusions.....	109
5.2	Future Works	110
	APPENDIX: CRM MOIRE FRINGE PATTERNS AND FRINGE ANALAYIS RESULTS ...	112
	LIST OF REFERENCES	118
	BIOGRAPHICAL SKETCH	126

LIST OF TABLES

<u>Table</u>		<u>page</u>
1-1	Categories of concrete materials.....	16
3-1	Substances for RH control.....	41
3-2	Shrinkage measurements under RH=0% and room temperature (23°C).....	58
3-3	Shrinkage measurements under RH=100% and room temperature (23°C).....	59
4-1	Thermal mechanical interaction model.....	83
4-2	Errors of optimization.....	87

LIST OF FIGURES

<u>Figure</u>	<u>page</u>
1-1 Concrete under external restraints	15
1-2 Shrinkage strain components in (a) normal-strength and (b) high-strength concrete (Sakata & Shimomura 2004)	17
2-1 Scheme of moiré interferometer	26
2-2 Schematic diagram of moiré interferometry	27
2-3 (a) Concrete fluid etched aluminum (b) concrete broke during separation	31
2-4 Concrete samples and molds.....	32
2-5 Procedure to prepare diffraction grating	33
2-6 Fringe patterns from the master grating.....	34
3-1 Chamber setup	40
3-2 Experimental setup with PEMI.....	42
3-3 Fringe-shifting stage	42
3-4 Experimental setup with PEMI II	43
3-5 U-field Moiré fringe patterns under 50% RH and 23°C.....	44
3-6 V-field Moiré fringe patterns under 50% RH and 23°C.....	45
3-7 Full-field maps in x-y coordinate for day 2	46
3-8 Full-field maps in polar coordinate for day 2	47
3-9 U-field Moiré fringe patterns under 0% RH and 23°C.....	49
3-10 V-field Moiré fringe patterns under 0% RH and 23°C.....	50
3-11 Full-field maps for day 7 under 0% RH and 23°C	50
3-12 U-field Moiré fringe patterns under 0% RH and 5°C.....	51
3-13 V-field Moiré fringe patterns under 0% RH and 5°C.....	52
3-14 Measured shrinkage from center to outer surface.....	55

3-15	U-field Moiré fringe patterns under 100% RH and 23°C	56
3-16	V-Field Moiré fringe patterns under 100% RH and 23°C	57
3-17	U-field displacement and strain maps for day	58
3-18	Relative humidity and temperature effect.....	60
3-19	w/c and size effects on averaged shrinkage of cement pastes	61
3-20	U-field moiré fringe patterns for mortar with s/c=37.5%	62
3-21	Strain information for mortar with s/c=37.5% on day 2.....	63
3-22	Displacement maps for mortar with s/c=37.5% on day 2.....	63
3-23	Moiré fringe patterns for mortar with s/c=75% on day 7	64
3-24	Full-field normal strain maps with both (a) large and (b) small gauge lengths for the mortar specimen of s/c=75% on Day 7.....	65
3-25	Aggregate quantity and RH effects on average shrinkage of mortar specimens	66
3-26	Side and top views of gravel test	67
3-27	Day 5 moiré fringe patterns for the gravel test	68
3-28	The Strain analysis for gravel test.....	69
3-29	U-field moiré fringe patterns for w/c =0.4 in room temperature	71
3-30	V-field moiré fringe patterns for w/c =0.4 in room temperature	71
3-31	Day 7 U-field displacement for the sealed specimen with w/c=0.4 in x-y coordinate	72
3-32	W/C ratio and temperature effects on sealed specimen shrinkage	73
3-33	Day 6 displacement and strain analysis for the sealed cement paste specimen with w/c=0.4 in polar coordinate	74
3-34	A modified sealing method.....	75
3-35	Day 7 Moiré fringe pattern for w/c=0.3 and s/c =37.5%	76
3-36	Autogenous shrinkage for mortar with w/c=0.3 and s/c=37.5% in room temperature.....	76
3-37	Scheme of Ring Test.....	77
3-38	Ring Test investigation for RH=0% and room temperature	78

3-39	Pictures of the specimen with a crack in the ring test.....	78
3-40	Moiré fringe patterns before and after one-day immersion	79
3-41	Full-field displacement maps for the swelling test	79
4-1	Scheme of numerical modeling	83
4-2	Boundary conditions of moisture diffusion model	85
4-3	Optimization results	87
4-4	3-D model of shrinkage behavior	88
4-5	FEA results for RH=50% and room temperature	88
4-6	Experimental and FEA results for RH=80% and room temperature	89
4-7	Experimental and FEA results for RH=80% and room temperature on Day 3	90
4-8	Cross-section view of deformations for RH=80% and room temperature on Day 3.....	91
4-9	U&V-field moiré fringe patterns for ring test under RH60% and room temperature	92
4-10	Experimental (above) and FEA (below) results of ring test on Day 2.....	93
4-11	Experimental and FEA shrinkage distribution for Day 2	93
4-12	Experimental (above) and FEA (below) results of ring test on Day 3.....	94
4-13	U and V-field moiré fringe patterns for the square specimen.....	95
4-14	Distribution of normal strain in x-direction along the red line	95
4-15	Experimental (above) and FEA (below) maps for square specimen on Day 4.....	96
4-16	Experimental (above) and FEA (below) results for Day 1 measurement.....	97
4-17	FEA result for out-of-plane displacement.....	98
4-18	Size and arrangement of the steel rods in cement paste.....	99
4-19	Master grating with the sheet on the back	99
4-20	Moiré fringe patterns for reinforced concrete	100
4-21	Experimental (left) and FEA (right) results for reinforced concrete on Day 2.....	101
4-22	Experimental (above) and FEA (below) results for reinforced concrete on Day 3	102

4-23	FEA result for stress development.....	103
4-24	FEA results for full-field stress maps	104
4-25	FEA results for stress maps over the cross section	104
4-26	FEA results for stress development in the ring test of RH=60%	105
4-27	FEA results for full-field stress maps in ring test	106
4-28	FEA results for stress development in the ring test of RH=0%	106
A-1	U-field Moiré fringe patterns for w/c=0.6 in sealed condition	112
A-2	V-field Moiré fringe patterns for w/c=0.6 in sealed condition	112
A-3	U-field Moiré fringe patterns under 80% RH and 23°C	113
A-4	V-field Moiré fringe patterns under 80% RH and 23°C	113
A-5	Additional full-field maps for ring test on Day 2	114
A-6	Additional full-field maps for ring test on Day 3	115
A-7	The full-field strain maps of cement paste only in ring test on Day 2.....	116
A-8	The full-field strain maps of cement paste only in ring test on Day 3.....	116
A-9	Additional full-field strain maps for reinforced concrete on Day 2.....	117

Abstract of Dissertation Presented to the Graduate School
of the University of Florida in Partial Fulfillment of the
Requirements for the Degree of Doctor of Philosophy

CHARACTERIZATION OF SHRINKAGE BEHAVIOR IN CONCRETE MATERIALS

By

Tzu-Chau Chen

December 2009

Chair: Peter G. Ifju
Major: Mechanical Engineering

A novel experimental technique was developed to investigate the shrinkage behavior in cementitious materials. The Cure Reference Method (CRM), previously developed for residual strain measurements in composites, was used to determine the shrinkage that develops in concrete materials during the curing or drying process. This technique involves the replication of diffraction grating on the concrete specimen during the curing process and the use of high sensitivity moiré interferometry. A specially-designed stage was created to help obtain a set of the consecutive phase shifted fringe patterns. Instead of the intensity-based methods, an automated fringe analysis program was used to analyze fringe patterns to obtain full-field displacement and strain information. Shrinkage as a function of time, location, humidity, temperature, water/cement (w/c) ratio and size was measured for unsealed cement paste specimens. Also, a method of combining CRM and removing drying effect was used to explore the relative contribution of non-drying shrinkage (autogenous shrinkage) to the total shrinkage in cement pastes. Furthermore, CRM technique was applied to explore the effect of fine aggregates (sand) on the shrinkage behavior. The effect of sand quantities was investigated to observe how shrinkage responded to this influential factor. The method of removing drying effect was modified to explore the relative contribution of autogenous shrinkage to the total shrinkage in the

specimen with the fine aggregates (mortar specimen). The effect of coarse aggregates (gravel) on shrinkage was also displayed.

An inverse method based on finite element moisture diffusion model and optimization was developed in order to obtain the material properties of cement paste from the complex geometry used in the tests. Once the material parameters were determined, they can be the inputs in finite element analysis for the predictions. The tests in different drying conditions, with different geometry of the specimens, and for the reinforced specimens were performed and their results were compared with FEA to validate the constructed model and the obtained materials properties.

Ring tests were performed under both normal and extreme low humidity conditions for crack investigation. Also, the FEA of the ring test under normal humidity has shown that the numerical result had good agreement with that from the experiment.

Finally, stresses were predicted in FEA model for both free shrinkage and restrained (ring test) shrinkage cases.

CHAPTER 1 INTRODUCTION

1.1 Background

Concrete is a material that forms the basis of our modern society. Nearly every aspect of our daily life depends directly or indirectly on concrete materials. For example, we live, play, work, or study directly in concrete structures or buildings to which we drive directly over concrete roads and bridges. Indirectly, our goods can be transported by trucks running on concrete freeways or by trains traveling on rails supported by concrete cross-ties; water for our drinking and raising crops is stored behind the concrete dams and is distributed through the systems of concrete water ways, conduits and pipes. We take concrete for granted when we are enjoying all the activities in our daily life. However, it can be truly said that many achievements of our modern civilization have been attributed to concrete.

Since concrete is closely related to our life, every aspect of its behavior/properties must be understood in order to thoroughly utilize it to the highest potential. One aspect that requires proper characterization is the shrinkage behavior because it influences the development of tensile stress when external or internal restraints exist and causes the subsequent cracking in concrete. The case of external restraints is very straightforward and can be explained by Figure 1-1 [1]. On the other hand, the internal restraint is due to non-uniform shrinkage over the cross section. It is known that larger shrinkage occurs near the outer surface and smaller shrinkage in the inner core. In this case, tensile stress develops close to the outer surface and compressive stress in the inner core [2]. Both cases can lead to subsequent cracking and reduction of its service life when the tensile stress that develops in concrete is greater than the tensile strength. Furthermore, in the case of reinforced concrete, the cracking may produce a direct path for chloride ions to reach the reinforcing steel. Once chloride ions reach the steel surface, the steel will corrode, which itself

can cause cracking, spalling, and delamination of the concrete [3]. As a result, the shrinkage behavior must be well understood in order to better evaluate the structural life of concrete or to properly control the occurrence of the shrinkage-induced cracks.

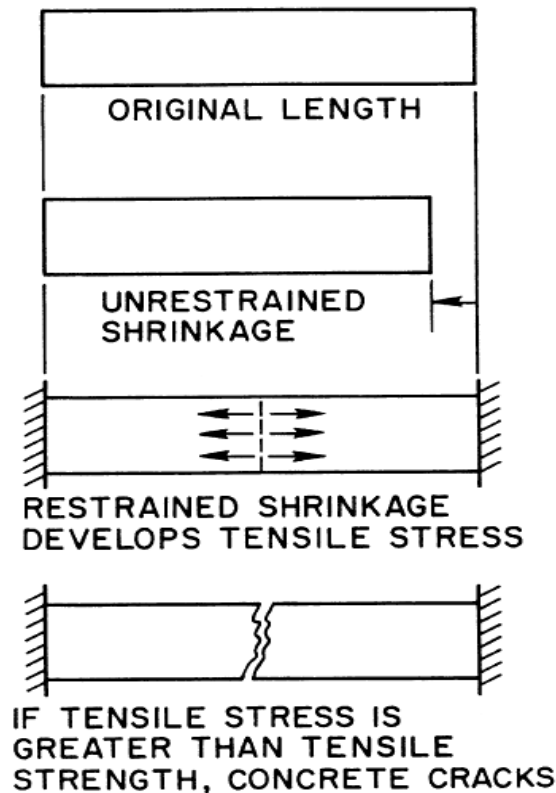


Figure 1-1. Concrete under external restraints

1.2 Literature Review

Concrete materials experience volume change during their service life. The total in-service volume change is the resultant of shrinkage and deformation from applied load or temperature variation. Shrinkage is typically defined as the strain measured on a load-free & unrestrained concrete specimen, not including changes due to temperature variations and is commonly described in micro-strains. According to the definition of concrete materials, there are three main categories: cement paste, mortar and concrete [4] and their compositions are indicated in Table 1-1. But generally speaking, they are all called “concrete” in our daily living.

Table 1-1. Categories of concrete materials

Category	Components
Cement paste	= Cement + water
Mortar	= Fine Aggregate (sand) + Cement Paste
Concrete	= Fine and Coarse Aggregate (gravel) + Cement Paste

1.2.1 Shrinkage Behavior in Concrete Materials

There are four main types of shrinkage associated with concrete materials: plastic, carbonation, autogenous, and drying shrinkage. Plastic shrinkage is due to moisture loss from the concrete before the concrete sets [5-7]. Carbonation shrinkage is caused by the chemical reaction of various cement hydration products with carbon dioxide present in the air [8-10]. This type of shrinkage is usually limited to the surface of the concrete. Autogenous shrinkage is associated with the hydration of the cement, which is a chemical reaction between water and cement, without water loss into the surrounding environments. This type of shrinkage tends to increase at lower water to cementitious materials ratio (w/c) and at a higher cement content of a concrete mixture. In general, it is relatively small and not distinguished from drying shrinkage for normal-strength concrete materials with w/c ratio larger than 0.4. Drying shrinkage is due to drying or moisture loss of concrete into the surrounding environments. The ratio of autogenous and drying shrinkage in total shrinkage of concrete is schematically illustrated as in Figure 1-2 [11, 12]. The figure indicates that autogenous shrinkage already occurs before the start of drying. The start of drying is usually set as the point at which the measurement of shrinkage is zero. Also, it can be seen that the contribution of autogenous shrinkage to the total shrinkage is significant for high-strength concrete materials. On the contrary, autogenous shrinkage in normal-strength concrete contributes to the total shrinkage insignificantly. The magnitude of the

total shrinkage depends on concrete mixture proportions and material properties, method of curing, ambient temperature and humidity conditions, and geometry of the concrete element. In the analysis of concrete structures, two components, drying and autogenous shrinkage are usually taken into account because they are more associated with induced cracking in concrete materials. As a result, autogeneous and drying shrinkage draw more attention from the concrete researchers. Therefore, it is necessary to discuss them in more details as below.

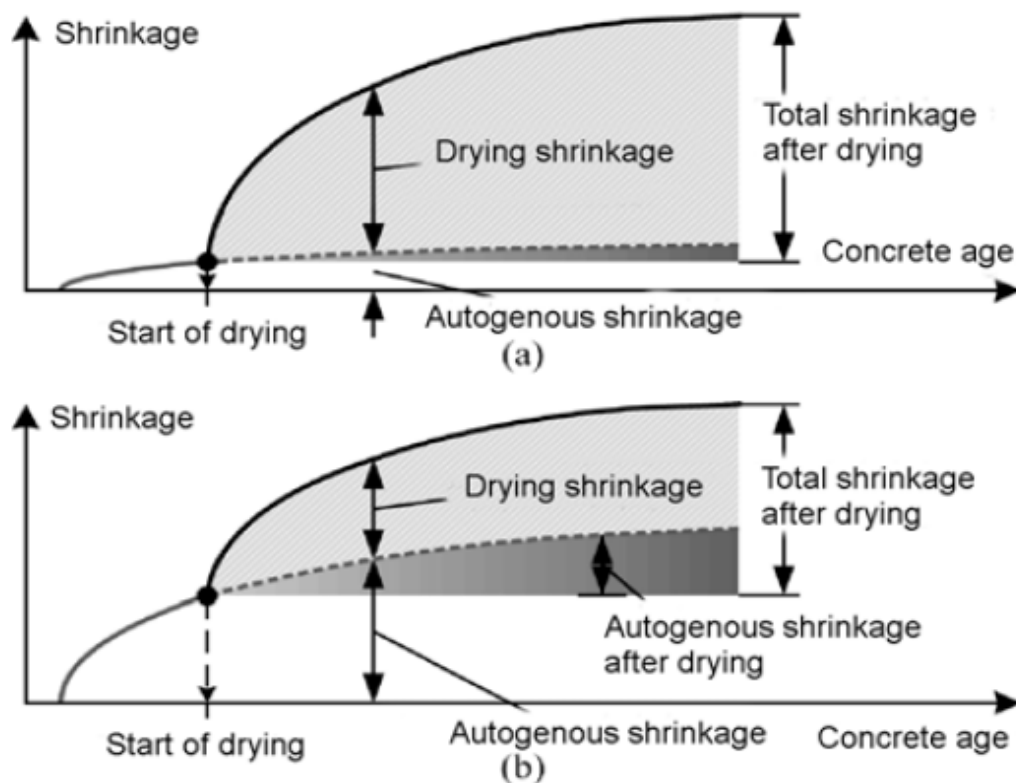


Figure 1-2. Shrinkage strain components in (a) normal-strength and (b) high-strength concrete (Sakata & Shimomura 2004)

1.2.1.1 Autogeneous shrinkage

The shrinkage occurring in the absence of moisture exchange (as in a sealed concrete specimen) due to the hydration reactions taking place inside the cement matrix is termed autogenous shrinkage [13]. Autogenous shrinkage was almost never considered as a factor in the research on shrinkage before 1990. It is usually insignificant for many normal compressive

strength concretes and can usually be neglected. However, for high-strength concrete with w/c ratio less than 0.40, it may be a significant contribution to the total shrinkage. As a result, it has become an issue with the increasing use of high-performance concrete. Factors affecting autogenous shrinkage include water/cement ratio [14, 15], temperature [16], aggregates [17, 18] and admixtures [19, 20] etc. And autogeneous shrinkage is not one-time deformation, but a time-dependent behavior.

1.2.1.2 Drying shrinkage

Shrinkage occurring in a specimen that is exposed to the environment and allowed to dry is called drying shrinkage. For normal-strength concrete with w/c larger than 0.4, it is usually assumed that the entire shrinkage strain is only from drying shrinkage, and any contribution from autogenous shrinkage is neglected. Factors influencing drying shrinkage can be divided into three categories. The first category is drying conditions. Much research has been devoted to the temperature, humidity and wind speed effects [21-28]. Also, because drying shrinkage involves moisture diffusion through the material and moisture loss into the surrounding environment, it depends on the geometry of the specimen, which is the second category, such as the shape and size of the specimen [29, 30]. The third category is the compositions of concrete, including the type of cement, water/cement ratio, and fine/coarse aggregate quantity etc. [31]. Drying shrinkage is also time-dependent behavior as is autogenous shrinkage.

1.2.2 Experimental Techniques

Some experimental techniques have been developed and used to determine the shrinkage that occurs in concrete materials during the curing and drying. There are two major categories of these experimental techniques, non full-field measurements and full-field measurements. They are summarized as the following.

1.2.2.1 Non full-field measurements

The most common one is ASTM C157 standard test method. This method measures the length change of hardened hydraulic-cement mortar and concrete specimen using a comparator [32, 33]. However, this method is categorized into the measurement of the averaged shrinkage of concrete samples. Embedded sensors, such as embedded strain gauges and fiber optics, are also the well-known methods which are used for measuring internal shrinkage at specific locations [34-38]. But these methods are in the category of point measurements and the gathered information is easily altered by the intrusive nature of these tests. Membrane method protocol is for the measurement of autogenous shrinkage and performed by monitoring the weight of a cement paste sample that is sealed in a membrane, submerged in paraffin oil, and suspended from a high-precision balance [39]. This method is able to obtain the averaged shrinkage in terms of volumetric strain rather than linear strain. Although the shrinkage of concrete in a fluid state can be measured, it is not significant to the development of tensile stress. And the lack of a steady contact between the membrane and the cement paste is a considerable disadvantage. Rigid form method measures the shrinkage using a non-contact laser to investigate the length change of a specimen in a conventional rigid steel form [40]. Likewise, this method belongs to the measurement of averaged shrinkage. Other methods, such as corrugated tube method and buoyancy method [41], are all averaged shrinkage measurements. Also, they have their own drawbacks and limitations of use.

1.2.2.2 Full-field measurements

Some of the full-field experimental techniques have been applied in the study of concrete structure inspection. Optical techniques, such as Grid method, Electronic Speckle Pattern Interferometry (EPSI) and Digital Correlation Method (DCM) are the most popular ones for the detection of flaws and cracks in the concrete structures [42-46]. Moreover, moiré interferometry

was used to investigate Fracture of concrete [47, 48]. However, the full-field techniques for measuring shrinkage of concrete are scarce in the literature. An optical technique, digital photogrammetric method, has been used to measure the shrinkage in concrete samples [49]. Although this method offers full-field measurement, it does not possess high sensitivity of displacements and strains measurements. Recently, an image-intensity-matching technique was used to measure strain in cement pastes within an environmental scanning electron microscope [50]. This method is still in the stage of the development.

1.2.3 Numerical Simulation

Since the use of full-field techniques to measure shrinkage is scarce in the literature, the modeling of shrinkage on a full-field basis is not available. Many mathematical models based on ASTM C157 standard test were proposed to predict averaged shrinkage of concrete specimens. On the other hand, due to the fact that shrinkage closely relies on moisture distribution, much research has been devoted to the measurement and the modeling of moisture distribution in concrete materials in terms of moisture content or internal relative humidity. However, they serve as the qualitative indication of shrinkage rather than quantitative.

1.2.3.1 Moisture diffusion modeling

Moisture diffusion models based on Fick's Law were widely used and solved analytically or numerically to investigate moisture distribution in concrete specimens [51-62]. The majority of commercial software packages do not offer mass diffusion modules but only heat conduction modules. The governing equation of heat conduction given by Fourier's law has the generalized form similar to the equation of diffusion given by Fick's Law. Hence, the heat conduction analogy is extremely useful in practice. However, for high-strength concrete with lower w/c ratio, moisture distribution cannot be governed only by moisture diffusion. As a result, the

decrease in relative humidity or moisture content due to self-desiccation needs to be considered in the moisture distribution modeling [63-66].

1.2.3.2 Shrinkage modeling

There exist many mathematical models associated with predicting shrinkage of concrete materials. A review of the literature for these types of prediction models shows that the most widely discussed and used models are Comite Euro-International Du Beton (CEB Model Code 1990), Bazant and Panula (BP-KX and Model B3), and American Concrete Institute (ACI 209) etc. [67-75]. However, all these models were based on the results of ASTM C157 standard test. The models are used for the prediction of averaged shrinkage as a function of time, and composition of concrete materials. The shrinkage at certain locations of interests cannot be known from these models.

1.2.3.3 Inverse method

The inverse methods based on optimization have been widely used to evaluate unknown coefficients such as material parameters or to determine the load and boundary conditions in the structural or heat transfer problems. They are computed by minimizing the error between the measured values obtained experimentally and those found by finite element analysis or analytical solutions.

Several methods have been developed for the determination of material properties using experimentally determined displacement or strain data. The analytical model for a circular disc in diametric compression with a linear least square updating procedure was used to determine the elastic constants using moiré interferometry displacements [76]. The inverse approach was applied to determine the far-field or residual stresses in open-hole specimens with biaxial loading [77]. A non-linear least squares solution was described for the evaluation of far-field stresses, material elastic properties and residual stresses in an infinite orthotropic plate with a hole.

Computer generated moiré interferometry displacement data was used for the updating procedure [78, 79]. The application of the microscopic hole method was demonstrated to assess the elastic properties of polycrystalline silicon freestanding thin films employed in micro-electro-mechanical system (MEMS) devices. The analytical model for an infinite plate with a hole with a Levenberg-Marquardt updating procedure using the nanometric displacement data obtained from atomic force microscopy (AFM) was used [80]. An overview of the existing full-field measurement techniques, their application in the field of composite material characterization and identification of parameters of constitutive equations has been presented [81].

On the other hand, several methods have been developed for calculating the loads from the structural response data that are measured using a variety of experimental techniques. The measured structural response is often the displacements or strains. An optical method of using CCD cameras to measure the displacements in a loaded structure has been described. Images before and after the loading are obtained and using sub-pixel edge detection techniques, the displacements are computed [82]. Loads acting on a beam by modeling the load distribution using Legendre polynomials with unknown weight factors have been computed. The unknown coefficients are computed by minimizing the error between the measured values of displacements obtained experimentally and those found by FEA [83]. A method to identify the element stiffness parameters of a truss and frame-like structures by utilizing elemental strain measurements has been proposed [84]. A videogrammetric technique for determining aerodynamic loads has been developed. Elastic deformations are measured optically and used to obtain the normal force and pitching moment [85]. An inverse problem approach has been presented for computing or calibrating the loads and boundary conditions acting on a structure. This enables the creation of more accurate finite element models, especially for structures that

have complicated load distribution and compliant boundary conditions. The method involves minimizing the least square error between the strains computed using the finite element model and the strains and displacements obtained experimentally by luminescent photoelastic coating (LPC) technique [86].

1.3 Research Objectives

In this research work, there are four main objectives proposed as following:

First, a full-field experimental technique must be developed for the measurement of in-plane deformation on the surface of concrete materials during drying. This technique is based upon the Cure Reference Method (CRM) in conjunction with the use of high sensitivity moiré interferometry. Because moiré interferometry requires a high quality diffraction grating on the specimen, the most challenging part in developing this technique is to create a procedure of replicating the diffraction grating on the concrete specimen during the curing process. Moreover, the selection of diffraction grating material is another issue. The diffraction grating should be able to survive in different drying conditions, and should not degrade or be damaged with time so that shrinkage as time-dependent deformation behavior in concrete materials can be captured. Also, it should be non-reinforcing to the specimen.

Second, based on the experimental results, the shrinkage behavior in concrete materials should be characterized and compared with the trends documented in the literature. Once they have good agreement, the technique is considered reliable and robust.

Third, based on the experimental data, an inverse method must be developed in order to obtain the material properties of shrinkage in cement paste from the complex geometry used in the tests. The method involves minimizing the least square error between the strains computed using the finite element model and the strains obtained experimentally by the moiré interferometry technique. Once the material properties are identified, they can be the inputs in

finite element analysis for the prediction of shrinkage behavior in concrete materials. The tests in different drying conditions or with different geometry of the specimens can be performed and their experimental results can be compared with FEA to validate the constructed model and derived material properties.

Finally, the stress development in concrete specimens can be simulated in FEA and the occurrence of cracking can be predicted if the tensile strength is given.

CHAPTER 2 METHODOLOGY

2.1 High Sensitivity Moiré Interferometry

Moiré interferometry has matured rapidly as a powerful tool, proven by numerous industrial and scientific applications [87-89]. It is an optical technique which has been used in the studies of composite materials, polycrystalline materials, piezoelectric materials, fracture mechanics, biomechanics, structural elements & joints, residual stress measurements, strain gauge calibration and more recently, thermal deformation of electronic packages. It utilizes moiré phenomenon of optical interference to measure the in-plane deformation of objects. The principle of high sensitivity moiré interferometry is founded on the interference between the specimen grating and the virtual reference grating created by two laser beams.

Moiré interferometry records the data as interference fringe patterns, or contour maps of displacement fields. It is characterized by a list of excellent qualities as follows:

- (a) full-field technique, i.e. quantitative measurements can be made throughout the field;
- (b) high sensitivity to in-plane displacements U and V , typically 0.417 μ m per fringe;
- (c) insensitive to out-of-plane displacements W ;
- (d) high spatial resolution, meaning that measurements can be made in tiny zones;
- (e) high signal-to-noise ratio, ensuring that the fringe patterns have high contrast and excellent visibility;
- (f) determination of shear strains as readily as normal strains;
- (g) real-time technique, where the displacement fields can be viewed as loads are applied.
- (h) capability for finite element analysis (FEA) validation, obtaining or correcting material properties or boundary conditions required for FEA inputs.

The general scheme of moiré interferometry is illustrated in Figure 2-1. A high-frequency cross-line grating on the specimen called the specimen grating, initially of frequency f_s (1200 lines/mm), deforms together with the specimen. Two parallel (collimated) incident laser beams

from the U-field mirrors strike the specimen and are diffracted back. Since the specimen grating is deformed as a result of the applied loads or thermal deformation, these diffracted beams are no longer collimated. Instead, they are beams with warped wavefronts, where the warpage is related to the deformation of the grating. These two coherent beams interfere in the image plane of the camera lens, producing a U-field interference fringe pattern which gives displacement information in x-direction. Similarly, a V-field interference fringe pattern produced by the beams from the V-field mirrors gives displacement information in y-direction.

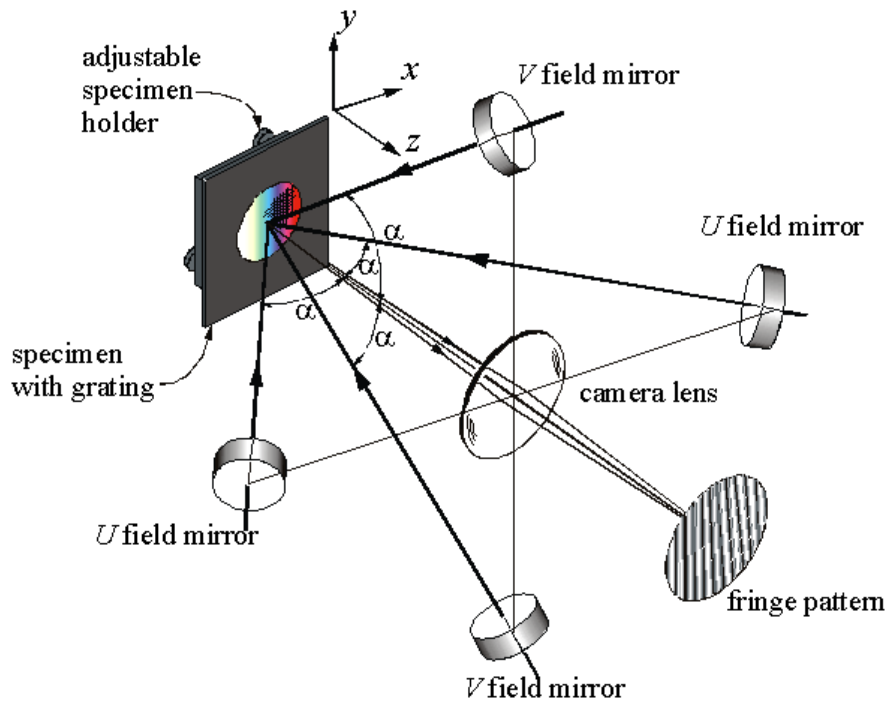


Figure 2-1. Scheme of moiré interferometer

Another more understandable physical explanation considers a virtual reference grating, of frequency f , created by two incident beams as in Figure 2-2. The frequency f of the virtual reference grating is determined by the angle α and wavelength λ (632.8 nm).

$$f = \frac{2}{\lambda} \sin \alpha \quad (2-1)$$

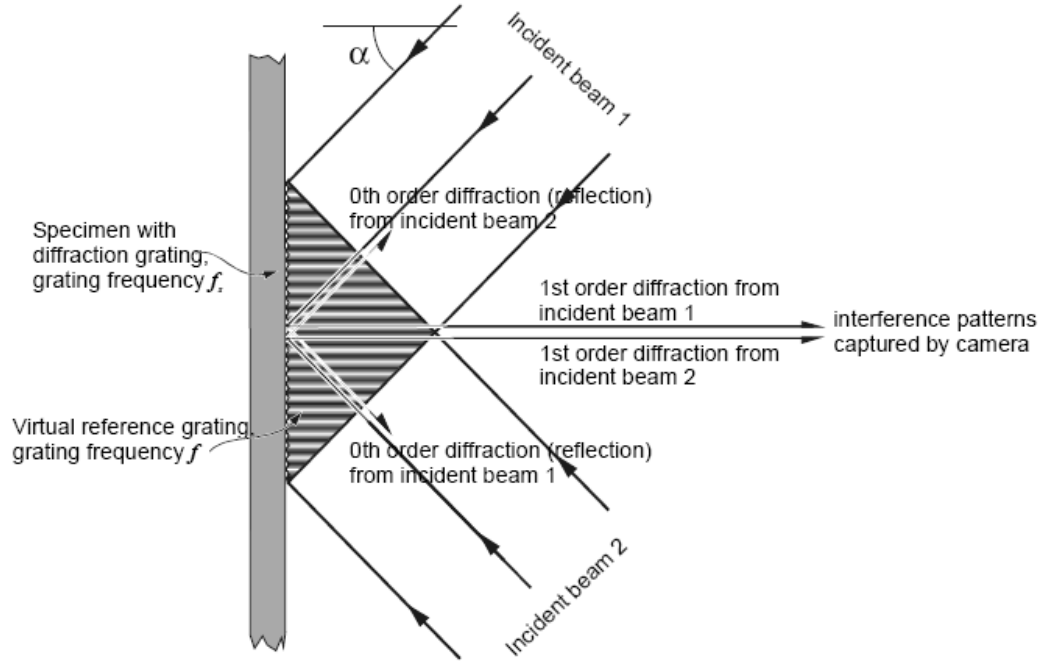


Figure 2-2. Schematic diagram of moiré interferometry

Moiré interferometry utilizes a virtual reference grating of twice the initial frequency of the undeformed specimen grating by adjusting α equal to 47.5° .

$$f = 2f_s \quad (2-2)$$

In this case, when the specimen grating is undeformed, there will be no interference fringes called null-field. However, when the specimen is deformed in the x-y plane, the virtual reference grating and the deformed specimen grating interact to form the moiré fringe patterns. The in-plane displacement maps can be determined according to the equations

$$U(x, y) = \frac{1}{f} N_x$$

$$V(x, y) = \frac{1}{f} N_y \quad (2-3)$$

Also, the in-plane normal strains and the in-plane shear strain can be calculated with the selected gauge length by the equations

$$\begin{aligned}\varepsilon_x &= \frac{1}{f} \frac{\Delta N_x}{\Delta x} \\ \varepsilon_y &= \frac{1}{f} \frac{\Delta N_y}{\Delta y} \\ \gamma_{xy} &= \frac{1}{f} \left(\frac{\Delta N_x}{\Delta y} + \frac{\Delta N_y}{\Delta x} \right)\end{aligned}\tag{2-4}$$

where $U(x, y)$ and $V(x, y)$ are the displacements in x and y direction at the point of interest (x, y) with respect to the chosen origin. N_x and N_y are the fringe orders in x and y direction from the origin to the point of interest. ε_x and ε_y are the normal strains, and γ_{xy} is the shear strain. Δx and Δy are the selected gage lengths; ΔN_x and ΔN_y are the fringe order difference over the selected gage length respectively.

2.2 Cure Reference Method

The Cure Reference Method (CRM) was originally developed for the measurements of residual strains which develop in composites as cooling via moiré interferometry [90-94]. Also, it was already applied for the measurement of post-gel chemical shrinkage in epoxy [95]. Unlike many other methods, the CRM technique is non-destructive, gathers the information not altered by the intrusion of the tests, and measures the deformation on a full-field basis. Because of these advantages, the same methodology was adopted to investigate shrinkage behavior in concrete materials.

2.2.1 Methodology of CRM

In the application of CRM to the shrinkage measurements in concrete materials, the diffraction grating is replicated from a master grating substrate onto the concrete specimen during the curing process or at the stress-free state. The stress-free state exists before the solidification of the specimen. The deformation of the concrete specimen at fluid state is unable

to be measured in CRM. However, it is of little significance to inducing cracks because fluid cannot carry stress. After the concrete specimen is hardened to some extent, the deformation causes it to carry stress. But at this moment, the in-plane dimensions of the specimen and the frequency of the diffraction grating on its surface remain the same due to the constraint from the rigid substrate. Once the concrete specimen is set and separated from the master grating substrate, the accumulated stresses are released and the specimen as well as the diffraction grating attached to it deforms. Hence, the frequency of the specimen grating is changed as the deformation occurs. The virtual reference grating is first created by tuning the moiré interferometer to reach the null field with the master grating. To minimize errors that can occur due to the misalignment of the gratings between the master grating and the specimen grating, the master grating is rotated 90° counter-clockwise. This operation accounts for any possibility that the cross lines of the master grating are not exactly perpendicular. Then by replacing the master grating with the deformed specimen grating, the interference fringe patterns can be obtained and the in-plane full-field deformation can be measured accordingly.

Another advantage of CRM is that time-dependent deformation in concrete materials can be determined. This requires the grating on the specimen not to degrade with time or in certain drying environments. In routine practice, once the virtual reference grating is created, it is fixed throughout the entire period of the testing. Every day the specimen is properly positioned in the moiré interferometer, the phase-shifted moiré fringe patterns are recorded, and the deformation as a function of time is determined. In summary, CRM is a non-destructive, non-intrusive, full-field, and resilient method.

2.2.2 Replication of Grating

In developing the procedure of grating replication, three major methods were attempted and they are discussed as below.

2.2.2.1 Silicone rubber grating based method without epoxy layer

The first attempted method was using silicon rubber grating (RTV615 A&B 10:1) as the master grating. Then concrete in fluid state was directly poured into the mold which was on top of the silicon rubber grating. Because of good contact between the mold and the master grating, leaking was not a concern. However, there are many issues with respect to this method. First, it was found that there was no grating at all for concrete with lower w/c ratio. The reason for this should be that concrete fluid was too thick to fit into the space of master grating. It was difficult to deal with this problem, but resulted in the putting a weight on concrete fluid. Second, the grating might disappear or degrade later during shrinkage because the grating itself is part of the concrete specimen. Finally, aluminum is a must for increasing the grating efficiency. But aluminum was not well-deposited onto the surface of the specimen in the vacuum deposition process. On the other hand, heat and vacuum resulting from the deposition process might accelerate the drying of the specimen, which should cause significant errors on the experimental results.

2.2.2.2 Aluminized epoxy grating based method

The second method was using an aluminized epoxy grating as the master grating was attempted. Aluminum in double layers was used with a parting agent (Kodak Photo-flo 200 diluted 1:300 in distilled water) in between in order to help separation of the specimen from the master grating. Parting agent was applied uniformly on the surface of the first aluminum layer by using a lens tissue prior to the deposition of the second aluminum layer. This method was forming a thin layer of epoxy on the surface of master grating and then fluid concrete was poured into the mold. After separation, the top or second layer of aluminum with epoxy was intended to be transferred unto the concrete specimen; the bottom layer remained on the master grating. However, the result has shown that concrete fluid etched aluminum if it went through the thin

epoxy layer as shown in Figure 2-3 (a). If not, there was another issue as shown in figure 2-3 (b) indicating that concrete is subject to breaking during separation.

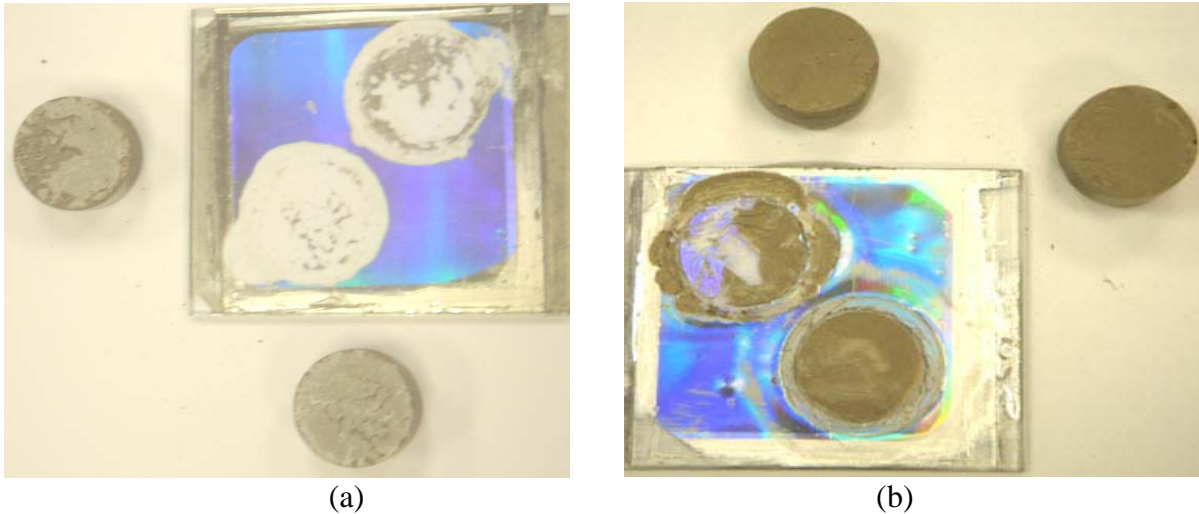


Figure 2-3. (a) Concrete fluid etched aluminum (b) concrete broke during separation

2.2.2.3 Silicone rubber grating based method with epoxy layer

In order to deal with all the issues addressed above, a method of using the silicone rubber RTV 6428 grating as the master grating and forming a thin layer of epoxy on the surface of the master grating has been developed. The procedure to prepare the diffraction grating on the specimen was described here.

Step 1: A 57.1 mm x 57.1 mm silicone rubber RTV 6428 grating (master grating) was prepared by replication from a photoresist or epoxy diffraction grating. The primer for RTV 6428 silicone rubber is SS4155, which provides very good adherence of RTV 6428 to glass substrates. Envirotex Lite epoxy was mixed, degassed by the centrifugal, and added to the master grating. The pool of epoxy needs to cure for 2 hours in advance to increase its viscosity.

Step 2: A clean glass plate was pushed onto the pool of epoxy to make it as thin as possible. Then the glass plate was removed horizontally and slowly from the master grating to prevent beads or bubbles. A thin layer of epoxy of approximately 100 μm in thickness was

formed on the master grating. Because of the relative thickness and compliance after cure, its reinforcement to the specimen was considered negligible.

Step 3: A silicone rubber mold of 28 mm in inner diameter was put on the master grating. Then the mixed concrete fluid was poured into the mold. The mold was made of GE RTV 627 silicone rubber.

Step 4: 24 hours was required before the concrete was set and epoxy was cured. Epoxy needs to be well-cured to become the diffraction grating of good quality.

Step 5: The concrete specimen was demolded and separated from the master grating. Due to lower bonding between the thin epoxy layer and the master grating, the epoxy diffraction grating was transferred onto the concrete specimen. The size of the specimen was 28 mm in diameter and 11 mm in thickness.

The same steps can be applied to replicate the diffraction grating on the specimens in the different shape or size as shown in Figure 2-4. The procedure to prepare the diffraction grating on the specimen is illustrated in Figure 2-5.



Figure 2-4. Concrete samples and molds

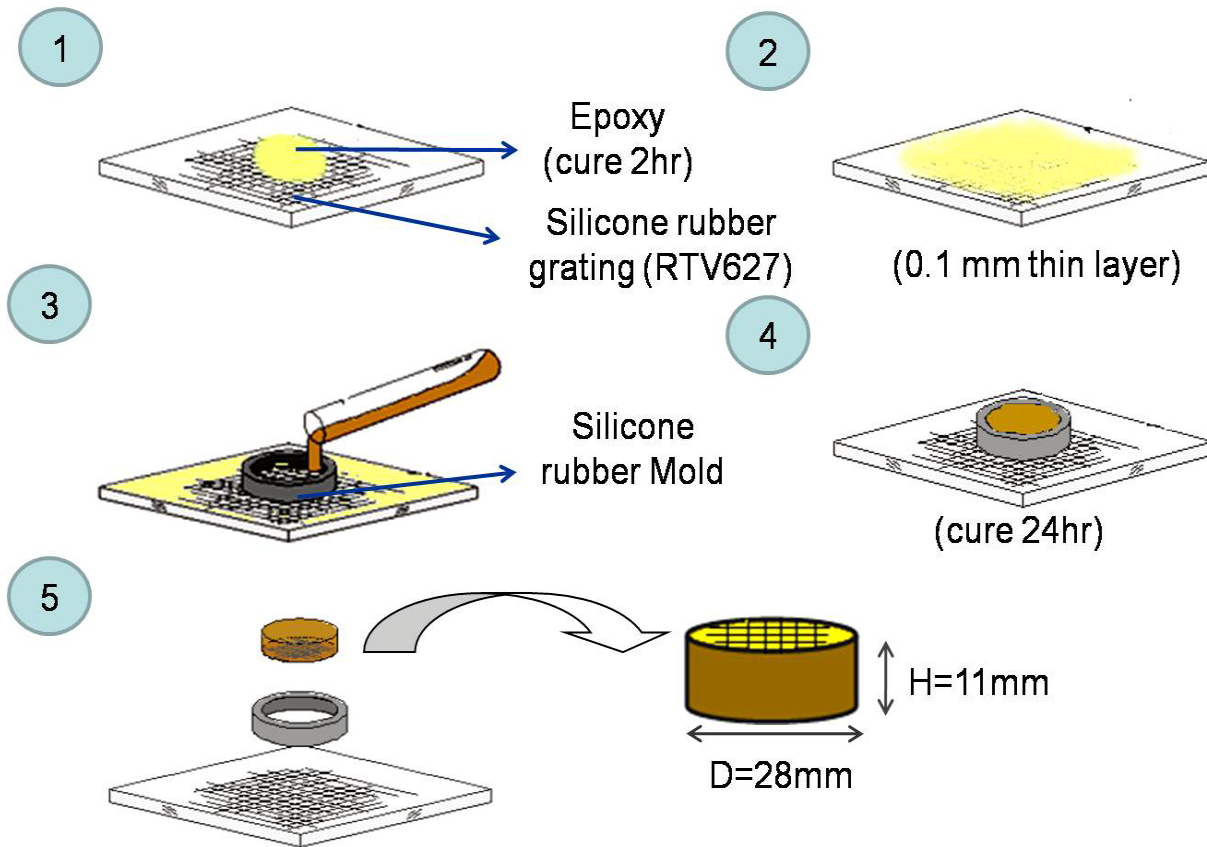


Figure 2-5. Procedure to prepare diffraction grating

Once the master grating was separated from the specimen, it was examined by observing moiré fringe patterns in the moiré interferometer. The U and V-field moiré fringe patterns in the null field and the fringe patterns with rotation carriers are shown as in Figure 2-6. The area in the circle was where the replication took place. The fringe patterns in the circled area remain the same as those in the area outside the circle. This indicated that the deformation of the concrete specimen did not cause any damage or distortion on the master grating. Therefore, the master grating can be used as the reference grating in the measurements.

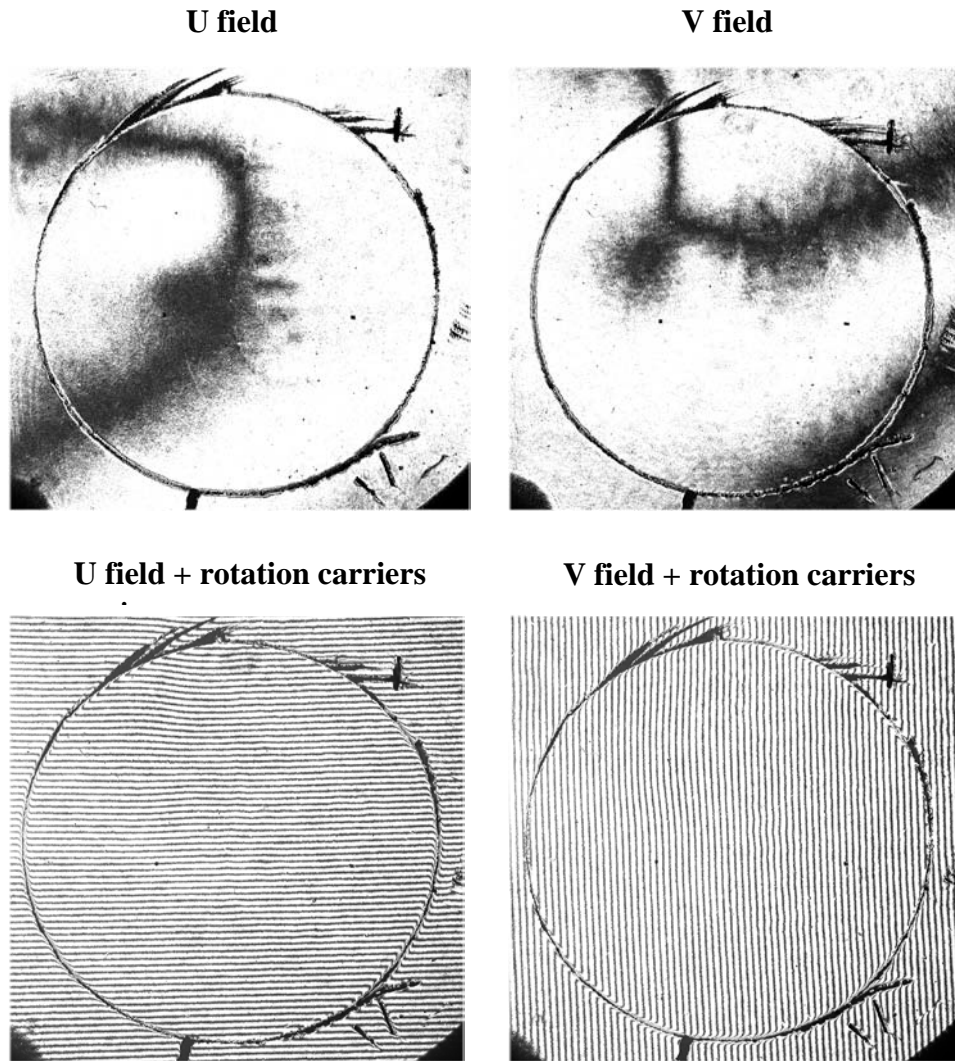


Figure 2-6. Fringe patterns from the master grating

2.3 Automated Fringe Analysis

Traditionally, the fringe patterns are analyzed manually by choosing the positions of interest and counting the fringe numbers within the selected gauge lengths. This is an intensity-based and point-wise method. Although this method can be repeated on multiple data points, it is time-consuming and causes errors because of the uncertainty in determining the exact locations of fringes. Methods based on extraction of the underlying phase distribution are becoming popular since they have significant advantages over the intensity-based methods: data is obtained

over the full field, not just at the fringe maxima and minima, the sign of the deformation is given and immunity from noise is normally better [96]. An automated fringe analysis system based on phase shifting theory was developed to obtain the full-field displacement and strain information.

The automated fringe analysis system was developed by **WeiQi Yin** in the UF ESA Lab to obtain the full-field displacement and strain maps automatically. There are five basic steps of this system listed as below.

Step 1: Fringe pattern recording

A stage specially for phase shifting was designed in the Experimental Stress Analysis (ESA) Lab at the University of Florida [97]. It applies a phase ramp to the U and V direction after calibration. The Insight Firewire charged coupled device (CCD) camera and a PC-based frame grabber were acquired from Diagnostic Instruments Inc. The CCD camera is used to scan the fringe pattern and the frame grabber is used to digitize the image and store it into the computer. The combination of CCD camera, frame grabber and computer can output images with high resolution of 16bits and maximum size of 1000×1000 pixels.

Step 2: Noise filtering

An appropriate noise reduction algorithm is needed since noise exists in all fringe patterns. The noise in the fringe pattern is considered as a random noise with a Gaussian distribution in our research. Gaussian Low Pass Filter (GLPF) in the frequency domain was chosen to remove the noise [98] before phase shifting step and the results showed that it was an effective way to reduce the noise.

Step 3: Phase shifting

Moiré fringe patterns are developed by interference caused by two light sources reflecting off a common location. Within that interference there is a corresponding intensity and phase

associated at each location (pixel) within the fringe image which can be mathematically expressed as Eq. (2-5),

$$I(x, y) = I_b(x, y) + I_m(x, y) \cos[\phi(x, y)] \quad (2-5)$$

where $I(x, y)$ is the recorded intensity of each pixel, $I_b(x, y)$ is the background intensity, $I_m(x, y)$ is the fringe amplitude, and $\phi(x, y)$ is the phase function to be measured.

Based on the expression above, it is generally impossible to obtain a unique phase distribution from a single fringe pattern. Positive phase cannot be distinguished from negative without more information. The solution to this problem is to add to the phase function of known phase ramp which is linear in either time or position as shown in Eq. (2-6).

$$I(x, y) = I_b(x, y) + I_m(x, y) \cos[\phi(x, y) + n\alpha] \quad n = 0, 1, 2, \dots, N-1 \quad (2-6)$$

where $n\alpha$ is the added known phase ramp, N is the total number of phase shifted and n is the order of the phase shifting pattern.

The wrapped phase, $\varphi(x, y)$, can be extracted by N phase shifted fringe patterns using Eq. (2-7),

$$\varphi(x, y) = \operatorname{arctg} \frac{-\sum_{n=0}^{N-1} I_n(x, y) \sin(2n\pi / N)}{\sum_{n=0}^{N-1} I_n(x, y) \cos(2n\pi / N)} \quad (2-7)$$

Step 4: Phase unwrapping guided by quality

A Phase unwrapping algorithm based on the quality map of the wrapped phase was developed to obtain the natural unwrapped phase. Quality maps are arrays of values that define the quality or goodness of each pixel of the wrapped phase. In a quality map, the areas with low quality represent unreliable phase data. There are many quality maps available such as

correlation, pseudo-correlation, phase derivative variance (PDV), etc [99]. In this paper, PDV map was utilized as the quality map.

PDV map is used to lead the phase unwrapping algorithm starting from the pixel with high quality to the pixel with poor quality. After phase unwrapping, the whole field phase information which can be easily converted into displacement and strain information via Eq (2-8).

$$\begin{cases} U(x, y) = \frac{1}{f2\pi} \phi_U(x, y) \\ V(x, y) = \frac{1}{f2\pi} \phi_V(x, y) \end{cases} \Rightarrow \begin{cases} \varepsilon_{xx}(x, y) = \frac{1}{f2\pi} \frac{\Delta\phi_U(x, y)}{\Delta x} \\ \varepsilon_{yy}(x, y) = \frac{1}{f2\pi} \frac{\Delta\phi_V(x, y)}{\Delta y} \\ \varepsilon_{xy}(x, y) = \frac{1}{2f2\pi} \left[\frac{\Delta\phi_U(x, y)}{\Delta y} + \frac{\Delta\phi_V(x, y)}{\Delta x} \right] \end{cases} \quad (2-8)$$

Step 5: Calculation of displacement and strain

The displacement or unwrapped phase field contains optical and electrical noise. The noise may not significantly affect the displacement field; however, it can result in large errors when calculating strain. Generally, the deformation of the specimen measured via moiré Interferometry is continuous, which indicates that the unwrapped phase, displacement, strain and should also be continuously distributed. However, the noise from an optical or electric device might break the continuity and incorporate significant error in strain calculation. The traditional method to calculate the strain is highly sensitive to the existence of noise in the phase map. At the same time, the selection of the gage length will also greatly affect the result. The idea of using global surface fit technique to smooth the unwrapped phase map can effectively attenuate the noise. And most importantly, it can calculate gradient (strain) analytically. Thin plate spline (TPS) is chosen because it is insensitive to noise in the data and it has high capability of constructing complex surface shapes. Theoretically, all the pixels recorded by the CCD camera can be used in TPS surface fit to maintain the spatial and strain resolution. However, the estimation of

parameters of TPS [100-103] is time-consuming or even fails for large images. One solution to this problem is to use the subset of the data, which can reduce spatial resolution somehow. A trade-off between the resolution and computational efficiency has to be made to obtain reasonable results for large images. TPS technique was used to analyze the numerically-simulated fringe pattern or the experimental fringe patterns. The results show the effective performance and accuracy of this method.

CHAPTER 3 SHRINKAGE MEASUREMENTS OF CONCRETE

3.1 Introduction

Using the Cure Reference Method which was described in the previous chapter, some tests were performed and their results were characterized and compared with the trends of shrinkage behavior recorded in the literature. Because a large number of factors can influence the shrinkage in concrete materials, in every test only one factor was set as a variable and the others were fixed in order to investigate the specific effect. Among these factors, temperature and relative humidity are the most important ones to be properly controlled because they are not quite stable in the surrounding environments. Without accurate control of them in the tests, the experimental results can be greatly affected. As a result, an environmental chamber for controlling the temperature and humidity was created.

In the concrete shrinkage measurements, once the specimen had been demolded, the master grating was positioned in the moiré interferometer as the reference grating for the tuning of the moiré interferometer to a null field which is regarded as the absolute reference of non-deformation. Then by replacing the master grating with the specimen grating, a set of the initial (day 1) fringe patterns can be captured by the CCD camera. After that, the specimen was stored in the environmental chamber which establishes the specific drying condition for the duration of six days. Every 24 hours in this period, the specimen was removed from the chamber and positioned in the moiré interferometer, a set of the consecutive phase-shifted moiré fringe patterns was recorded and the specimen was stored back after the measurement. Precautions to accurately position the specimen were taken so that the location and orientation were repeatable. These procedures are discussed in detail in ref [91]. An automated strain analysis system based on phase shifting theory was used to obtain the full-field displacement and strain maps for the

measurements from day 1 to day 7. Shrinkage as a function of time, location and other factors was determined accordingly.

3.2 Chamber Setup

A 100% air-tight food storage container served as the chamber (Figure 3-1). The picture shows that the desiccant fills the bottom side of the container to provide low-humidity drying environment to the specimen. The size of the container is around 10x10x15cm. The hygrometer with an accuracy of $\pm 2\%$ RH and $\pm 1^\circ\text{C}$ was used to check the temperature and humidity inside of the chamber.



Figure 3-1. Chamber setup

3.2.1 Humidity Control

Water, saturated salt solutions [104] or desiccates were inserted into the chamber to create differing levels of relative humidity inside the chamber. 0.5 pounds of Drierite desiccants are inserted to create 0~2% relative humidity (RH) inside of the chamber. On the other hand, 100% RH is easily maintained only by replacing desiccates with a cup of 80c.c water. 200c.c. potassium carbonate saturated salt solution is mixed and filled the bottom of the chamber for creating $50\pm 2\%$ RH. Table 3-1 shows the substances for the control of RH inside of the chamber.

Table 3-1. Substances for RH control

Substance	Desiccate	Potassium carbonate	Magnesium nitrate	Sodium chloride	Water
RH (%)	0~2	50±2	60±2	80±2	100

3.2.2 Temperature Control

23°C was room temperature which was very stable in the laboratory. The oven was used to create higher temperature such as 40 °C and 45°C. The refrigerator was used to provide 5°C. The chamber was placed in the oven or the refrigerator if the specific temperature other than room temperature as needed.

3.3 Experimental Setups

In this research, two experimental setups are introduced here. They are the first and second generations of Portable Engineering Moiré Interferometers (PEMI) respectively.

3.3.1 PEMI I

The experimental setup with PEMI I is shown in Figure 3-2. It includes a moiré interferometer, a stage for phase-shifting, a power supply, a specimen fixture, an x-y-z stage, a CCD camera and a desktop. The moiré interferometer is put on the stage which is controlled by the power supply. When the stage is moving, the fringe patterns are shifted and recorded via the CCD camera which is controlled by the software in the desktop. A set of the consecutive phase-shifted fringe patterns is able to be recorded with some interval time. The Figure 3-3 shows a close-up view of this specially-designed stage for fringe shifting. This was designed in the Experimental Stress Analysis (ESA) lab at the University of Florida. The stage is composed of two aluminum plates and four aluminum tubes. The four tubes were precisely machined and attached to the bottom and top plates at 45°. Magnetic wires of 0.007” in diameter with special enamel coating for high temperature were wrapped exactly 200 times around the center of each

of the four aluminum tubes then connected together with strain gage wire to complete the circuit. A 0~35 V, 0~5 A adjustable power supply, from Pyramid, model PS-32 lab was connected to the circuit. By turning on the power and increasing the voltage, the current passed through the magnetic wire circuit. The aluminum tubes are hence heated and have elongation in the 45-degree direction. This then moves the entire moiré interferometer in the 45-degree direction. Therefore, the displacements of the moiré interferometer in both horizontal and vertical directions remain the same. This provides the same phase to both U and V-field fringe patterns.

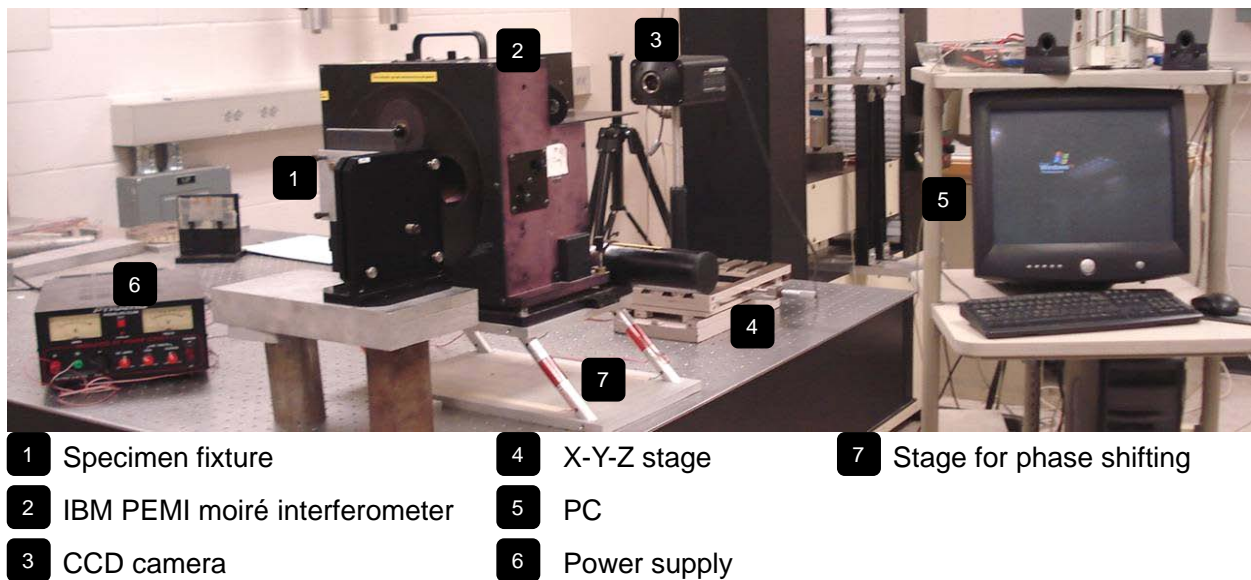


Figure 3-2. Experimental setup with PEMI

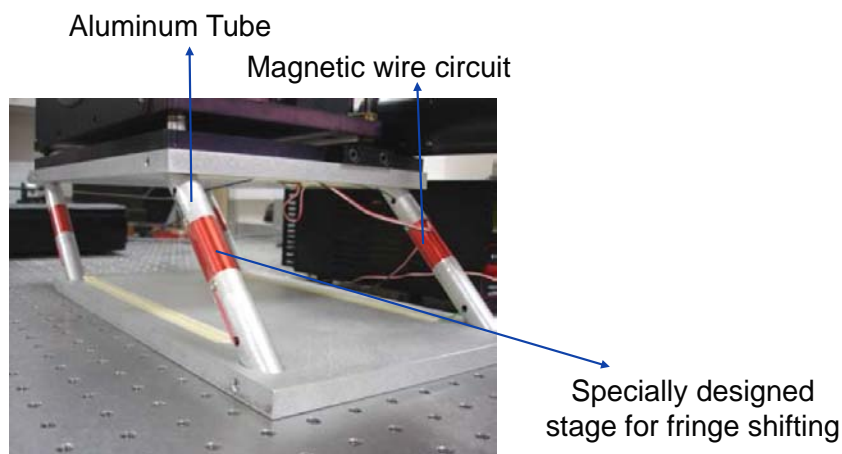
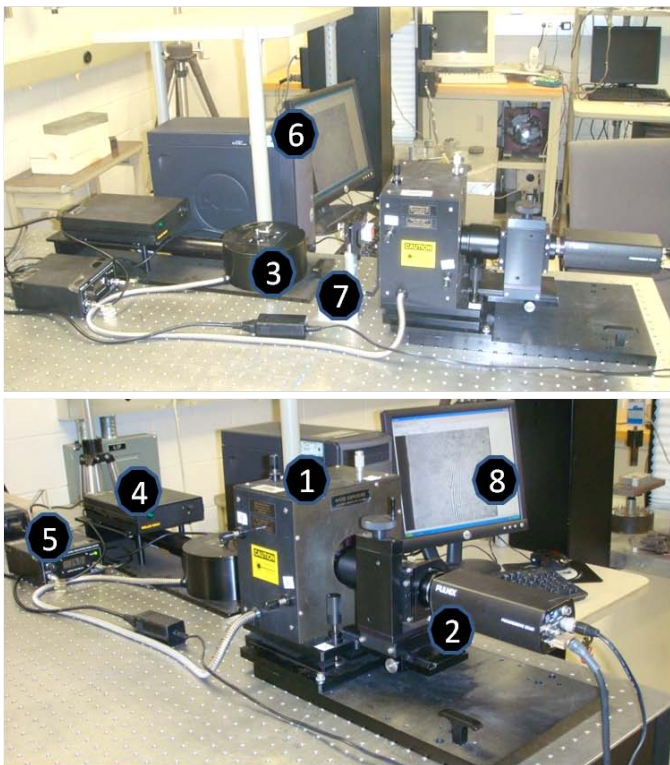


Figure 3-3. Fringe-shifting stage

3.3.2 PEMI II

The experimental setup with PEMI II is shown in Figure 3-4. This setup is much more compact, versatile, portable, and friendly to users because of the combination of all components as one system and extremely easy alignment. Also, there is no need for traditional dark room. The PEMI II has built-in phase shifting hardware that utilizes a custom-designed piezo-electric transducer. The compact design of the phase shifting device offers optimum stability and repeatability. Switching between U and V fields is achieved without touching the interferometer, eliminating the possibility of a disturbance that can modify the fringe patterns. The phase shifting hardware and the high resolution CCD camera are controlled through the software in the computer. A set of the consecutive phase shifted fringe patterns are obtained in the format of 1000x1000 pixels and can be analyzed immediately through the automatic fringe analysis system in the computer.



1. Moire interferometer
2. High resolution CCD camera
3. U&V-field mechanical shutter
4. Power
5. Phase shifting hardware
6. Desktop
7. Fixture and specimen
8. Fringe pattern

Figure 3-4. Experimental setup with PEMI II

3.4 Experimental Results

Since there are numerous factors influencing the shrinkage of concrete materials, the testing can be performed by controlling some other factors in order to investigate the specific effect. Some examples of the moiré fringe patterns are shown and analyzed. And then their results are compared with one another and interpreted.

3.4.1 Drying Condition Effect (Temperature and Humidity)

The cement paste specimens were made by mixing ASTM C150 type I Portland cement with water in w/c ratio of 0.5. Shrinkage in different drying environments was measured. Initial fringe patterns (day 1) which were obtained right after the specimen was demolded revealed some swelling effect, but this was not significant and was able to be explained by FEA in the next chapter. Some examples of the U and V-field moiré fringe patterns in different drying conditions are shown and analyzed.

Case1: 50% RH and room temperature (23°C)

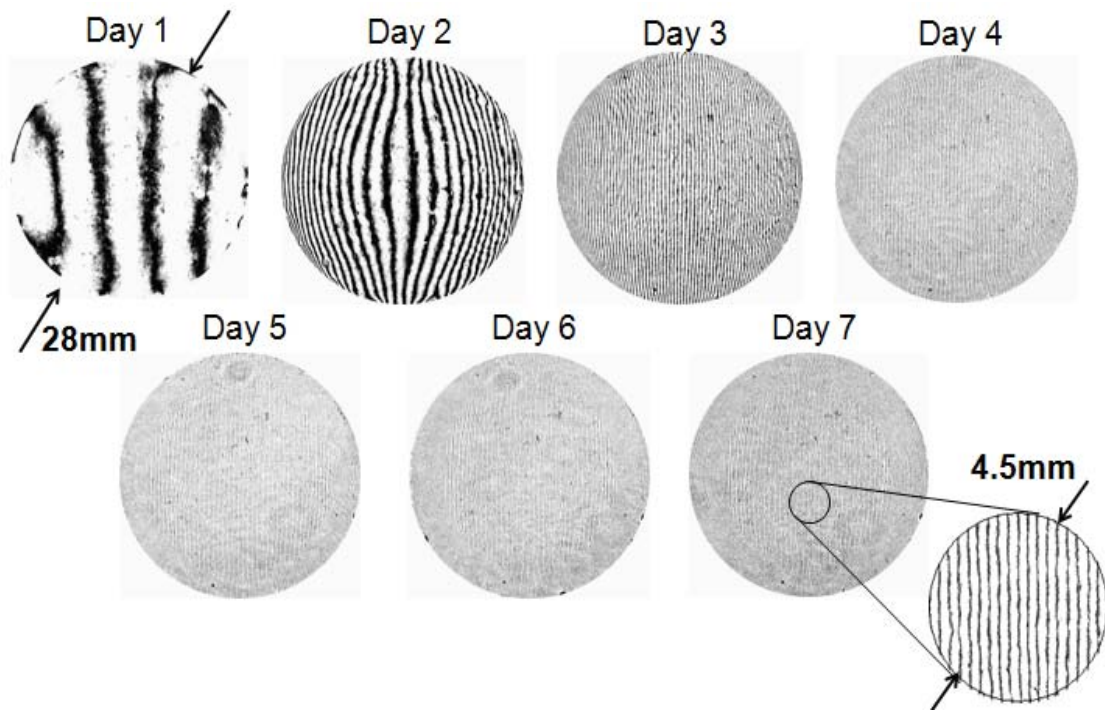


Figure 3-5. U-field Moiré fringe patterns under 50% RH and 23°C

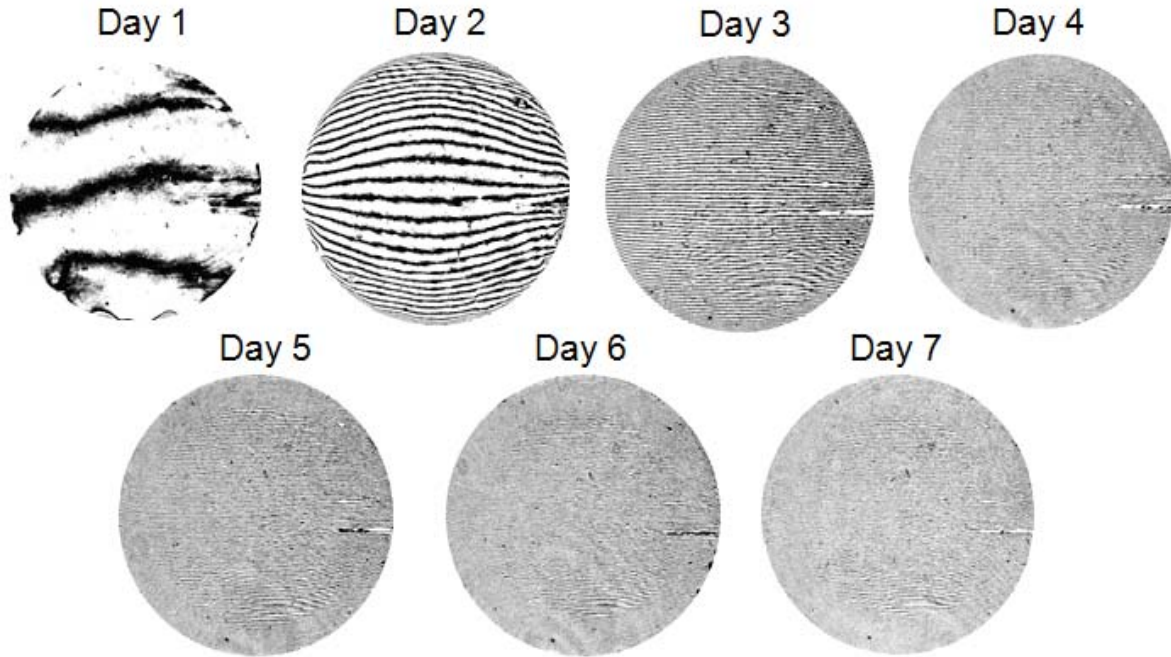


Figure 3-6. V-field Moiré fringe patterns under 50% RH and 23°C

Obviously, Figure 3-5 and 3-6 have shown that the V-field fringe patterns are similar to the U field except the rotation of 90 degree. This is due to the axisymmetric conditions of the specimen. Moreover, the number of fringes increases with time and the fringe density is larger in the area close to the outer surface than in the inner core. Although the fringe density is too high to show here, the inset shows the quality and contrast are high. The full-field maps for each day were obtained via the automated fringe analysis system. Only the day 2 full-field information is shown as Figure 3-7 in x-y coordinate and Figure 3-8 in polar coordinate. In the automated fringe analysis system, the center of the specimen is set as the point of zero displacement. The displacement and strain fields in polar coordinates are obtained by the transformation of those in rectangular coordinates. From the displacement maps in both coordinate systems, the overall in-plane deformation of the specimen is shrinkage. In the normal strain maps, it can be seen that shrinkage was larger in the area close to the outer surface. This is due to the fast drying in the volume close to the exposed surface.

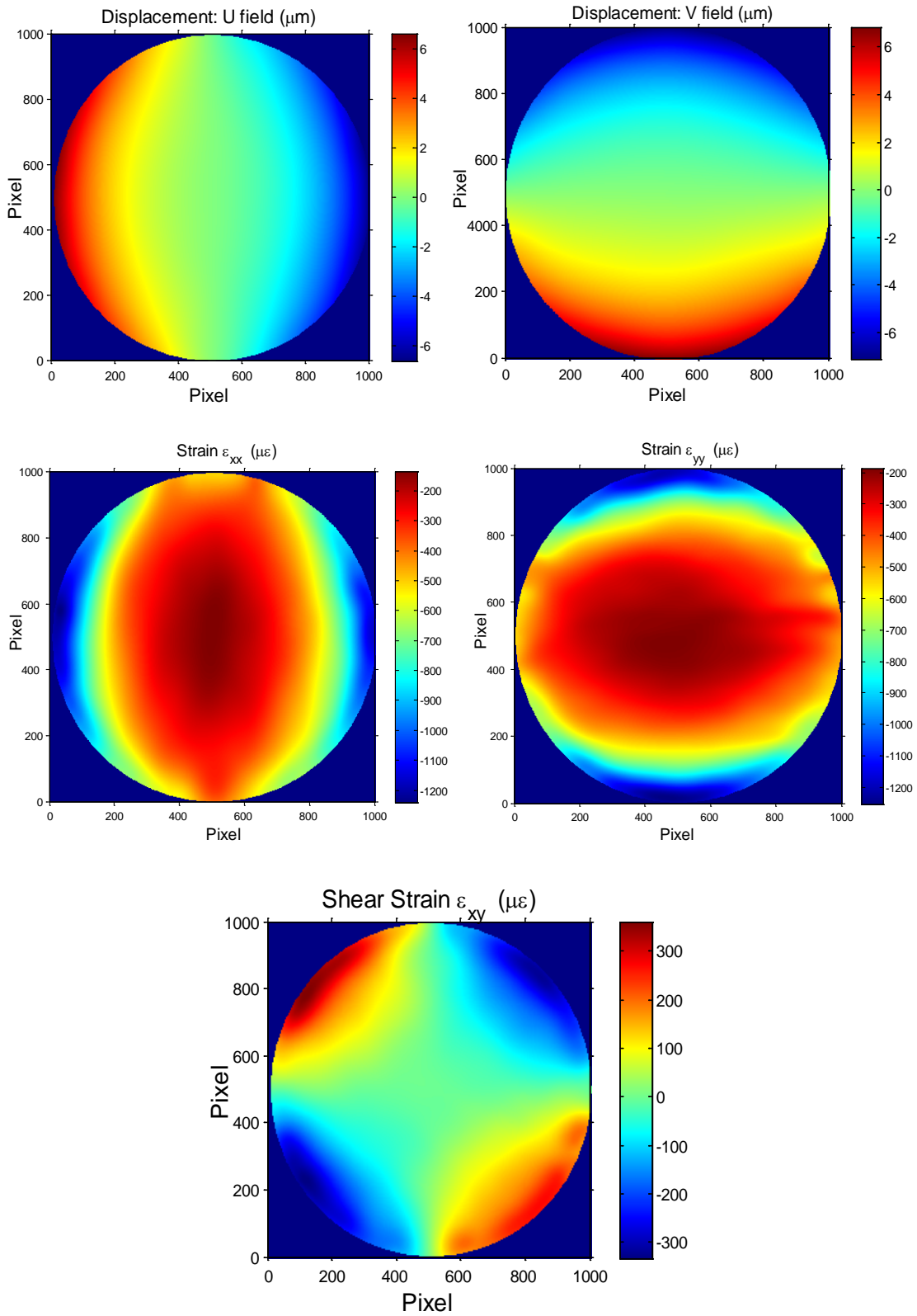


Figure 3-7. Full-field maps in x-y coordinate for day 2

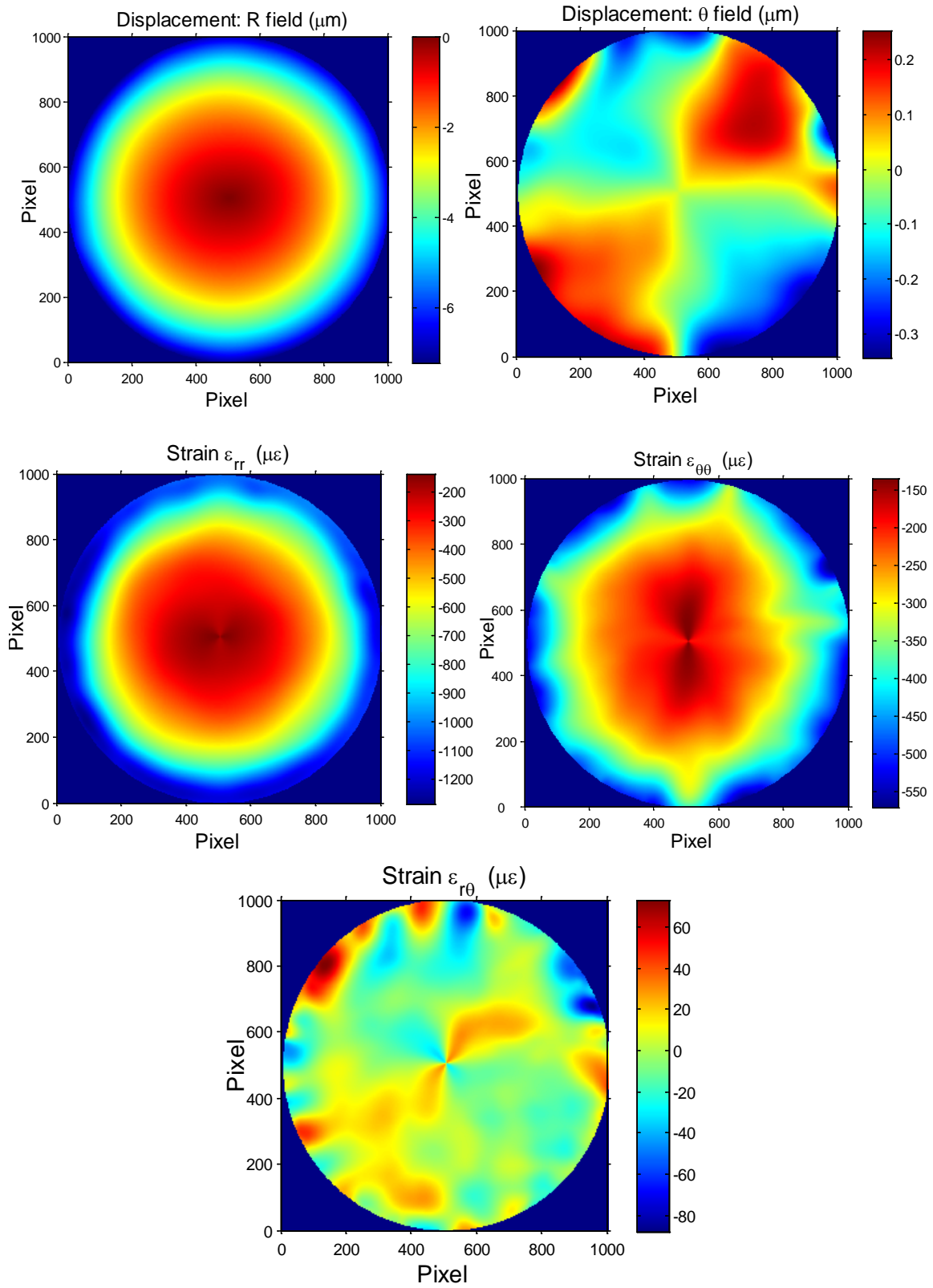


Figure 3-8. Full-field maps in polar coordinate for day 2

The shear strain map in x-y coordinate shows the maximum shear strain near the outer surface occurred in ± 45 and ± 135 degree directions. Also, along the vertical and horizontal centerlines, the value of the shear strain is zero. This can be easily explained by using Mohr's circle or shown later by finite element analysis. In polar coordinate, the angular displacement and shear strain should be zero due to axisymmetry. The result has shown their values are insignificant compared with those in other fields. However, their maps are not uniform due to noise.

Case2: 0% RH and room temperature

In this case, a generous amount of desiccates was used in the chamber to create as low RH as 0%. The moisture diffusing out of the specimen was absorbed by desiccates continuously, which maintained the RH0% in the chamber. Figure 3-9 and 3-10 are the U and V-field fringe patterns under 0% and room temperature. Likewise, both the fields have shown similar fringe distributions because of axisymmetry. Apparently, the fringe density or the number of fringes was much higher compared with the case of RH50%. This is due to the faster drying in the case of lower humidity. Likewise, the number of fringes increased with time. Also, the fringe density was higher in the area close to the outer surface than in the inner core from day 2 U & V-field fringe patterns. The inset has shown the quality and contrast are still high. Only day 7 full-field strain information is shown here as Figure 3-12. The automatic strain analysis system was still capable of resolving such fringe patterns of very high fringe density. The radial strain is as high as around $5000 \mu\epsilon$; the hoop strain is approximately $4000 \mu\epsilon$. Also, the shear strain map in x-y coordinate shows the maximum shear strain occurs near the outer surface in ± 45 and ± 135 degree directions with the magnitude of $500 \mu\epsilon$. The value of the shear strain in x-y coordinate is zero along the vertical and horizontal centerlines. The shear strain in polar coordinate was not significant.

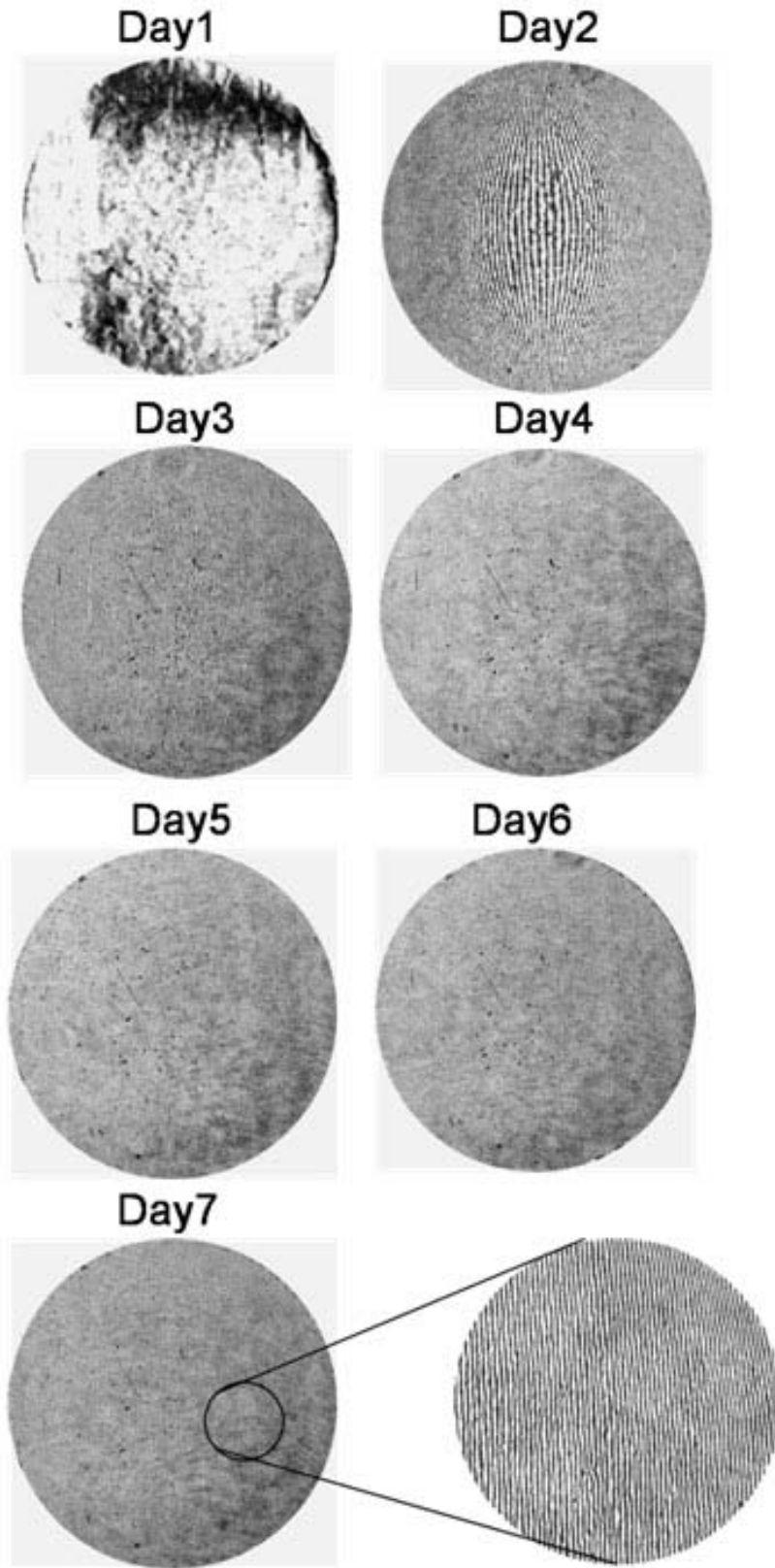


Figure 3-9. U-field Moiré fringe patterns under 0% RH and 23°C

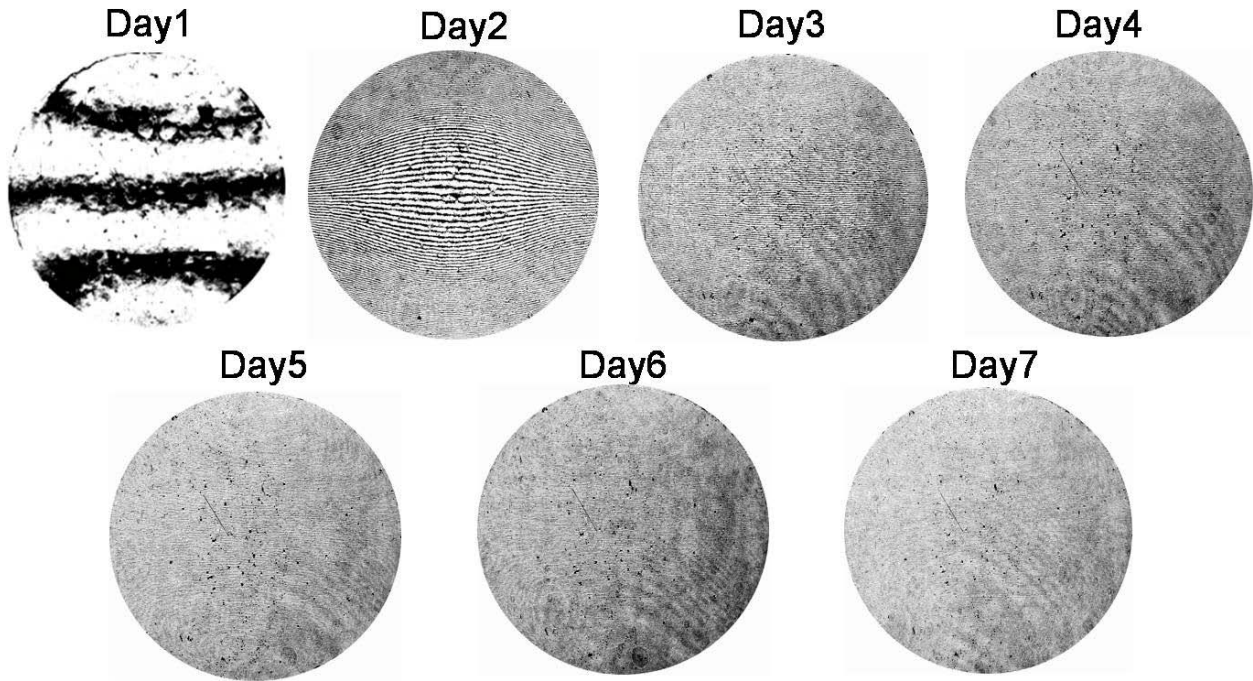


Figure 3-10. V-field Moiré fringe patterns under 0% RH and 23°C

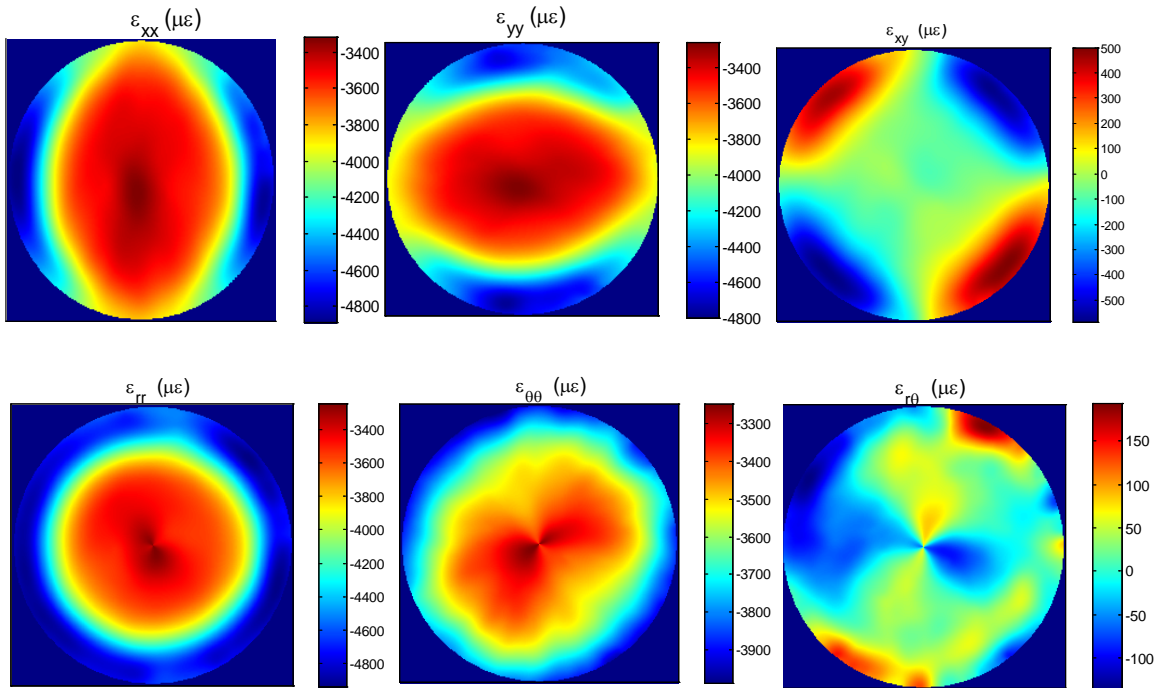


Figure 3-11. Full-field maps for day 7 under 0% RH and 23°C

Case3: 0% RH and 5°C

In this example, the chamber of 0% RH was maintained in the refrigerator. The low temperature of 5°C was very stable in the refrigerator. After the specimen was removed from the chamber, the measurement was not started immediately. Instead, it was placed on the optical table for around 5 minutes. This is to make the specimen return to room temperature and to reduce deformation from the thermal effect. Figure 3-12 and 13 are U & V-field moiré fringe patterns in RH0% and 5°C. The fringe density and the fringe number are not as large as those in the case of RH 0% and room temperature. It can be explained by the fact that low temperature reduces the rate of drying. Also, this example makes the fringe densities near the outer surface and in the inner core more distinguishable than the case of RH 0% and room temperature. It can be seen that the fringe density was higher near the outer surface.

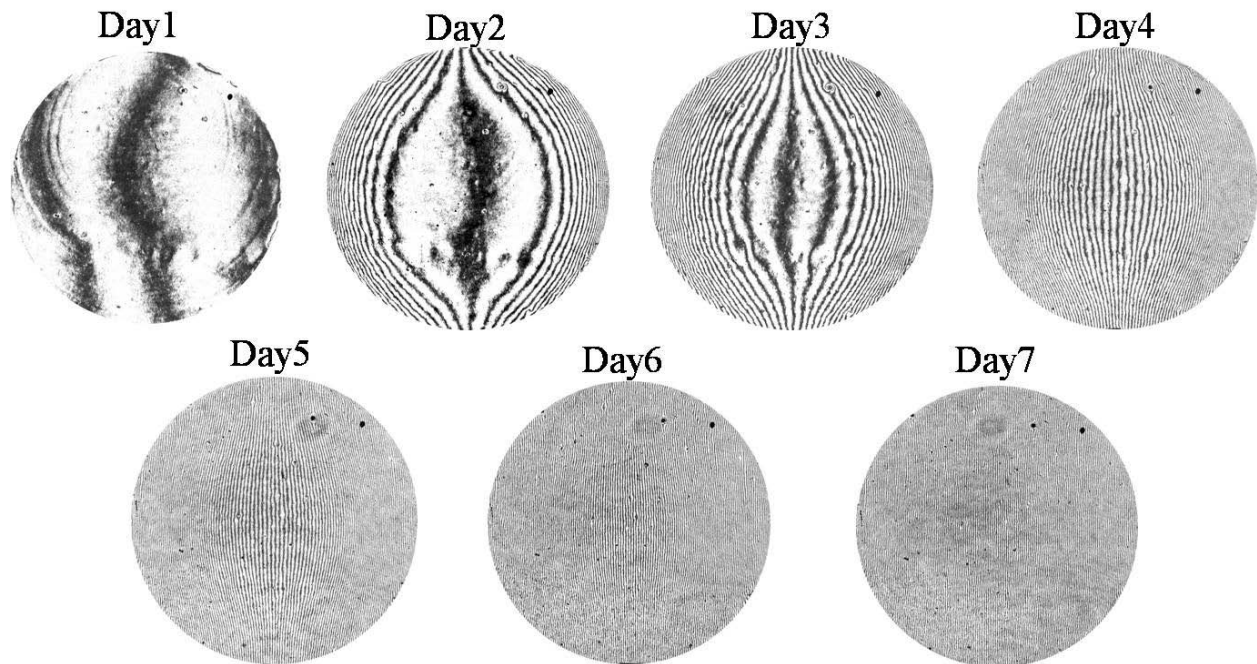


Figure 3-12. U-field Moiré fringe patterns under 0% RH and 5°C

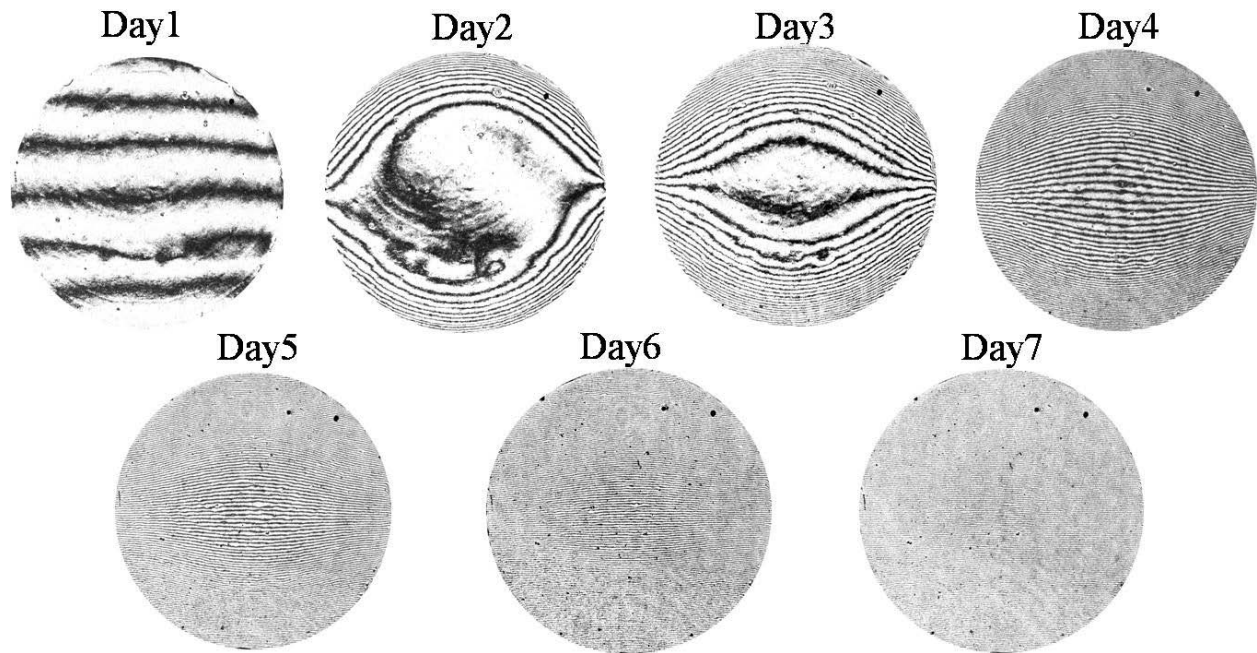
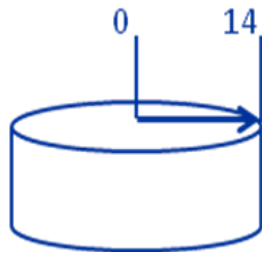
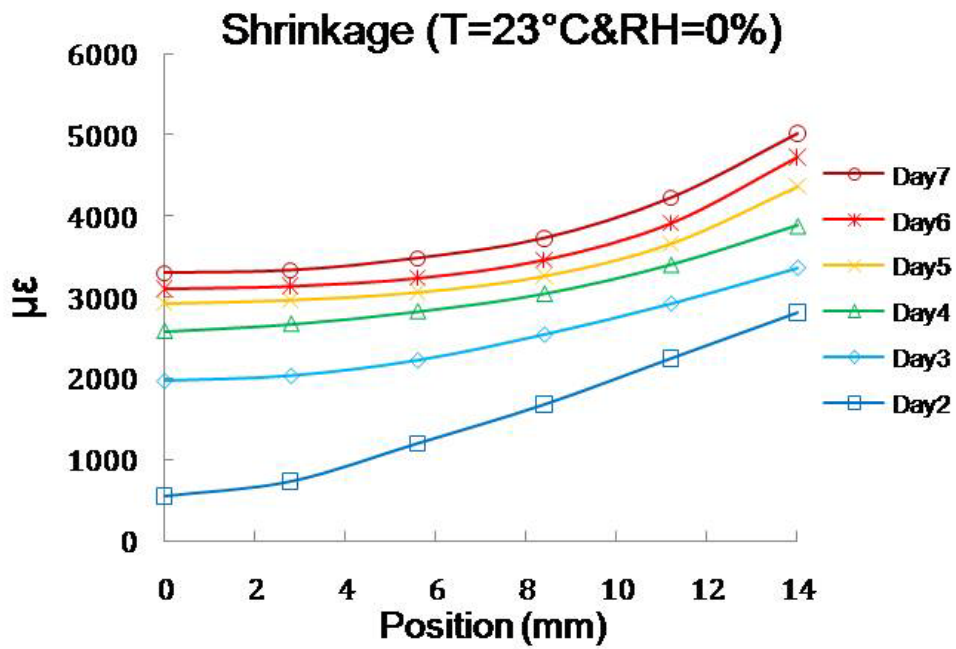
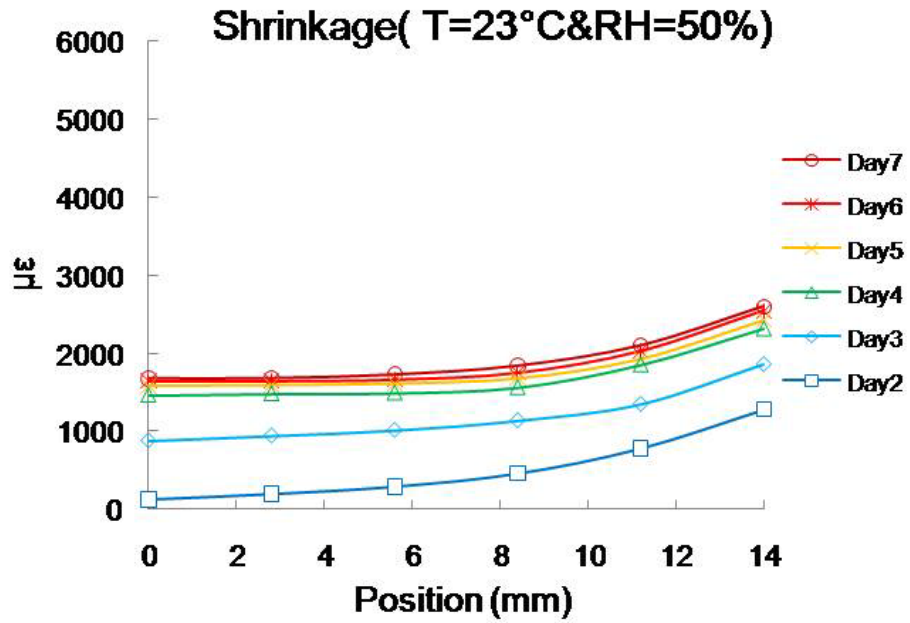
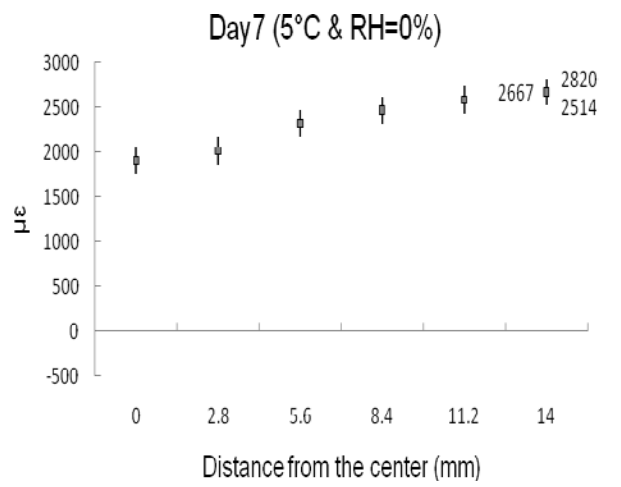
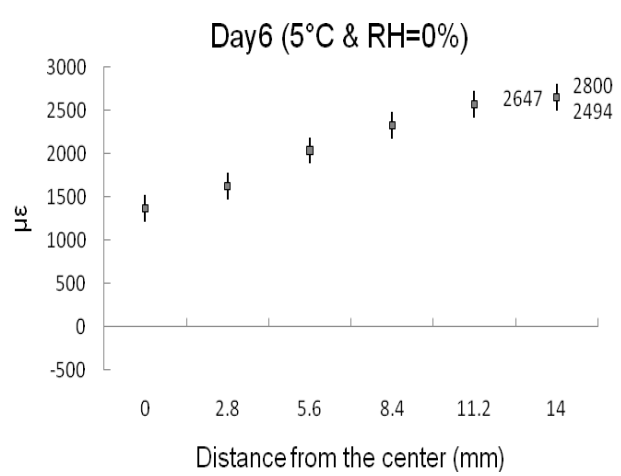
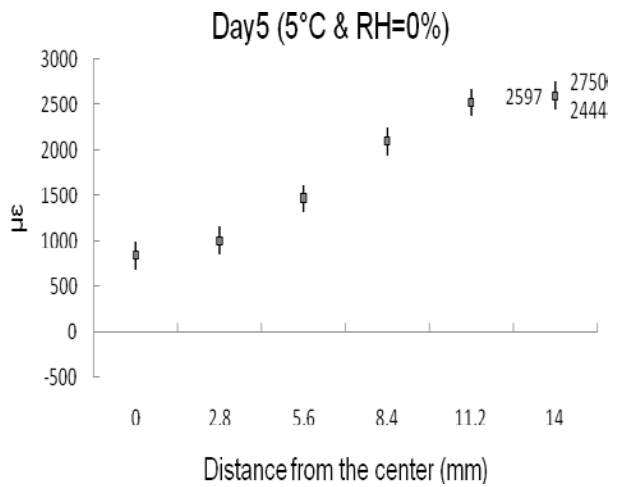
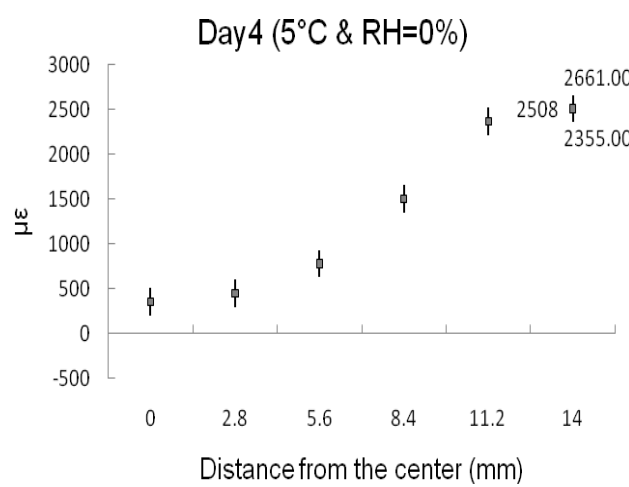
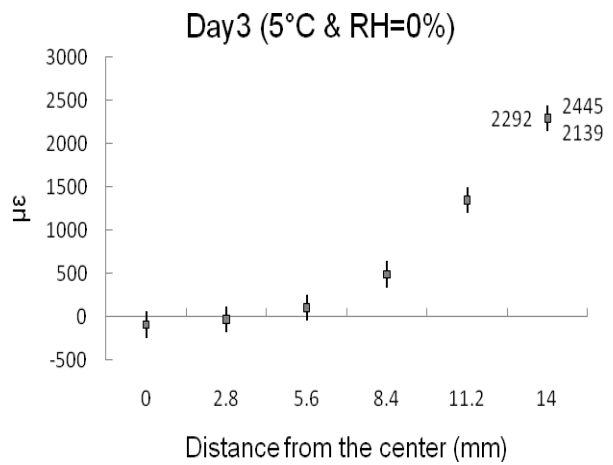
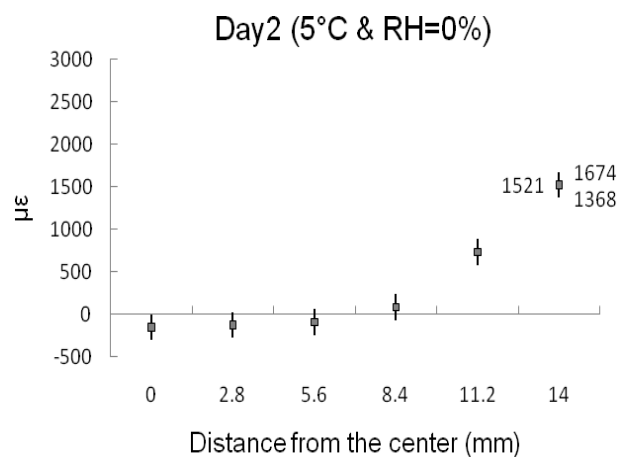


Figure 3-13. V-field Moiré fringe patterns under 0% RH and 5°C

The moiré fringe patterns in the case of 0% and 40°C are not shown here. But from the fringe patterns, it can be followed that drying is accelerated in high temperature environment. Likewise, the specimen was left on the optical table for about 5 minutes before the measurement.

Figure 3-14 shows the measured shrinkage from the center of the specimen to the outer surface on the grating surface for different combinations of humidity and temperature. Shrinkage on day 1 was not recorded because it is insignificant. Here, shrinkage is defined as the radial strain (ϵ_{rr}). Obviously, the results indicate that larger shrinkage occurred in the area close to the outer surface and shrinkage increased with time. Also, shrinkage is very sensitive to the drying conditions. In the hot and cold temperature conditions, the specimen might take at least 20 minutes rather than 5 minutes to return to room temperature. The experimental results in these two cases must incorporate some errors due to thermal effect. The typical value of thermal expansion coefficient for cement paste with $w/c = 0.5$ is $18\mu\epsilon/^\circ\text{C}$. Therefore, the results for the cold and hot conditions are demonstrated with the consideration of the errors.





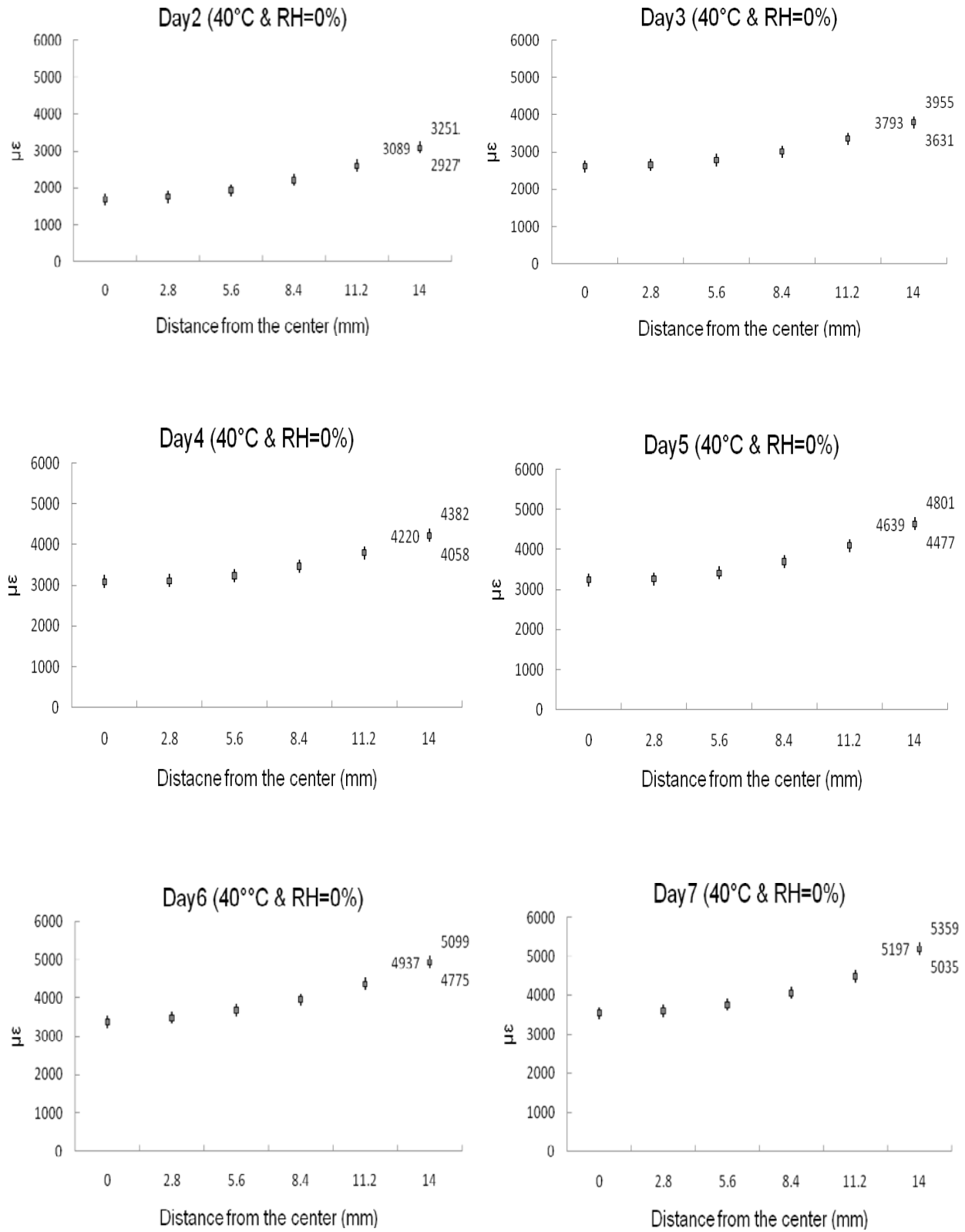


Figure 3-14. Measured shrinkage from center to outer surface

The evolution of the shrinkage in the case of 0% and 5°C is different. That might be related to the temperature variation over the cross section. The heat generated from the hydration process might cause much higher temperature in the inner core of the specimen than 5°C near the outer surface. This temperature variation would lead to differential material properties of shrinkage over the cross section. However, this phenomenon might not be influential in room temperature condition.

Case4: 100% RH and room temperature (23°C)

This example is worthy to be discussed here because the fringe distribution is quite different from the previous cases. The U and V-field moiré fringe patterns in Figure 3-15 and Figure 3-16 have shown that compared with RH=0 or 50%, there are not many fringes. That means the overall deformation is quite small. Also, the fringes curve outwardly instead of curving inwardly in the other cases. Furthermore, there are the enclosed fringes close to the outer surface from Day 5.

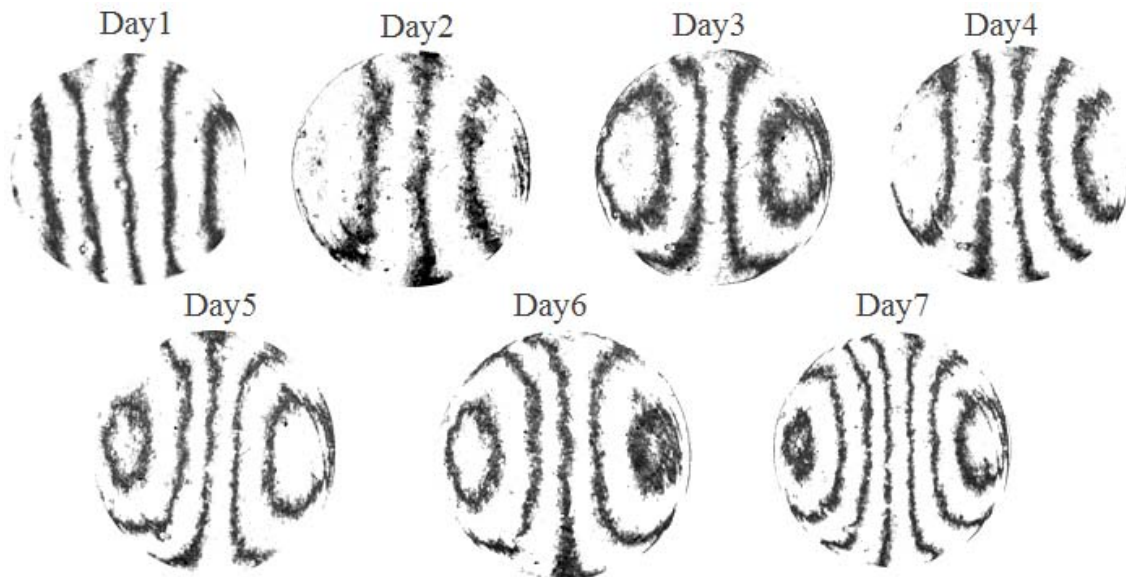


Figure 3-15. U-field Moiré fringe patterns under 100% RH and 23°C

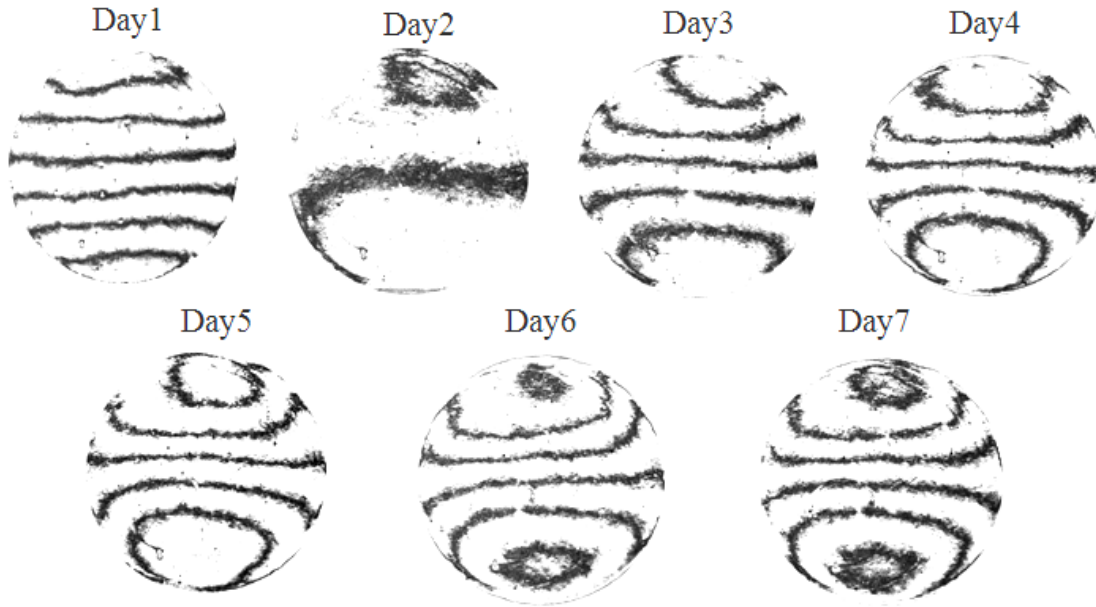


Figure 3-16. V-Field Moiré fringe patterns under 100% RH and 23°C

In order to understand the strain distribution in this special case, the U-field fringe pattern on day7 was analyzed. The result is shown in Figure 3-17 with the full-field displacement and strain information, and the plot of the strain distribution along the horizontal centerline. Globally, the concrete experienced shrinkage, which is determined according to the U-field displacement map. Locally, swelling occurred in the area close to the outer surface, which is due to the moisture gain from the surrounding environment. The inner core still experienced the shrinkage because of the hydration process. The locations of zero strain approximately correspond to the centers of the enclosed fringes. They are the positions to separate the swelling zone and the shrinkage zone.

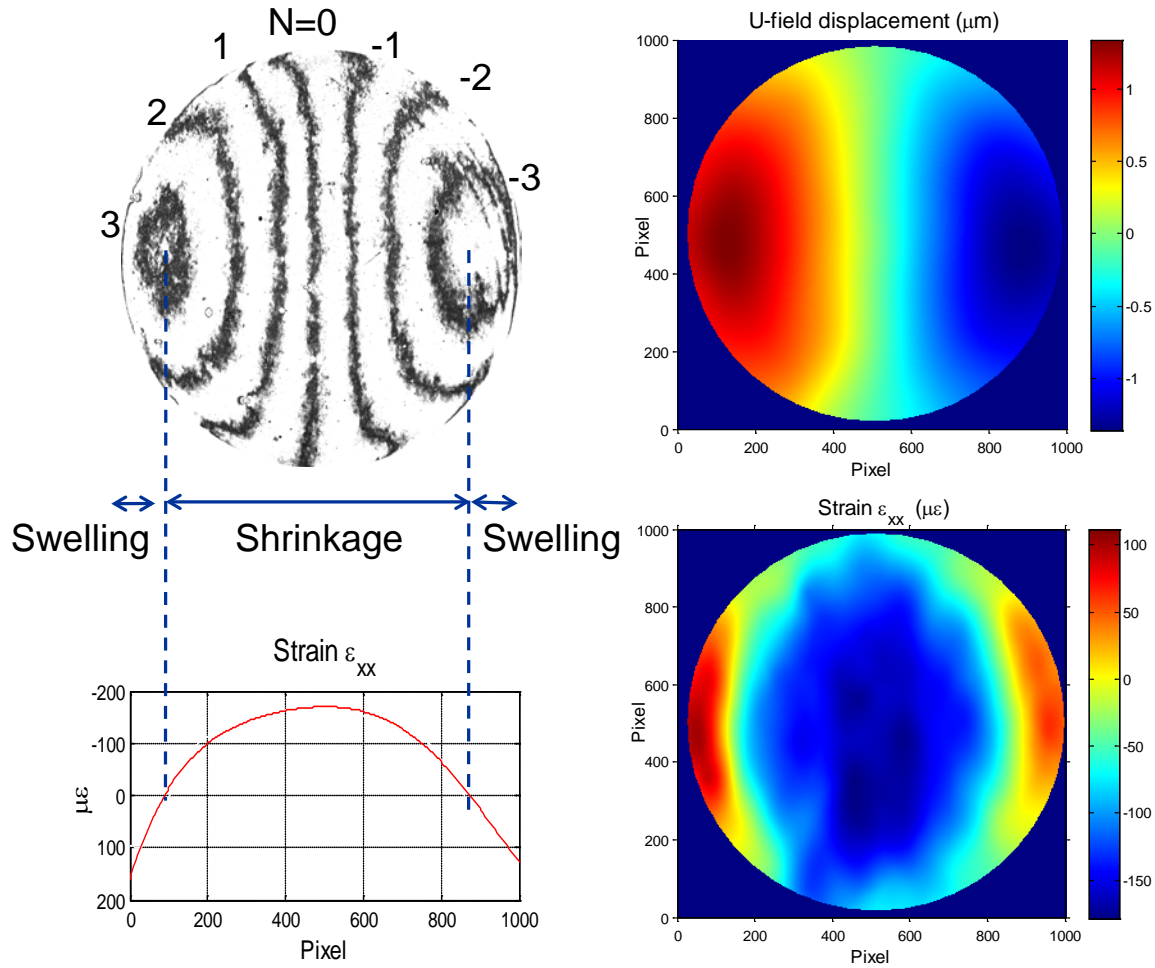


Figure 3-17. U-field displacement and strain maps for day

Three tests were attempted for both drying conditions of RH=0% and 100% in room temperature. Their results are recorded in Table 3-2 and 3-3 separately. The data strongly indicated the repeatability of this experimental technique.

Table 3-2. Shrinkage measurements under RH=0% and room temperature (23°C)

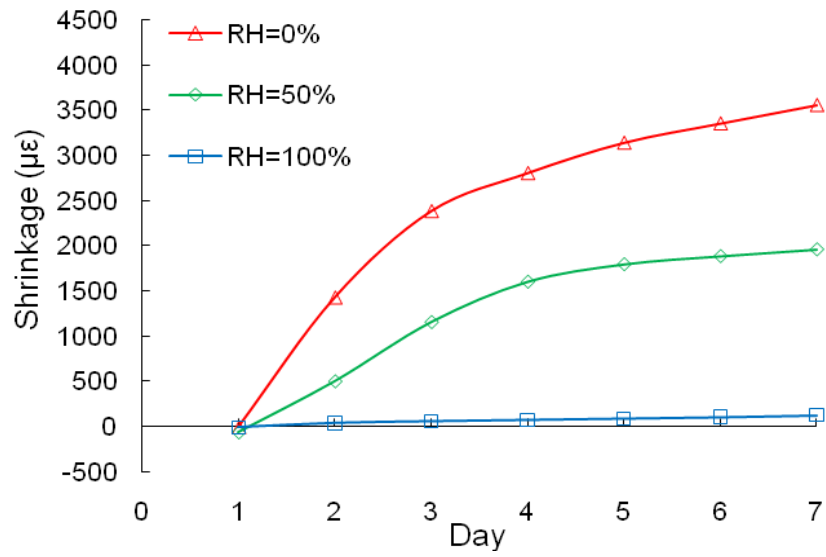
RH=0%	Specimen 1		Specimen 2		Specimen 3	
	Fringe number	Shrinkage (με)	Fringe number	Shrinkage	Fringe number	Shrinkage
Day1	0	0	0	0	-1	-14.88
Day2	80	1190.47	88	1309.52	87	1294.64
Day3	147	2187.50	156	2321.42	158	2351.19
Day4	175	2604.16	183	2723.21	186	2767.85
Day5	197	2931.54	206	3065.47	209	3110.11
Day6	210	3125.00	217	3229.16	224	3333.33
Day7	225	3348.21	230	3422.61	238	3541.66

Table 3-3. Shrinkage measurements under RH=100% and room temperature (23°C)

RH=100%	Specimen 1		Specimen 2		Specimen 3	
	Fringe number	Shrinkage ($\mu\epsilon$)	Fringe number	Shrinkage	Fringe number	Shrinkage
Day1	0	0	0	0	-2	-29.76
Day2	4	59.52	2	29.76	2	29.76
Day3	5	74.40	4	59.52	3	44.64
Day4	6	89.28	6	89.28	3	44.642
Day5	7	104.16	7	104.16	4	59.52
Day6	8	119.04	8	119.04	5	74.40
Day7	12	178.57	8	119.04	5	74.40

The experimental results can be displayed in terms of the averaged shrinkage or overall shrinkage. The averaged shrinkage was determined by dividing the diameter change by the original diameter (28mm). The diameter change was derived by counting the number of fringes within the horizontal centerline in the U field or within the vertical centerline in the V field, and then multiplying it with $0.417 \mu\text{m}/\text{per fringe}$. Figure 3-18 are the results concerning relative humidity and temperature effects on the shrinkage behavior of cement pastes. Figure 3-19 were the results regarding to W/C ratio and size effects on the shrinkage behavior of cement pastes. The data points are the measurements of the averaged shrinkage. From the results, it can be known that in the surrounding environment of low humidity and high temperature concrete experiences larger shrinkage. As a result, larger tensile stress is developed when the concrete structure is constrained. This increases the possibility of cracking occurrence in the structure and reduces the durability of the structure.

Relative Humidity Effect ($T=23\pm 1^\circ\text{C}$)



Temperature Effect (RH=0%)

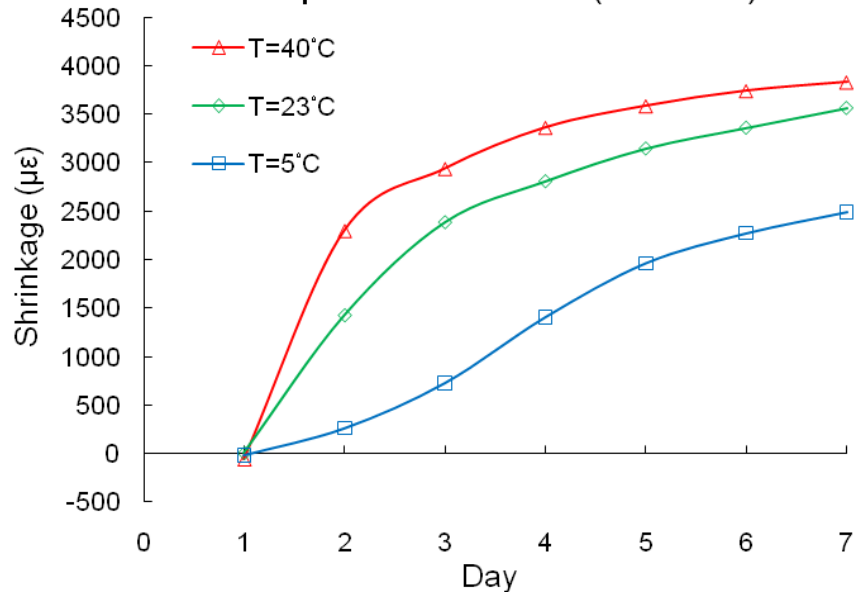


Figure 3-18. Relative humidity and temperature effect

3.4.2 W/C ratio and Size Effects

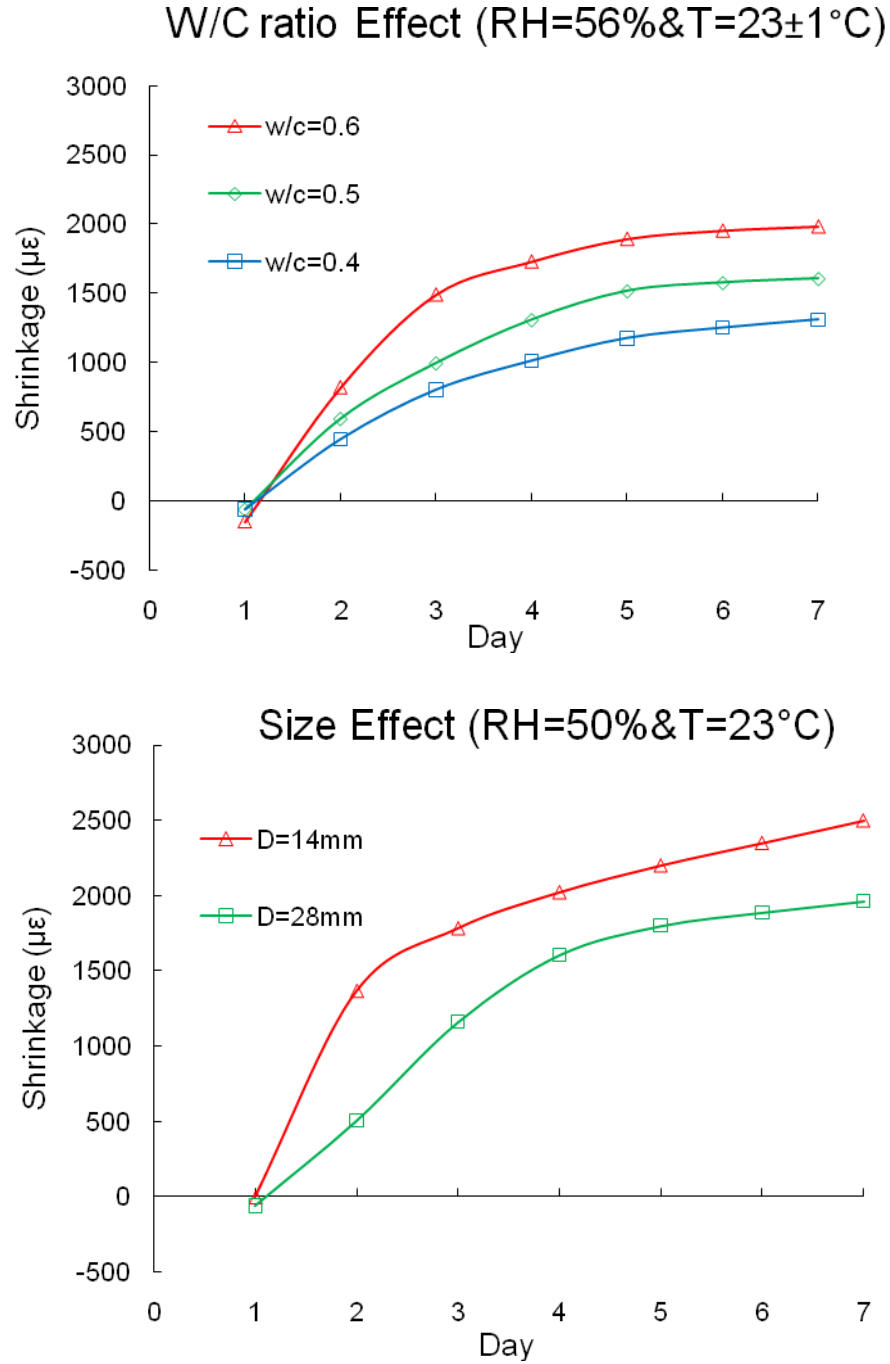


Figure 3-19. w/c and size effects on averaged shrinkage of cement pastes

3.4.3 Aggregate Effect

The shrinkage behavior of the specimens with aggregates was explored in the same experimental technique. Either fine or coarse aggregates (sand or gravel) were added to cement

pastes to investigate how aggregates affected moiré fringe patterns and shrinkage behavior. Some examples of moiré fringes patterns were shown and analyzed. Both aggregate quantity and humidity effects were tested.

3.4.3.1 Fine aggregate

The mortar specimens were made by adding ASTM C778 sand to cement pastes ($w/c=0.5$).

The specimens were stored in the drying conditions of relative humidity 0% and room temperature. Figure 3-20 was The U-field moiré fringe patterns for sand/cement ratio (s/c) of 37.5%. The V-field fringe patterns were not shown here due to the same shape as U field except 90° rotation. The inset revealed the fringes were affected by the existence of the sand particles. Sands seem to lower the fringe density or reduce the shrinkage locally. However, hand-counting the number of fringes was not an issue while determining the averaged shrinkage.

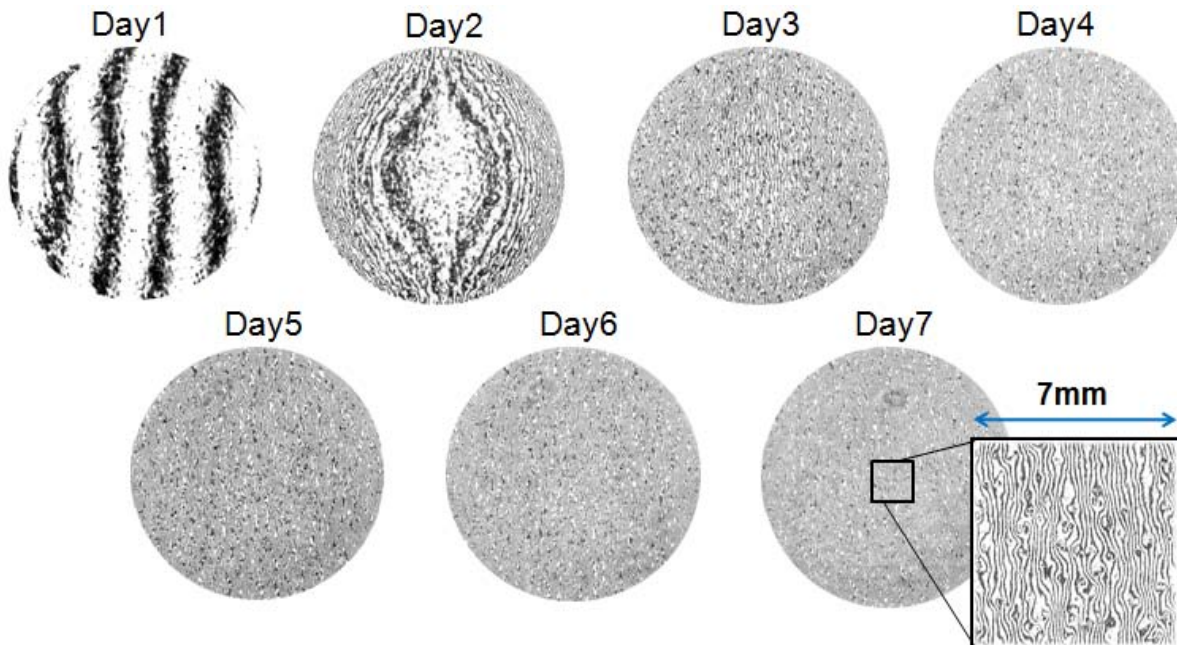


Figure 3-20. U-field moiré fringe patterns for mortar with $s/c=37.5\%$

The strain analysis for Day 2 fringe patterns was shown as Figure 3-21. The maps might be too smooth to reflect the actual strain information. However, it was still acceptable and

reasonable while only considering the strain distribution in a more global sense. Likewise, shrinkage was larger in the area close to the outer surface than in the inner core.

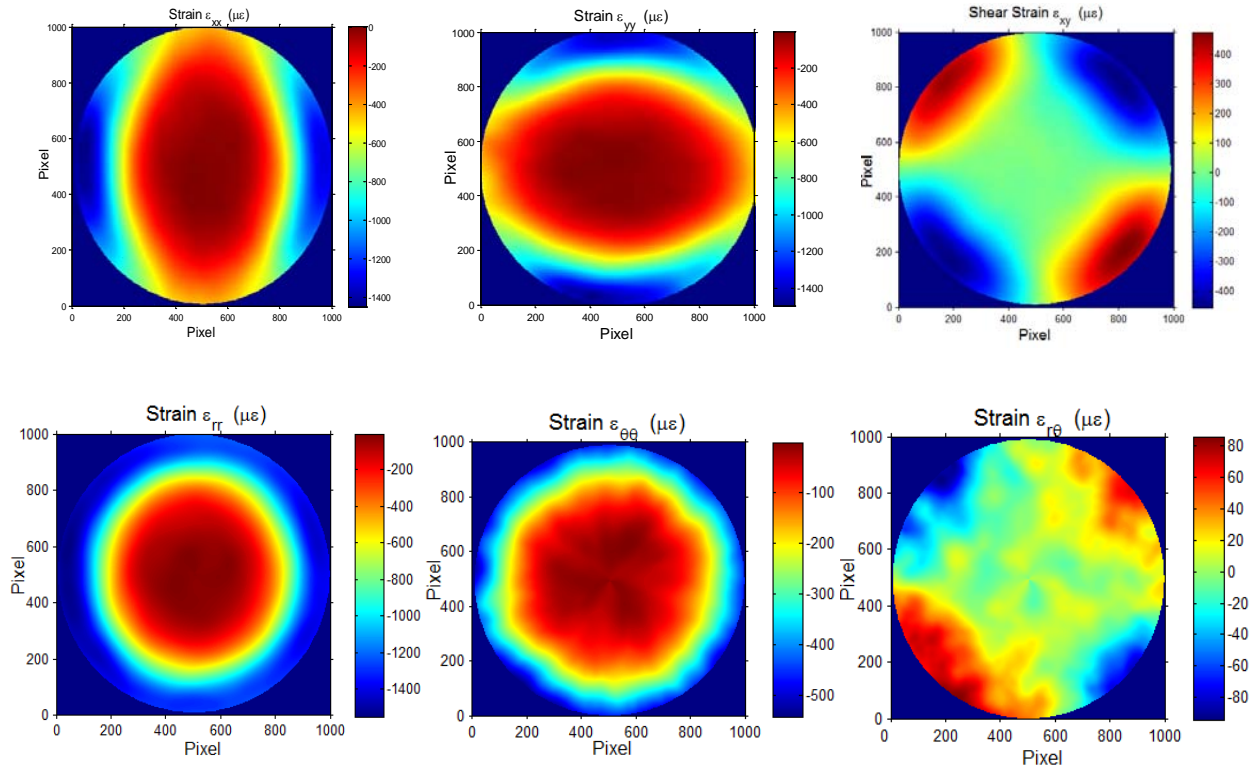


Figure 3-21. Strain information for mortar with $s/c=37.5\%$ on day 2

The displacement maps in both coordinate systems were shown in Figure 3-22. The radius displacement field was used to verify the angular strain field by the equation U_r/r .

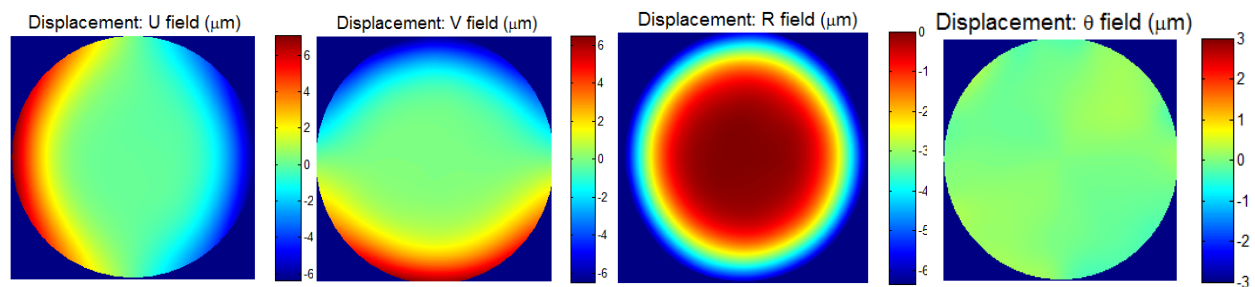


Figure 3-22. Displacement maps for mortar with $s/c=37.5\%$ on day 2

The specimen with $s/c= 75\%$ was also tested. Day 7 U & V-field moiré fringe patterns and fringe patterns with rotation carriers were shown as in Figure 3-23. The inset revealed counting

fringes became challenging due to the irregularity and distortion of the fringes. However, the rotation carriers could be added to make it possible to count fringes for the determination of the averaged shrinkage. Also, this would not change the full-field strain distribution if choosing the moiré fringe patterns with rotation carriers for analysis.

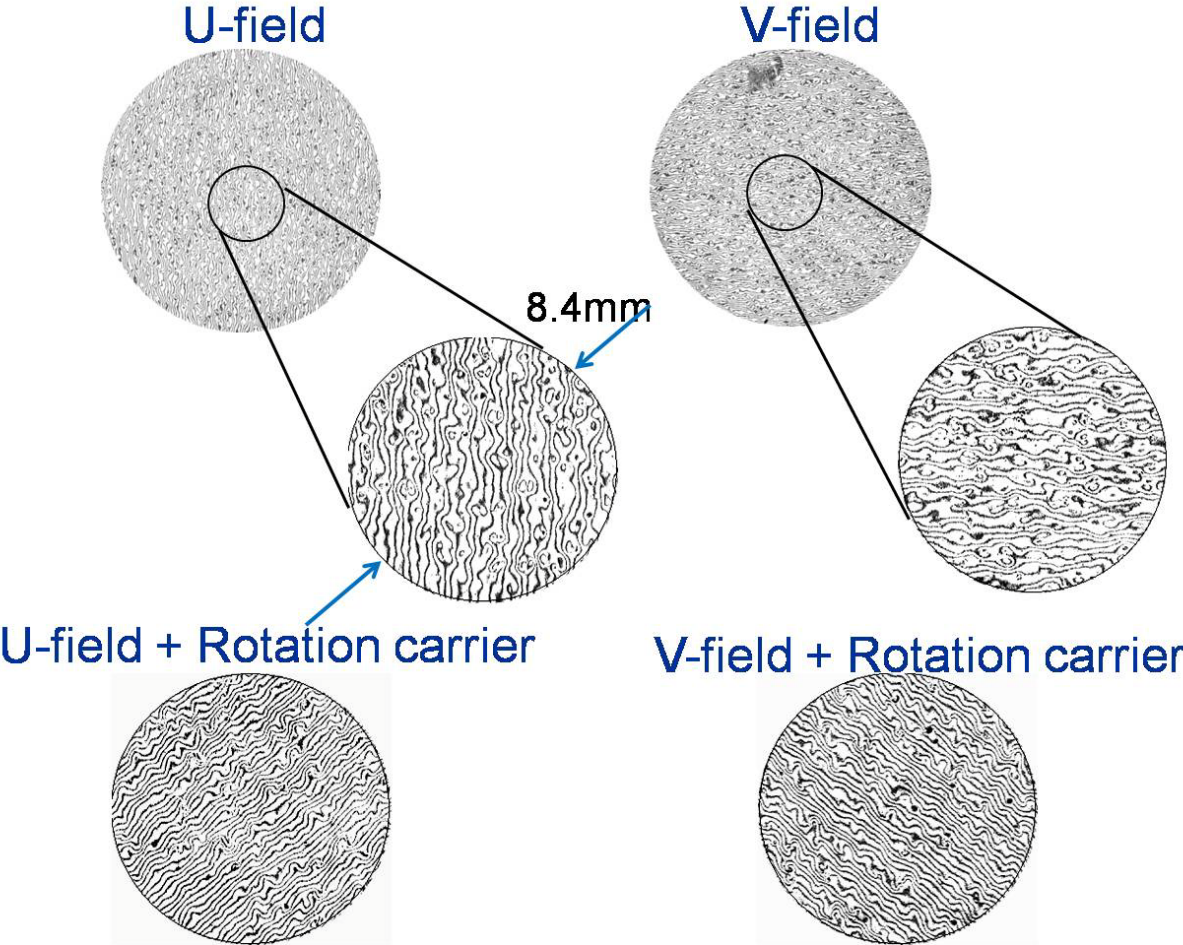
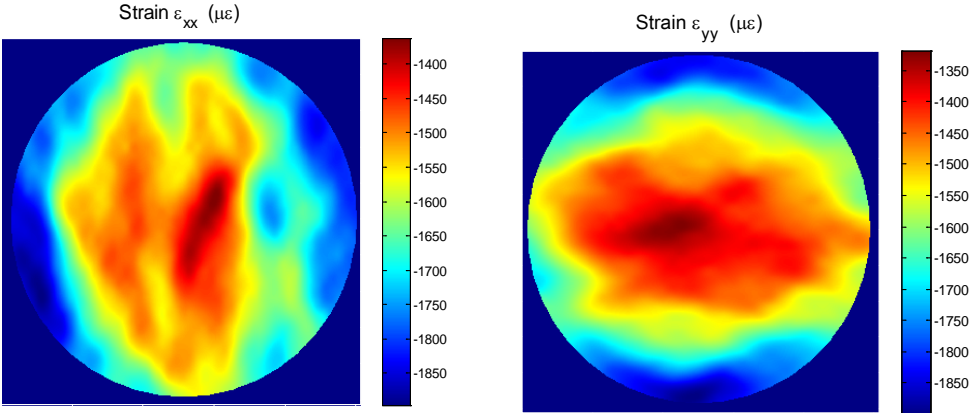


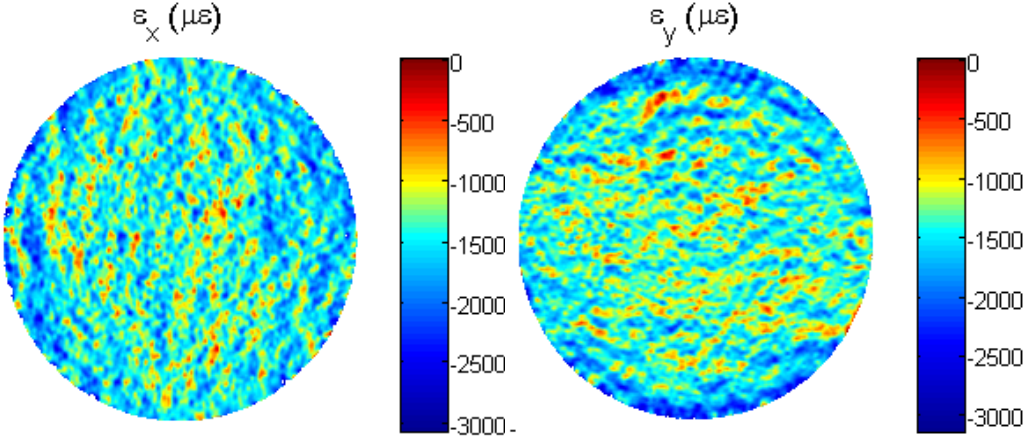
Figure 3-23. Moiré fringe patterns for mortar with $s/c=75\%$ on day 7

Theoretically, the full-field strain maps could be obtained with different sizes of gauge lengths in the automatic fringe analysis system. However, if the selected gauge length is too large, the maps will be too smooth to exactly reflect real local information like the maps in the previous case of $s/c=37.5\%$. Therefore, in this case, Day 7 moiré fringe patterns were analyzed with both small and large gauge lengths. The result shown in Figure 3-24 revealed two things.

Firstly, there still existed larger shrinkage in the area close to the outer surface. Secondly, from 3-24(b), the shrinkage at many local points was smaller due to the existence of the randomly distributed sands. The strain information from the analysis with the small gauge length might display the strain distribution more properly.



(a) Large gauge length (25 pixels)



(b) Small gauge length (8 pixels)

Figure 3-24. Full-field normal strain maps with both (a) large and (b) small gauge lengths for the mortar specimen of s/c=75% on Day 7

Figure 3-25 shows both fine aggregate quantity and RH effects on the averaged shrinkage of mortar specimens. Obviously, the more the quantities of sands, the lower the measured averaged shrinkage. Also, averaged shrinkage increased with the decreased relative humidity.

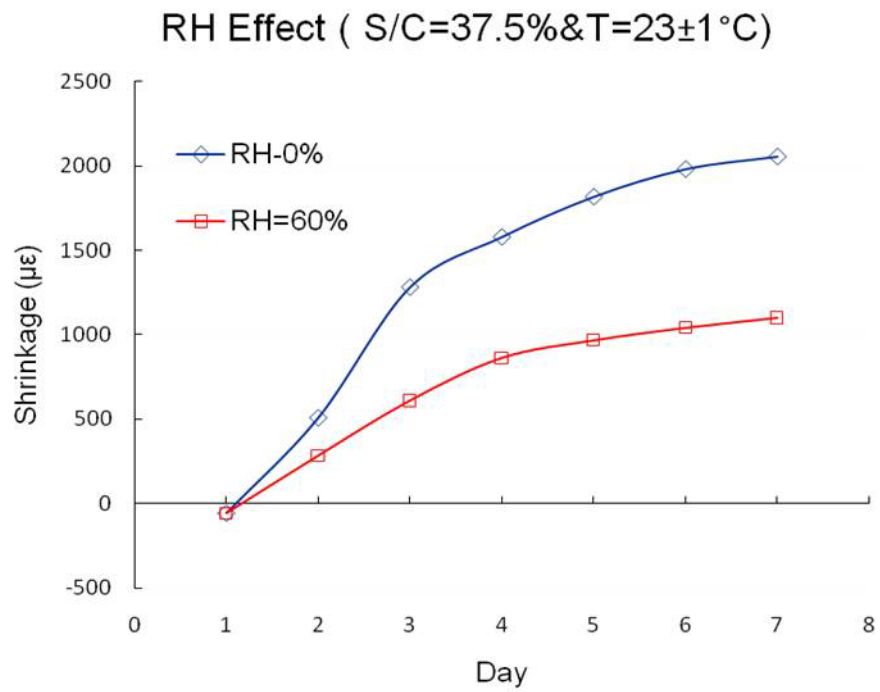
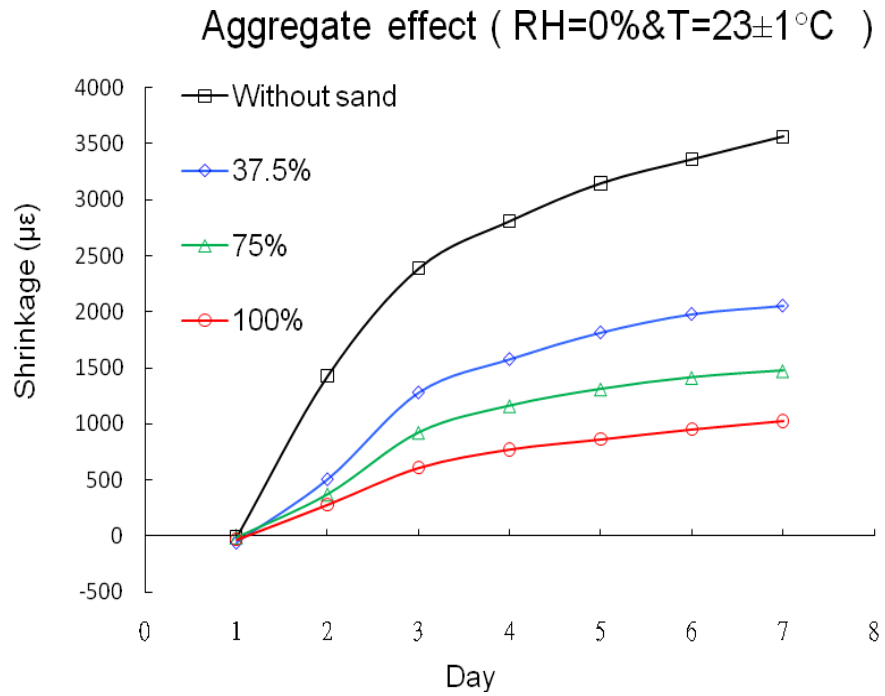


Figure 3-25. Aggregate quantity and RH effects on average shrinkage of mortar specimens

3.4.3.2 Coarse aggregate

Gravel was embedded into the cement paste ($w/c=0.5$), but did not contact with the grating. The arrangement of the gravel is shown as Figure 3-26 with the side view and the top view. The specimen was stored in relative humidity 0% and room temperature.

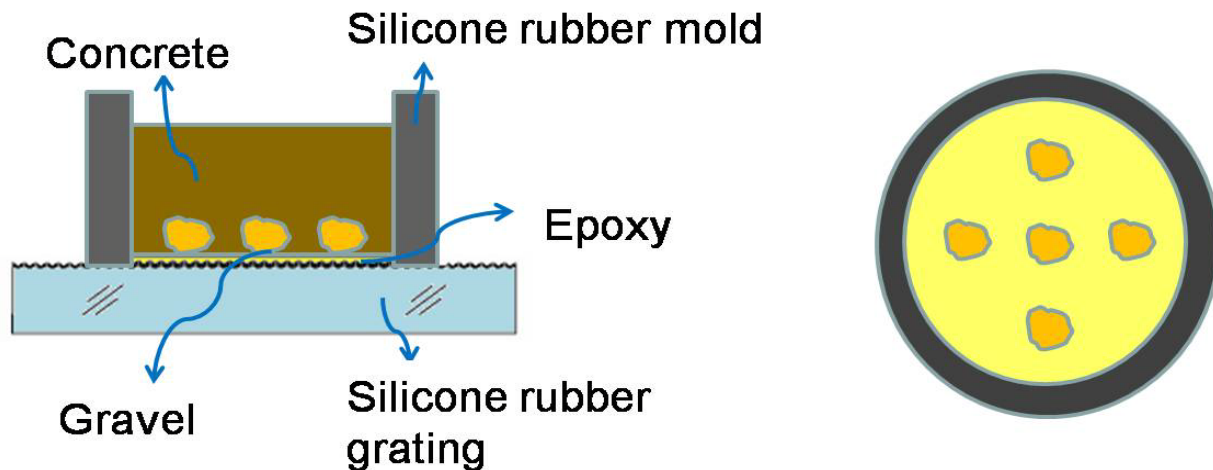


Figure 3-26. Side and top views of gravel test

The moiré fringe patterns from Day 1 to Day 5 were recorded. But only day 5 U & V-field moiré fringe patterns are shown here in Figure 3-27. There were some areas of the lower fringe density as remarked by the blue boxes. The insets indicated the fringes in the blue box. These areas corresponded to the locations of the embedded gravels. There was a crack going on in the area circled by the red line. This was due to the constraint from the embedded gravels.

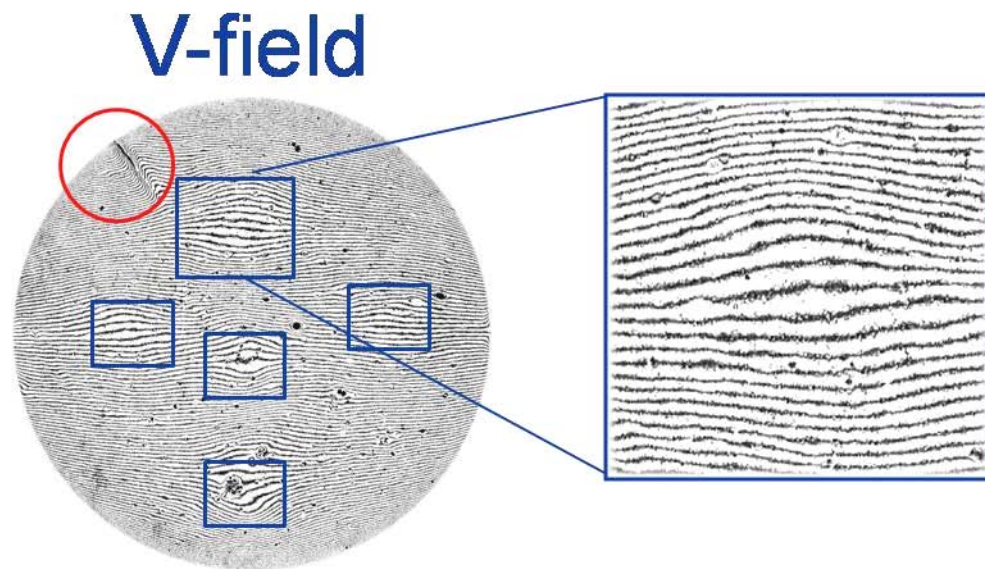
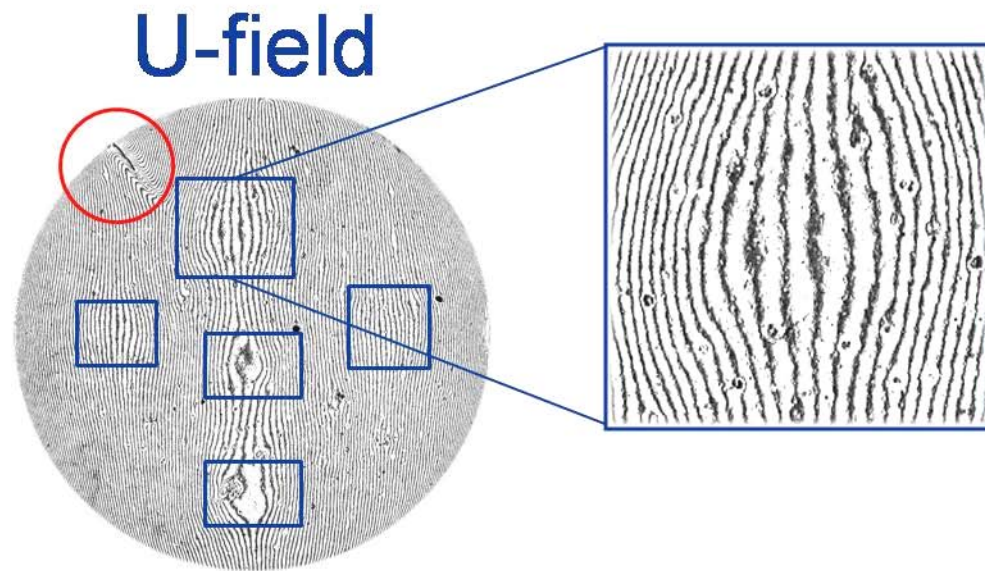


Figure 3-27. Day 5 moiré fringe patterns for the gravel test

The strain analysis was performed and the results were shown in Figure 3-28. Clearly, the locations of the gravels have the lower shrinkage. The plots just displayed the normal strain distributions along the horizontal centerline in U field and along the vertical centerline in V field.

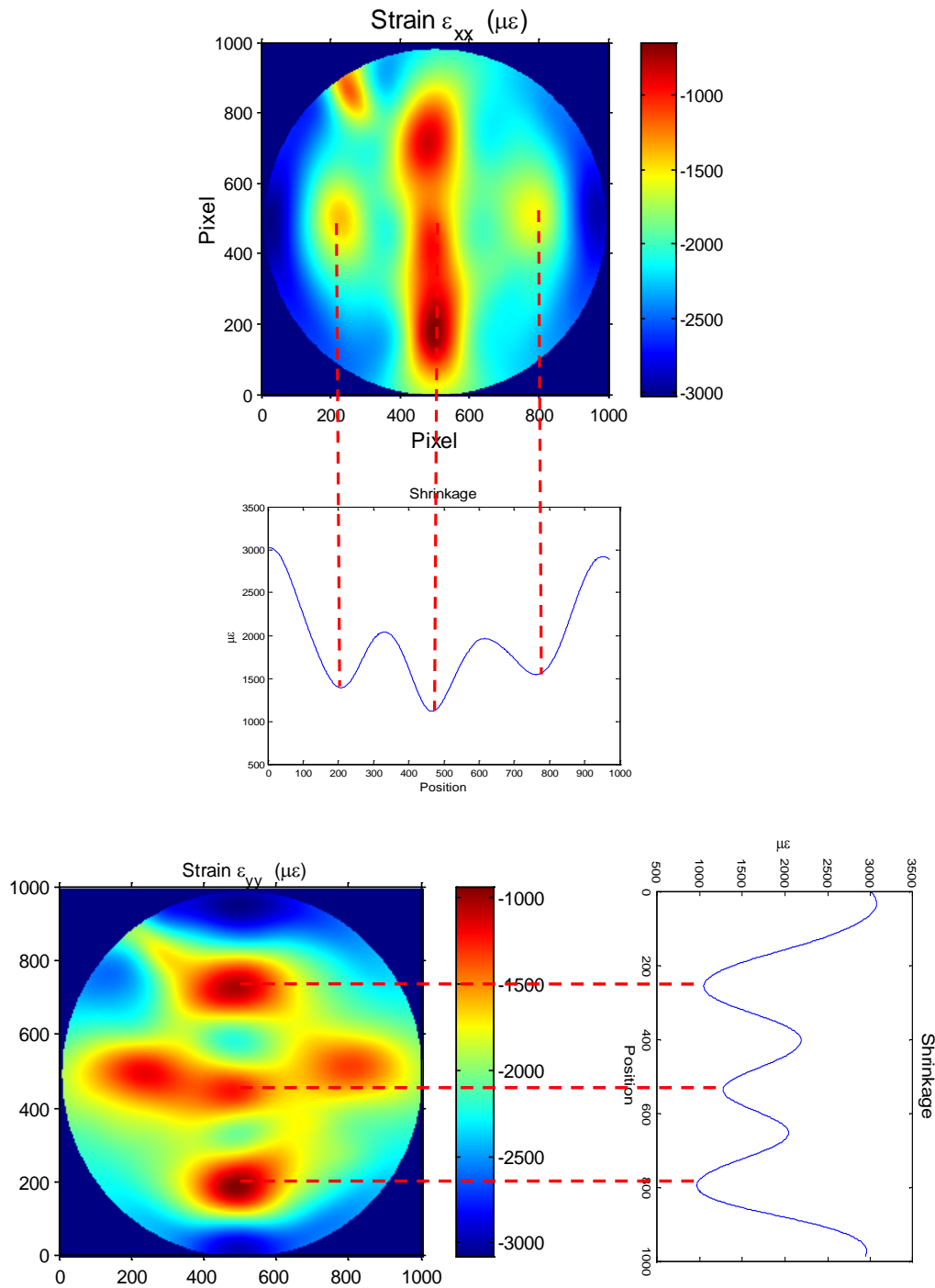


Figure 3-28. The Strain analysis for gravel test

3.4.4 Autogenous Shrinkage Measurements in Sealed Conditions

In order to explore Autogenous shrinkage only, drying shrinkage from moisture loss needs to be prevented. A method of combining CRM and the sealing of the entire specimen was used to measure autogenous shrinkage. This method could offer the information concerning the contribution of autogenous shrinkage to overall shrinkage. Therefore, instead of placing the specimen inside of the chamber after demold, the entire specimen was sealed with aluminum sheets first and then plastic wrap to prevent the exchange of moisture with the surrounding environments. Many sealing methods have been attempted, but this one could prevent the grating on the surface of the specimen from damage. Every day the specimen was unsealed, a quick measurement was taken, and then the specimen was sealed again after testing. Humidity is no longer a factor to autogenous shrinkage measurement, but temperature is still an influential one. The tests were done on both the sealed cement paste specimens and the mortar specimen. For the test on the mortar specimen, one modified sealing method was used, which could work out some issues in the original sealing method.

3.4.4.1 Sealed cement paste specimens

According to literature, autogenous shrinkage is not significant when w/c ratio is above 0.4. Hence, the cement paste specimen with w/c ratio=0.4 was tested first. The U&V-field moiré fringe patterns for w/c=0.4 in room temperature were shown as Figure 3-29 and 3-30. It was noticed that the fringes were quite uniformly-spaced in both the fields. That was because drying shrinkage which is differential over the cross section no longer existed in this case and the measured shrinkage only came from the hydration process.

The day 7 U-field fringe pattern was analyzed as in Figure 3-31. Exactly uniform strain maps could not be obtained through the automated fringe analysis because of noise. However, the normal strain map in U field has shown very uniform strain over the entire field when the

scale was enlarged. Furthermore, by obtaining displacement fields and plotting displacement distribution along the horizontal centerline in U field, it was found that the slope was very close to constant, which means the strain was very uniform. And the shear strain was very uniform and close to zero over the entire field when the scale was enlarged.

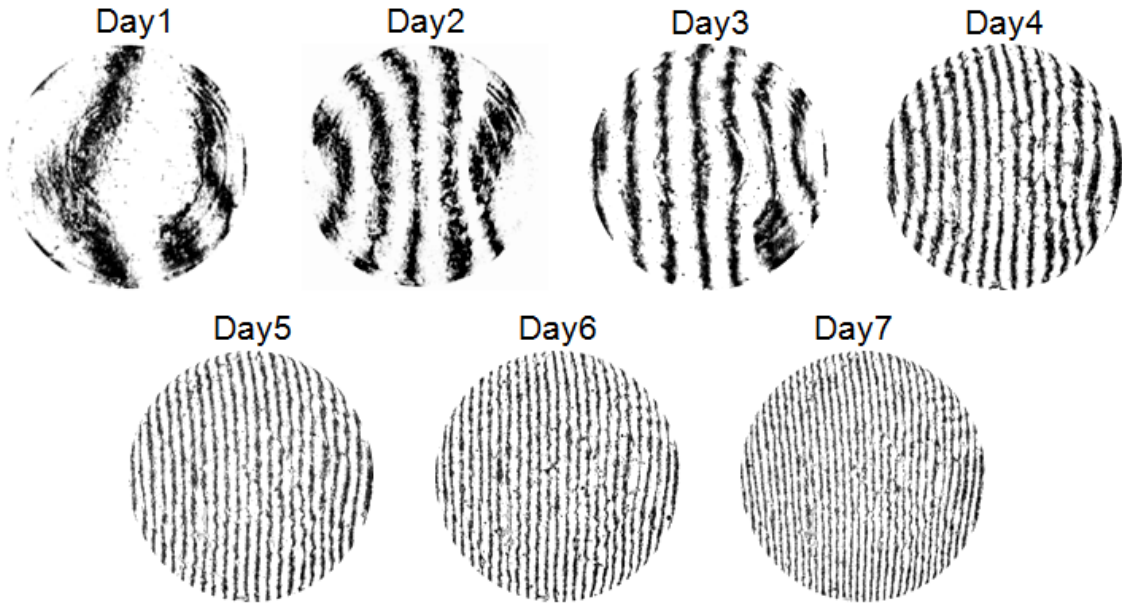


Figure 3-29. U-field moiré fringe patterns for $w/c = 0.4$ in room temperature

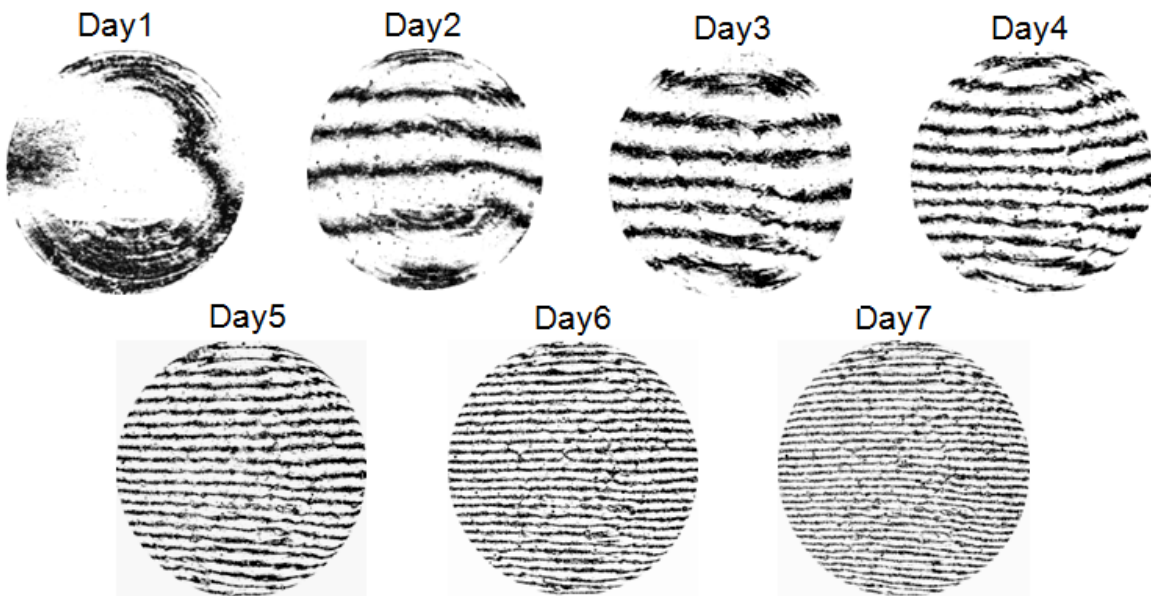


Figure 3-30. V-field moiré fringe patterns for $w/c = 0.4$ in room temperature

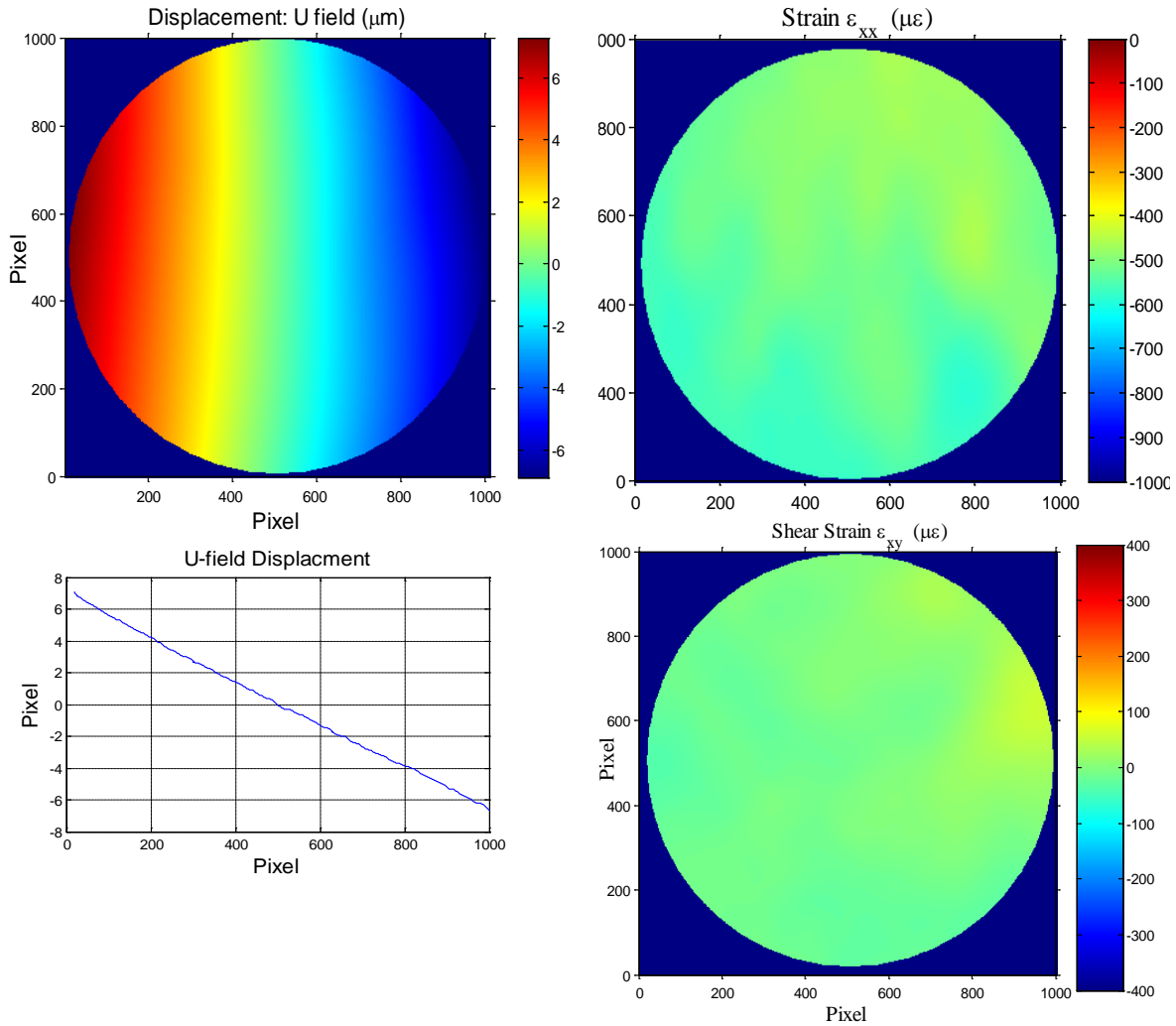


Figure 3-31. Day 7 U-field displacement for the sealed specimen with $w/c=0.4$ in x-y coordinate

Two influential factors, w/c ratio and temperature, were investigated and the results were shown in Figure 3-32. It can be seen that the use of concrete with w/c below 0.4 or in higher temperature might face an issue. Autogenous shrinkage in such cases has significant contribution. As a consequence, this might induce cracking in the concrete structure and reduces its durability.

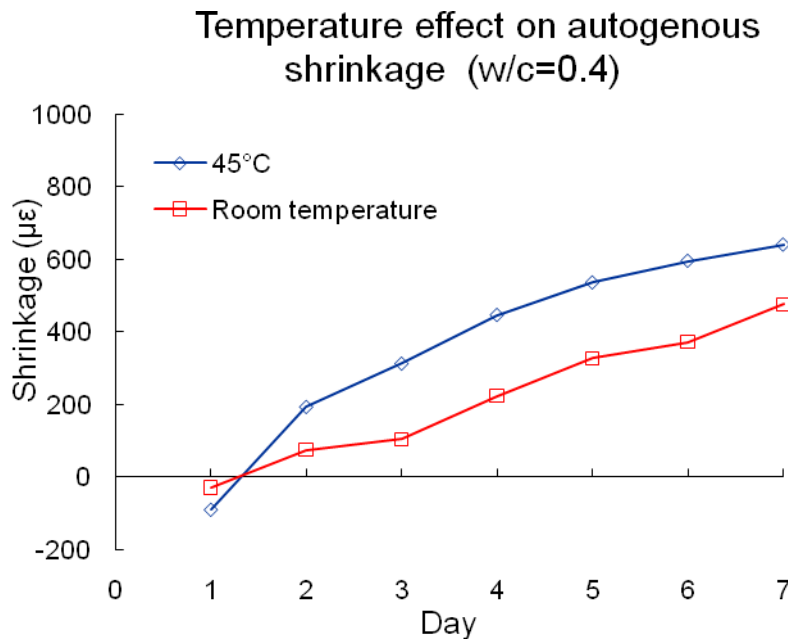
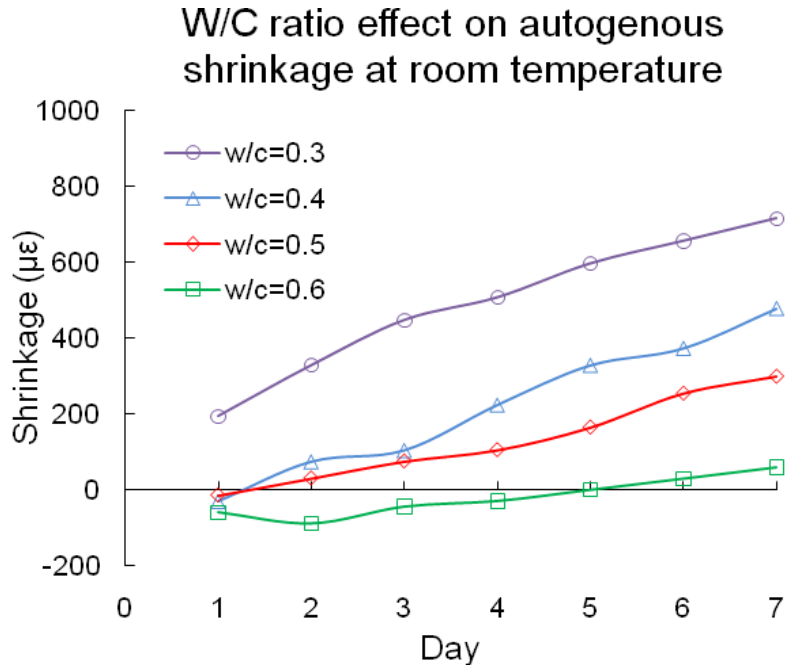


Figure 3-32. W/C ratio and temperature effects on sealed specimen shrinkage

The results show autogenous shrinkage increased with decreased w/c ratio and with increased temperature. For w/c=0.3, the shrinkage increased significantly. Even the measurement on day 1 showed the shrinkage rather than the swelling. This was due to strong hydration process in the earlier time of curing. For w/c=0.5 or 0.6, the shrinkage is not significant. The fringe

patterns for $w/c=0.6$ included in the appendix were to show the insignificant deformations. The results correspond to the trend of autogenous shrinkage documented in the literature. Therefore, the contribution of chemical shrinkage to overall shrinkage increases with the decrease in the w/c ratio. The autogenous shrinkage is a concern in the use of high performance concrete materials. On the other hand, higher temperature could accelerate the hydration process and induce larger shrinkage. The day 6 fringe patterns are analyzed and the full-field maps are shown in terms of polar coordinate in Figure 5. The radial displacement and shear strain maps are not shown here because they are supposed to be zero. Also, it can be seen that the radial strain is similar to the angular strain.

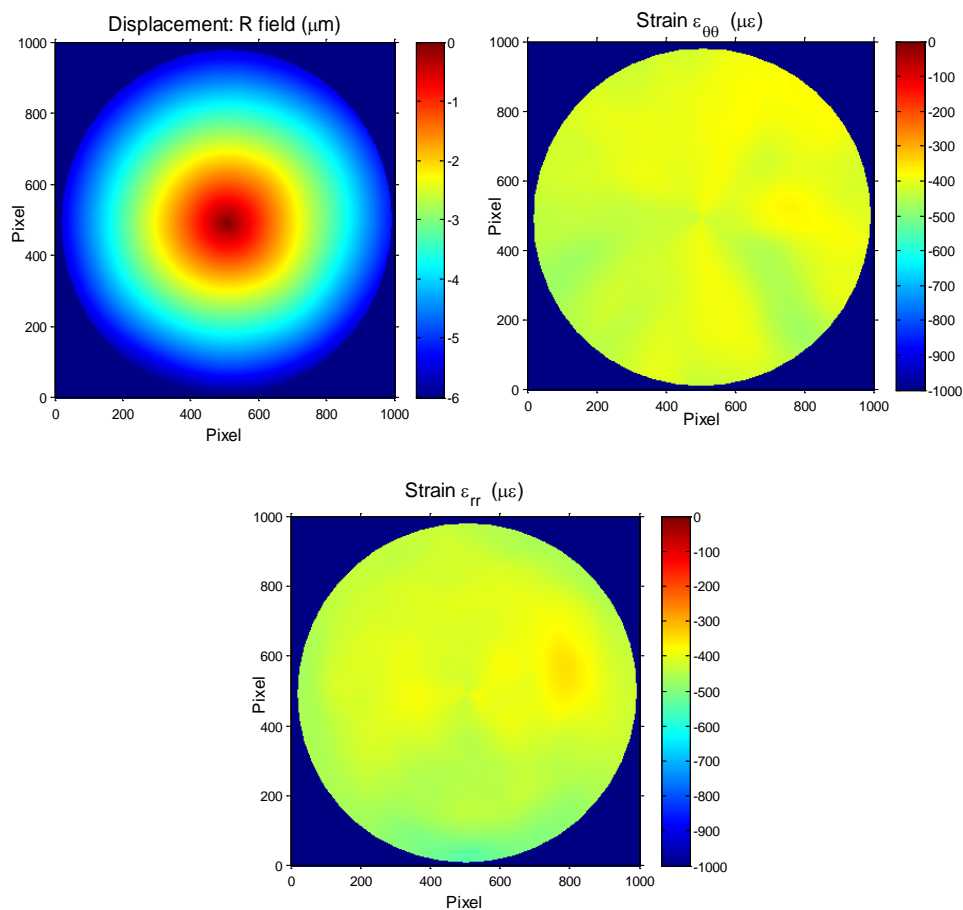


Figure 3-33. Day 6 displacement and strain analysis for the sealed cement paste specimen with $w/c=0.4$ in polar coordinate

3.4.4.2 Sealed mortar specimen

A modified sealing method is illustrated in Figure 3-33 and also described as following:

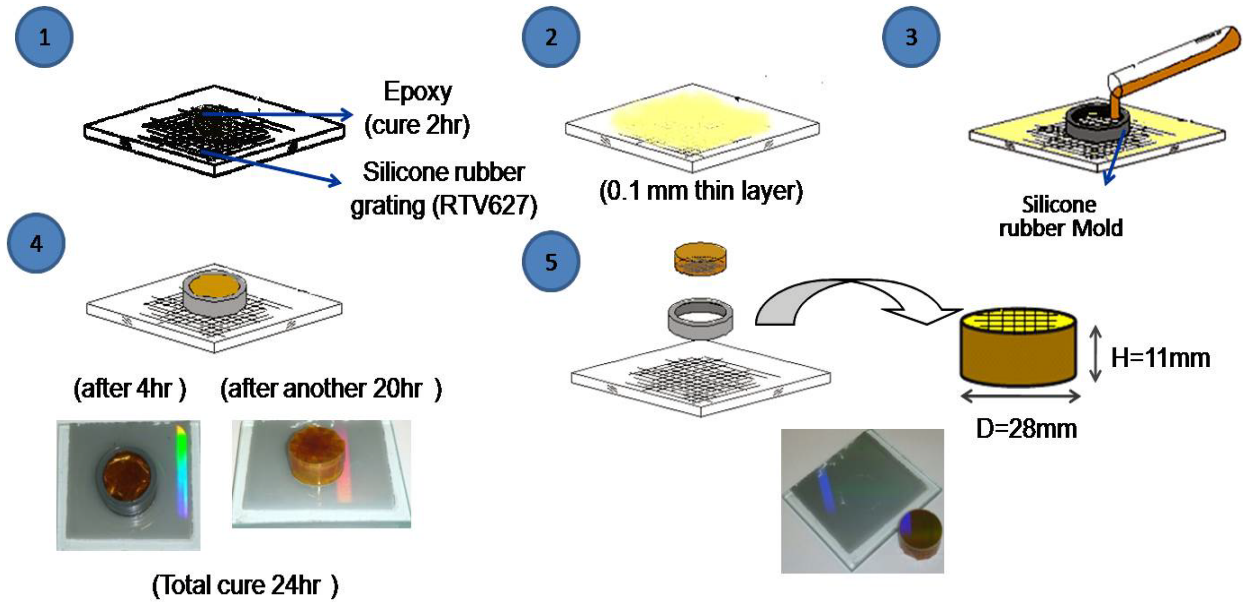


Figure 3-34. A modified sealing method

Step 4: 4 hours after concrete was poured into the mold, concrete was hardened a little bit. It is good time to seal the top side of the specimen with the tape. This prevents the moisture loss from that side afterwards. Another 18 hours later, the mold was removed and the side was sealed with the tape.

Step 5: The specimen was separated from the master grating. There is no need to seal the bottom side with the grating. The epoxy grating is already a block to the moisture diffusion. This method avoids repeating the sealing and unsealing steps for the measurement of everyday.

And the top side is sealed earlier to minimize the error from the moisture loss. Day 7 U-field moiré fringe pattern and the fringe pattern with rotation carriers for $w/c=0.3$ and $s/c=37.5\%$ in room temperature were shown as in Figure 3-34.

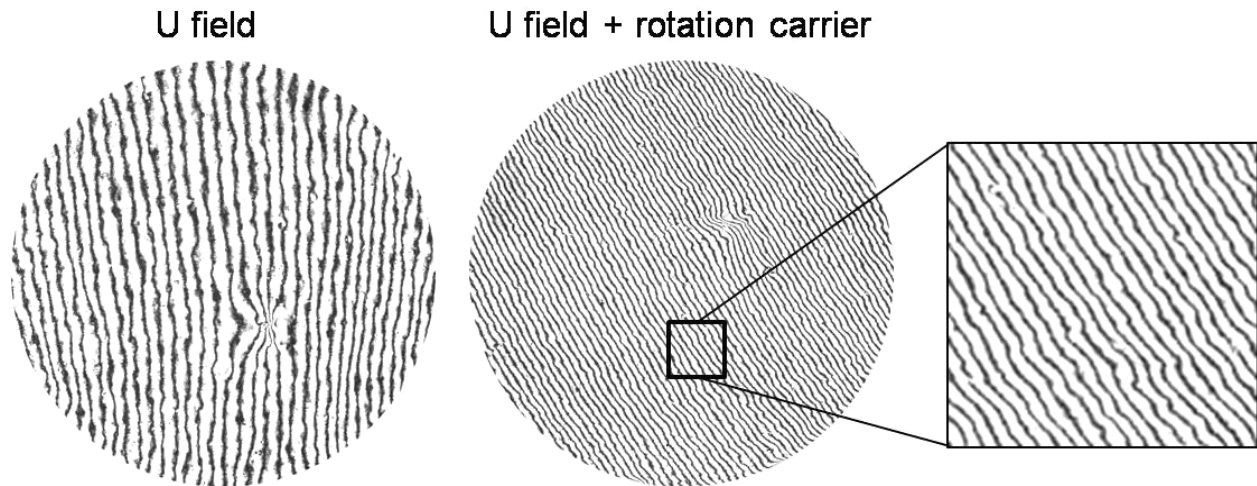


Figure 3-35. Day 7 Moiré fringe pattern for $w/c=0.3$ and $s/c =37.5\%$

It can be easily seen from the fringe pattern with rotation carriers that the fringes are close the uniformly-spaced distribution. Also, the fringes seem to be affected by the particles of the sand.

Figure 3-35 shows the evolution of the autogenous shrinkage. The autogenous shrinkage is reduced if comparing this result with that without sands. Therefore, aggregates can lower the chemical shrinkage.

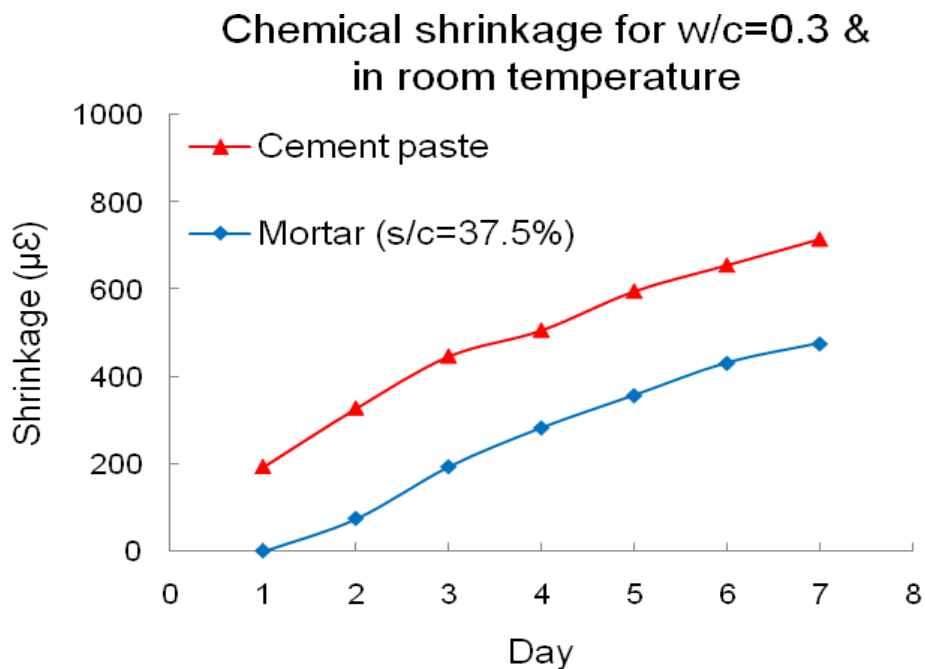


Figure 3-36. Autogenous shrinkage for mortar with $w/c=0.3$ and $s/c=37.5\%$ in room temperature

3.4.5 Ring Test for Crack Investigation

Since cracks could happen due to shrinkage and existence of constraints, the ring test as shown in figure 3-33 was performed to induce cracks on the concrete specimen. In the test, the thin epoxy layer was formed on silicone rubber grating, and then the steel rod was placed in the middle of the mold. The positions of the mold and the steel rod were marked on the back side of the silicon rubber grating in advanced. Cement paste fluid (w/c=0.5) was poured into the space formed by the mold and the steel rod. Likewise, the specimen with the steel rod was demolded after 24 hours. Then the chamber with drying condition of RH0% and room temperature was used to store the specimen. RH0% was chosen to induce large shrinkage to initiate cracks.

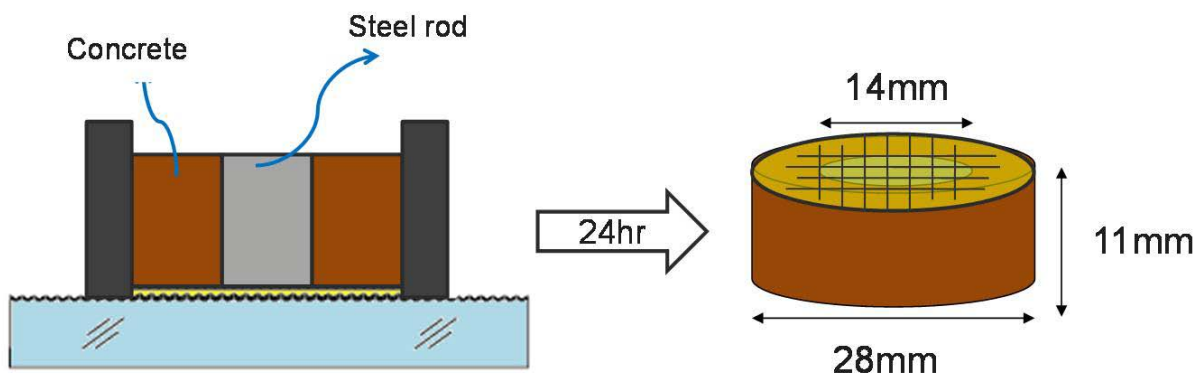


Figure 3-37. Scheme of Ring Test

The specimen was stored in the chamber for one day and then removed from the chamber for the measurement. Moiré fringe patterns on day 1 and day 2 were recorded as in figure 3-34. Day 1 moiré fringe patterns indicated the deformation was not significant because the specimen has not been stored in the chamber. Day 2 moiré fringe pattern has shown cracks occurred due to shrinkage and constraint from the steel rod as the insets in both U and V fields indicated. The pictures of the specimen in figure 3-35 demonstrated the crack from the top, bottom and side views. Cracks seemed to propagate along the radius direction.

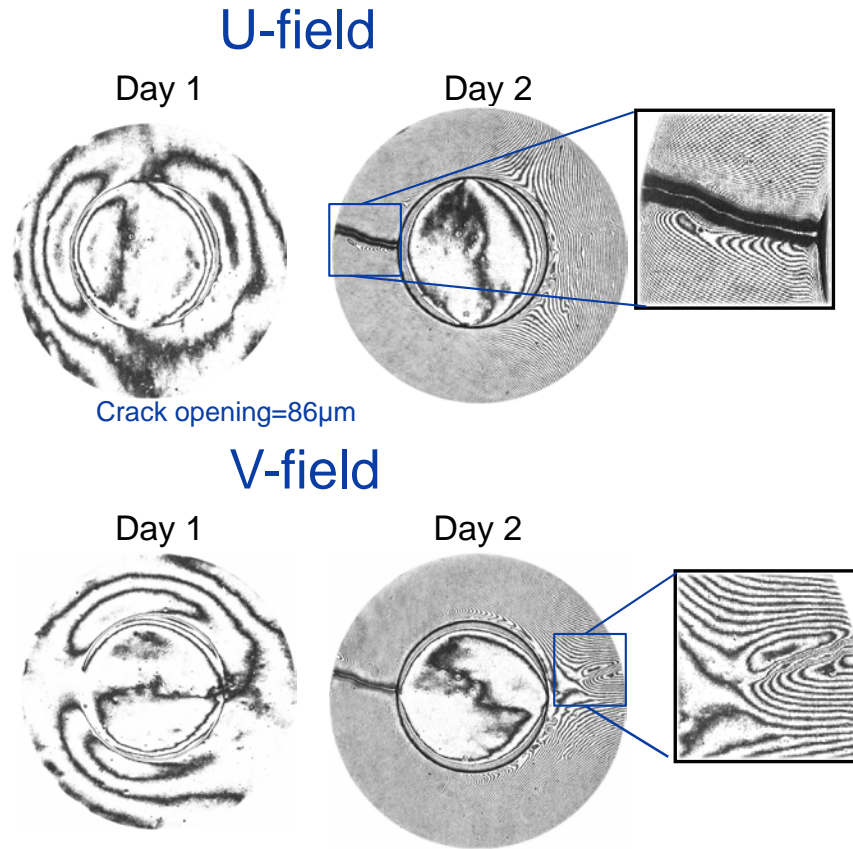


Figure 3-38. Ring Test investigation for RH=0% and room temperature

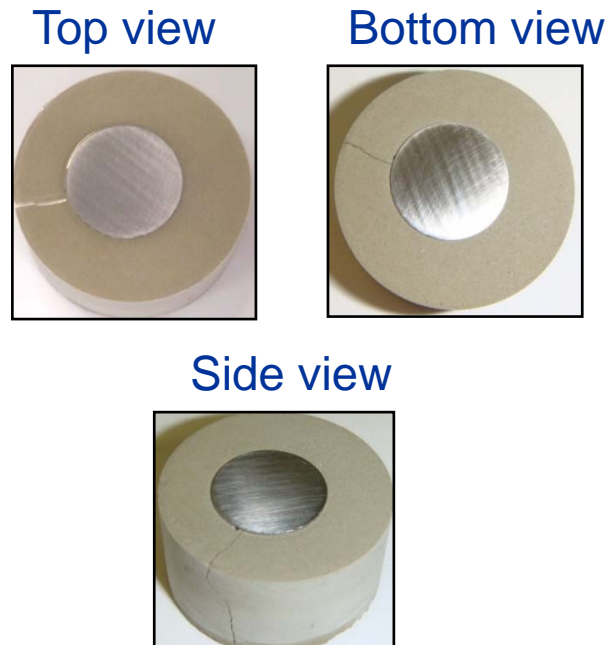


Figure 3-39. Pictures of the specimen with a crack in the ring test

3.4.6 Swelling test

Instead of being placed into the chamber under drying, the specimen was fully immersed into water for 24 hours after demold. But the grating was covered with dental material before immersion so that it was not allowed for direct contact with water. The fringe patterns before and after immersion as in figure 3-39 are compared. The result in figure 3-40 showed the specimen absorbed water and swelled. However, the deformation due to the absorption of water was insignificant.

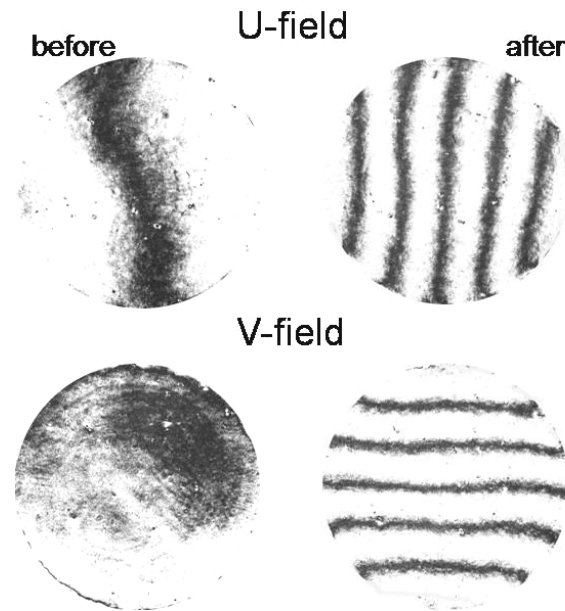


Figure 3-40. Moiré fringe patterns before and after one-day immersion

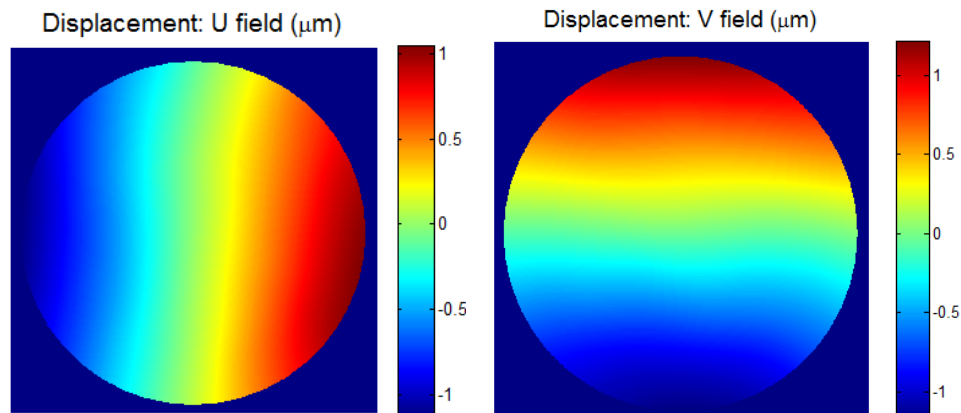


Figure 3-41. Full-field displacement maps for the swelling test

3.5 Conclusion & Discussion

The experimental technique to measure shrinkage which develops in concrete materials during drying is very repeatable and the process to prepare grating on the specimen is not complicated. The following conclusions can be drawn.

- The experimental technique to measure the shrinkage of concrete materials on a full-field basis was developed based on the methodology of curing reference method.
- A method of combining CRM and the sealing of the entire specimen was used to explore the relative contribution of non-drying shrinkage (chemical shrinkage) to the overall shrinkage in concrete materials.
- Phase shifting technique was used to analyze the moiré fringe patterns to obtain the full-field displacement and strain maps in both x-y and polar coordinates.
- The experimental results demonstrated the same trend of shrinkage behavior as documented in literature. The following conclusions can be drawn for shrinkage behavior in concrete,

For the cement paste specimens,

- Shrinkage increases with the decrease of relative humidity.
- Shrinkage decreases as temperature decreases.
- Shrinkage increases with time.
- Shrinkage near the exposed surface is larger than that in the inner core.
- For RH=100%, swell-up occurs near the outer surface, but shrinkage in the inner core.
- Specimens in small size have larger shrinkage (rate) than the ones in large size.
- Shrinkage increases as w/c ratio goes up.
- The specimen experiences the swelling after the immersion into water, but not significant.

For the specimens with fine or coarse aggregates,

- The rotation carriers are helpful in obtaining the average shrinkage and the full-field shrinkage information.
- Shrinkage increases with time.
- Shrinkage near the exposed surface is larger than that in the inner core.
- Shrinkage decreases as increasing fine aggregates
- Fine and coarse aggregates both affect the shrinkage locally.

For the sealed specimens,

- Chemical shrinkage increases with the decrease of w/c ratio.
- Chemical shrinkage above w/c=0.4 was not significant.
- Chemical shrinkage increases with the increase of temperature.
- Chemical shrinkage decrease with the increase of aggregate quantity.

For ring test, cracks occurred and propagated in the radial direction in the drying condition of RH0% and room temperature.

The experimentally obtained shrinkage measurements seem very useful in characterizing shrinkage behavior under different influencing factors. However, from the experiment, one cannot directly measure the shrinkage coefficient, which is a material property of cement paste. Material properties must be independent of specimen geometry, but dependent on the composition of cement paste, such as cement type and w/c ratio. The FEA model will be used to match the boundary conditions with the experiment to determine the shrinkage coefficient using an inverse approach.

CHAPTER 4 NUMERICAL MODELING

4.1 Introduction

According to literature, the shrinkage in concrete materials is not uniform over the entire specimen but highly dependent upon the distribution of moisture content. As known, moisture distribution is mainly governed by moisture diffusion during drying, which is here described by Fick's law and self-desiccation in the hydration process. Also, moisture distribution is generally described with relative humidity instead of moisture concentration. From the results of the experiments or previous research, shrinkage from self-desiccation or shrinkage under sealed conditions was negligible for $w/c=0.5$. In this case, the measured shrinkage could be assumed as drying shrinkage only. Therefore, only drying effect or moisture diffusion was considered in the model if $w/c=0.5$ was used. In other words, if w/c is below 0.4, shrinkage from self-desiccation must be considered.

The scheme of the inverse approach to obtain the material properties from the complex geometry in the tests is depicted in Figure 4-1. Finite element model as the forward model was created based on thermal mechanical interaction because this was a multi-physics problem. In this coupled model, moisture diffusion was modeled as heat transfer and shrinkage behavior was modeled as thermal expansion. Table 4-1 gave the details of the analogy regarding to the model. Two materials parameters, film coefficient and shrinkage coefficient, were defined and to be determined. Optimization in conjunction with the constructed finite element model was used to fit experimentally determined shrinkage in order to determine these two material parameters. This was the inverse method to solve this inverse problem. Once they are obtained, they can be the inputs for finite element analysis to predict the shrinkage under different drying or geometric conditions. The other tests can be performed and their results can be compared with FEA.

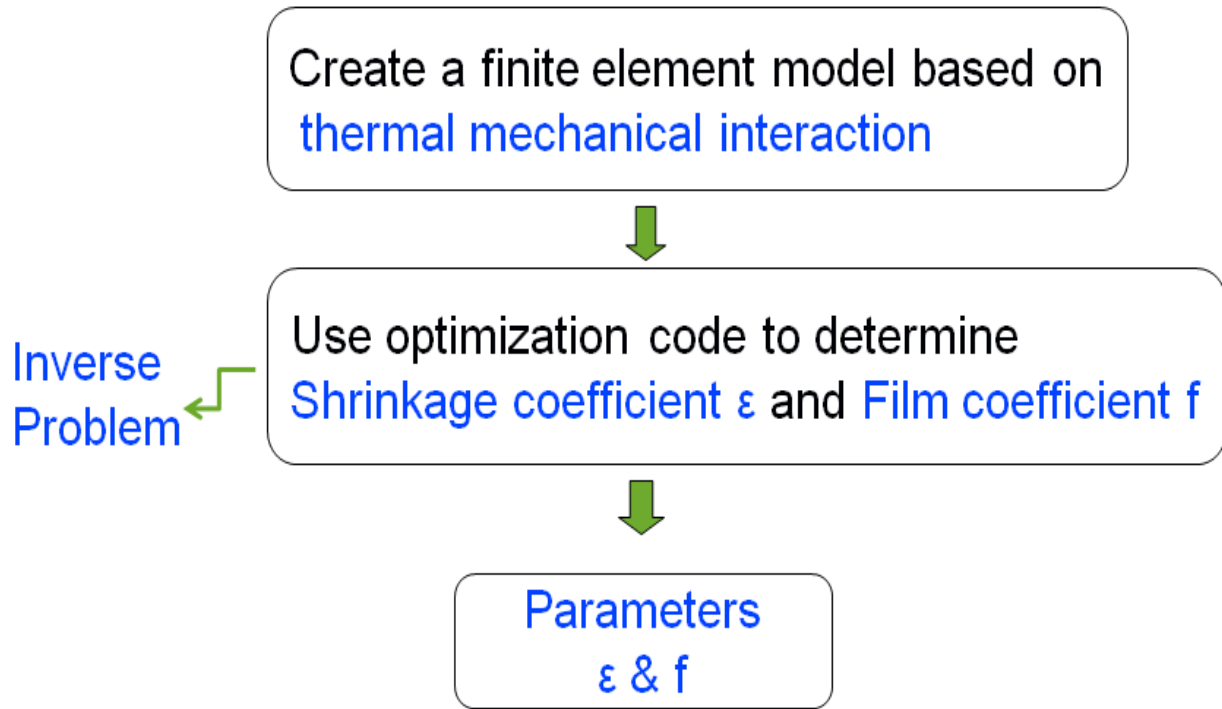


Figure 4-1. Scheme of numerical modeling

Table 4-1. Thermal mechanical interaction model

Thermal Model		Mechanical Model	
Heat Transfer	vs.	Moisture Diffusion	Thermal Expansion vs. Shrinkage
Temperature	vs.	Relative Humidity	Thermal Expansion coefficient vs. Shrinkage coefficient
Conductivity	vs.	Diffusivity	
Surface coefficient	vs.	Film coefficient	

4.2 Model Description

4.2.1 Axisymmetric Model

In order to obtain the defined material properties, the finite element model was created and took advantage of axisymmetry because the geometry of the specimen in the tests was in the shape of the cylindrical disk. The use of the axisymmetric model could save running time in each iteration while using the inverse method to determine material properties. Eight-node quadratic quadrilateral meshes were used in the model.

4.2.2 Materials Properties

According to literature, the expression of moisture diffusion coefficient shown as below was used in the thermal model:

$$D = D_1 * \left(\alpha + \frac{1 - \alpha}{1 + \left(\frac{1 - h}{1 - h_c} \right)^n} \right) \quad (4-1)$$

Where D_1 is the maximum of $D(h)$ for $h = 1.0$, $\alpha = D_0/D_1$, D_0 is the minimum of $D(h)$ for $h = 0.0$, h_c is the pore relative humidity when $D(h) = 0.5D_1$. Here $D_1 = 25 \text{mm}^2/\text{day}$, $\alpha = 0.1$, $n = 6$, and $h_c = 0.72$ are approximately assumed [105]. The values of these parameters are only applicable to ASTM Portland cement type I with $w/c = 0.5$ in room temperature condition. Typical values $E = 2.5 \text{GPa}$ and $\nu = 0.3$ were used for cementitious materials in the mechanical model. The shrinkage coefficient in the mechanical model and film coefficient in the thermal model are two unknown material properties to be determined by the inverse approach.

4.2.3 Initial Condition:

Moisture diffusion from the bottom side, which is the opposite side to the top side with the grating, to the environment started before the specimen was demolded. However, it was assumed negligible due to the long process of drying in the tests. Also, the specimen took some

time to cure and get hardened from the fluid phase. Therefore, it was assumed that the whole specimen has $h=1$ or 100% when $t=0$ which referred to Day 1.

4.2.4 Boundary Condition

The boundary conditions in moisture diffusion model were described in figure 4-2. The grating on top of the specimen was assumed as the insulation to moisture flux. The insulation on the boundary along the symmetrical line was automatically assumed. The flux on other two boundaries was assumed as convection type which is described by the equation in figure 4-2. Here, f represents film coefficient. J represents moisture flux. h_s represent relative humidity on the surface. h_{en} represents ambient relative humidity. No boundary conditions need to be defined in the mechanical model because the specimen in the experiments was in the condition of free shrinkage.

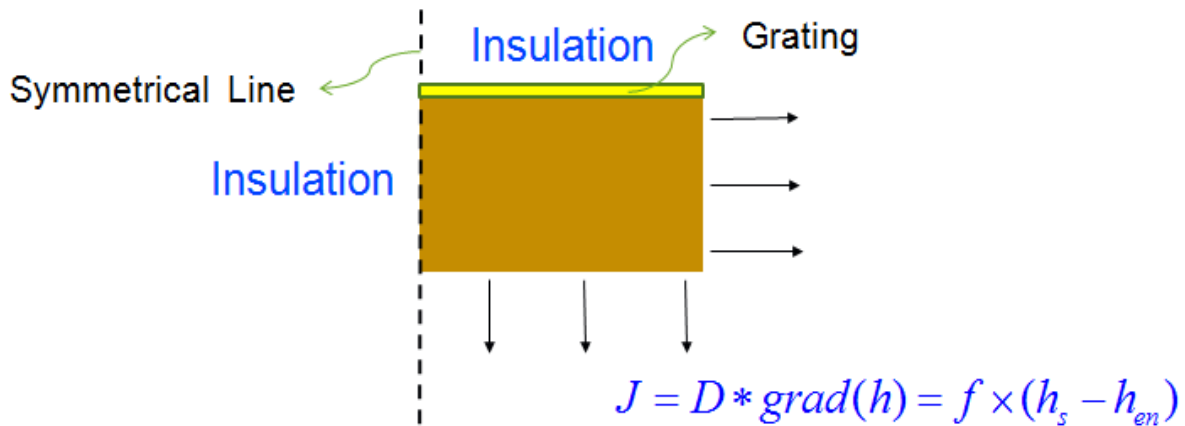


Figure 4-2. Boundary conditions of moisture diffusion model

4.3 Inverse Method

In the inverse method, the finite element model described above was the forward model created in COMSOL. This forward model was interfaced with the optimization code which was developed in Matlab to obtain the shrinkage coefficient and film coefficient. The shrinkage coefficient and the film coefficient were two variables in the optimization code. In each of

iterations, the optimization code specified the values of these two variables, called the forward model to solve the problem, and then computed the value of the objective function. When the value of the objective function was minimized, which indicated the fitting of the FEA result with the experimental data was optimized, the shrinkage coefficient and the film coefficient were hence determined. The optimization code was based upon the nonlinear least-squares method and the Gauss-Newton algorithm was adopted. The objective function was defined as the following equation:

$$F(\varepsilon, f) = \sum_{j=1}^m \sum_{i=1}^n (e_{ij} - \bar{e}_{ij})^2 \quad (4-2)$$

In the above formulation, there are two unknown coefficients represented by constant ε as the shrinkage coefficient and represented by constant f as the film coefficient. e_{ij} in equation (4-2) is the i th radial strain on j th drying day obtained experimentally and \bar{e}_{ij} is the radial at the same point computed using finite element analysis. It is assumed that there are n such experimentally obtained radial strains at n positions from the center to the circumference on the surface with the grating. Here, n is equal to 6 and the measurement positions are equally spaced. Hence, the distance between two neighboring positions is 2.8mm. And m represents the total drying duration in the chamber in units of day. Here, m is equal to 6, which corresponds to drying duration of 6 days in the experiments.

Using the experimentally obtained radial strains under RH=50% and room temperature at six locations from Day 2 to Day 7, the estimation of these two material parameters was performed through the inverse approach mentioned above. The curve fitting result was shown in Figure 4-3. The shrinkage coefficient $\varepsilon=53.8 \mu\varepsilon / ^\circ\text{C}$ and the film coefficient $f= 2.12 \text{ mm/day}$ were obtained.

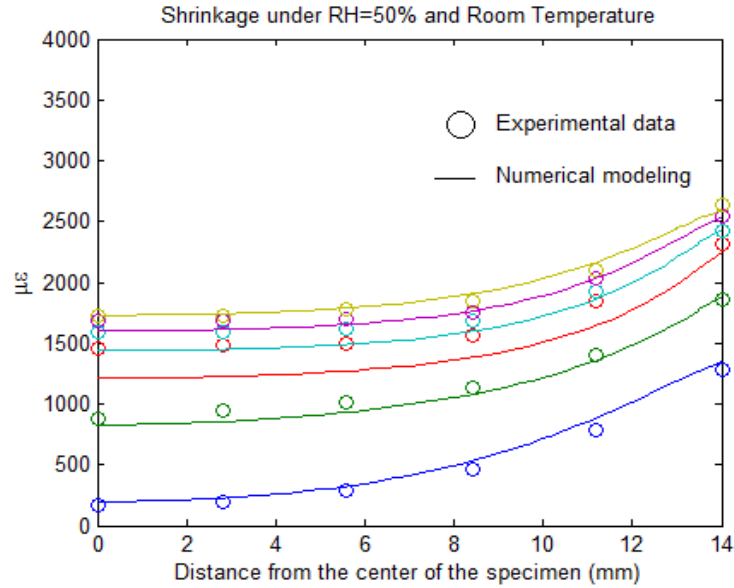


Figure 4-3. Optimization results

The errors of the optimization were calculated and shown in table 4-2. The goodness of fit can be evaluated by the value of R square value. The value indicated the fitting between the experimentally obtained data and FEA results is good. The discrepancy mainly results from the day 4 data.

Table 4-2. Errors of optimization

Mean	TSS	SSR	SSE	E_{rms}	R^2
1515.995	13159522.14	13005106.88	154415.26	4289.31	0.9883

Once the shrinkage coefficient and the film coefficient were determined, 3-D model was created to model shrinkage behavior of the entire specimen in x-y coordinate as figure 4-4. This made it easy to compare between FEA results and experimental results from moiré interferometry in x-y coordinate.

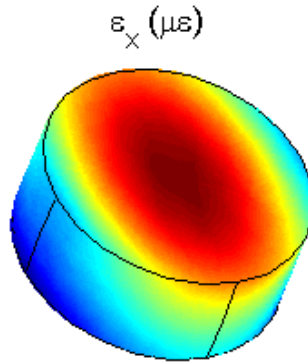


Figure 4-4. 3-D model of shrinkage behavior

The top surface of 3-D model which the grating was on was selected and the shrinkage maps on this surface were drawn as figure 4-5. The full-field strain information in both x-y and polar coordinates is shown. The shear strain in polar coordinate is automatically assumed zero in the finite element analysis.

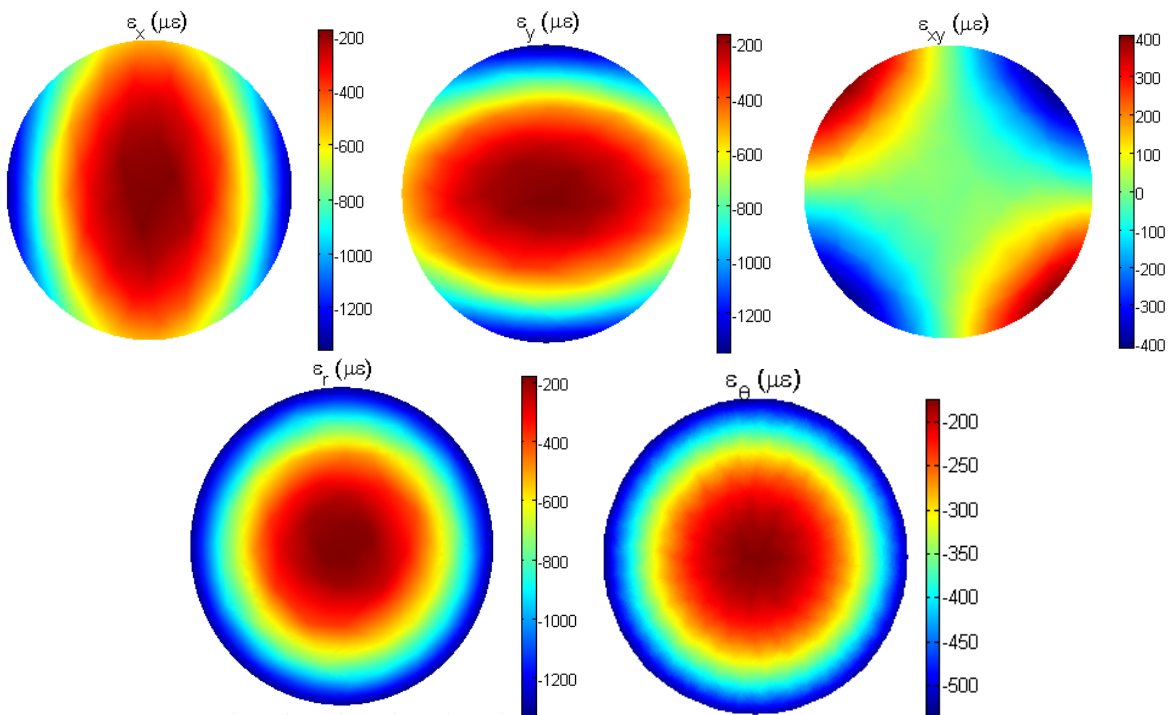


Figure 4-5. FEA results for RH=50% and room temperature

4.4 Validation of Model

In order to validate the constructed model and the obtained material properties, some other tests were performed and their results were compared with FEA. Different surrounding relative humidity, different size and shape of the specimen, ring test, shrinkage before demold and reinforced cement paste were tested and discussed.

4.4.1 Different Surrounding Humidity

The same material parameters were used to predict the shrinkage under the drying condition of RH=80% and room temperature. The size of the specimen and w/c ratio remained the same. The moiré fringe patterns for RH80% and room temperature are covered in Appendix. The experimental and FEA results are shown as Figure 4-6. For each day measurement, the experimental result did not match perfectly with FEA result. However, they are very similar in the trend and the range of the magnitude. The full-filled experimental and FEA maps on Day 3 are compared as Figure 4-7. The maps indicated that the results from the experiment and FEA have very good agreement.

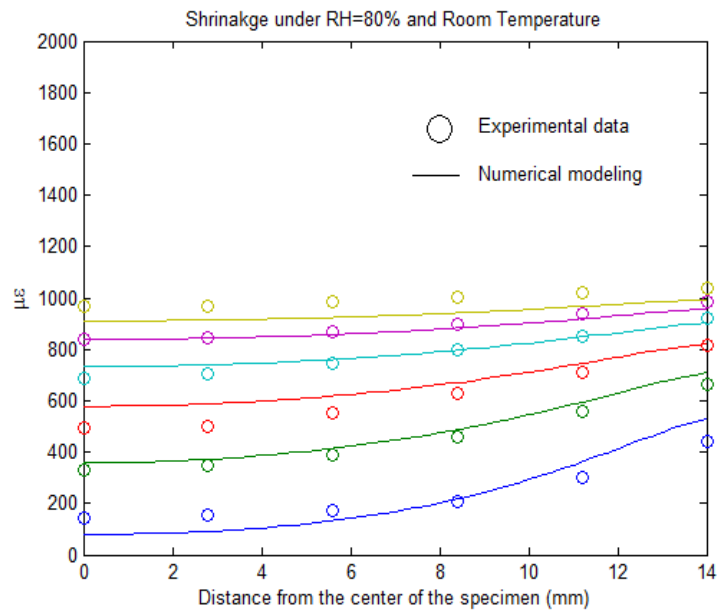


Figure 4-6. Experimental and FEA results for RH=80% and room temperature

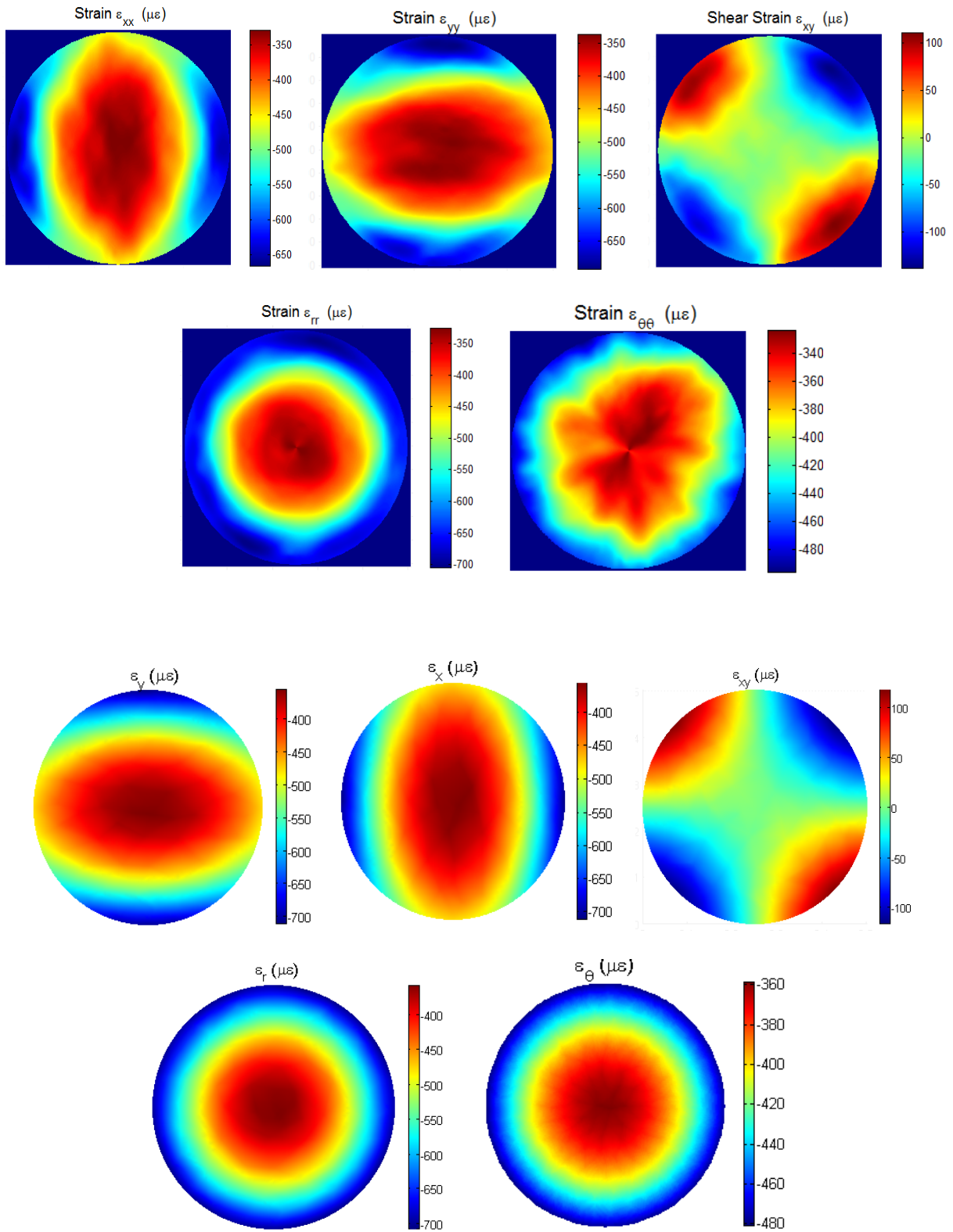


Figure 4-7. Experimental and FEA results for RH=80% and room temperature on Day 3

The experimental technique can only measure the deformation on the surface of the specimen. In order to investigate the true shrinkage behavior inside of the concrete specimen, the cross-section views of the deformations in cylindrical coordinate in FEA are used to address the 3-D effect through the thickness as Figure 4-8. The top and left sides represent the surface with the grating and the central axis of the specimen individually. The shear components are not shown here due to their insignificance in magnitude. The normal components reveal the maximum shrinkage occurs in the area near the bottom side and close to the outer surface. On the other hand, the minimum shrinkage occurs near the central axis of the specimen and close to the surface with the grating.

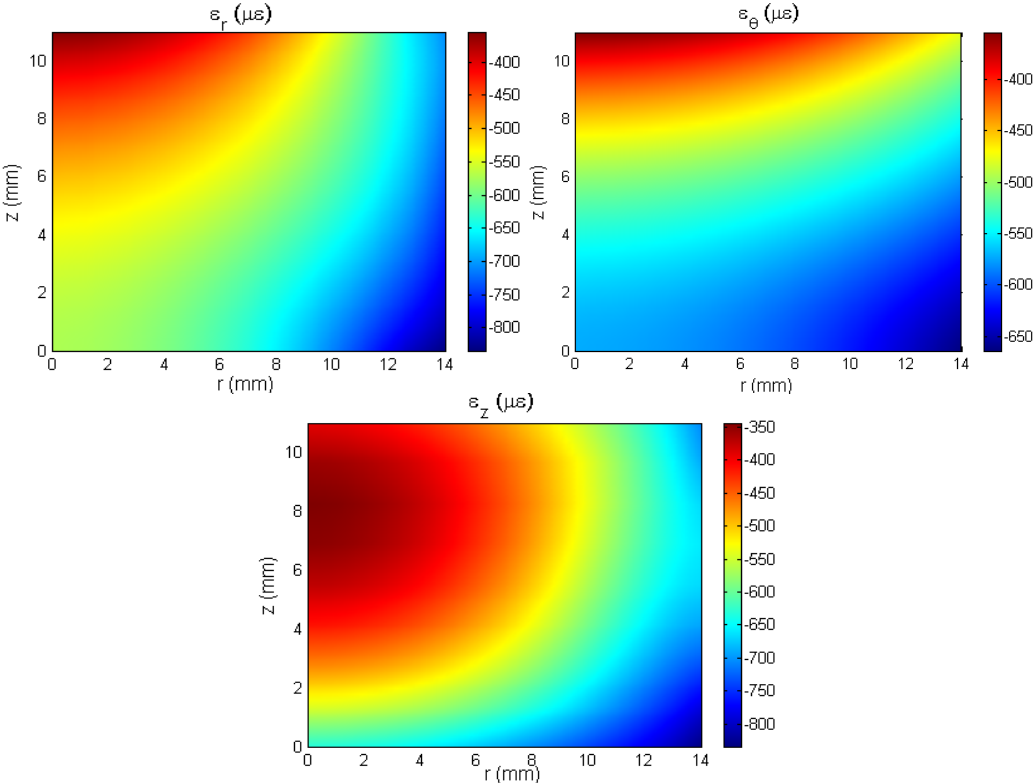


Figure 4-8. Cross-section view of deformations for RH=80% and room temperature on Day 3

4.4.2 Ring Test

Ring test was performed again, but this time the test was under room temperature and RH60% which was achieved in the laboratory. The U and V-field moiré fringe patterns from Day 1 to Day 3 were recorded as figure 4-9. Apparently, the deformation of the steel rod was insignificant according to the fringe patterns on the surface of the steel rod. Also, no cracks are observed from the fringe patterns because the shrinkage-induced stress is not high enough to initiate cracks.

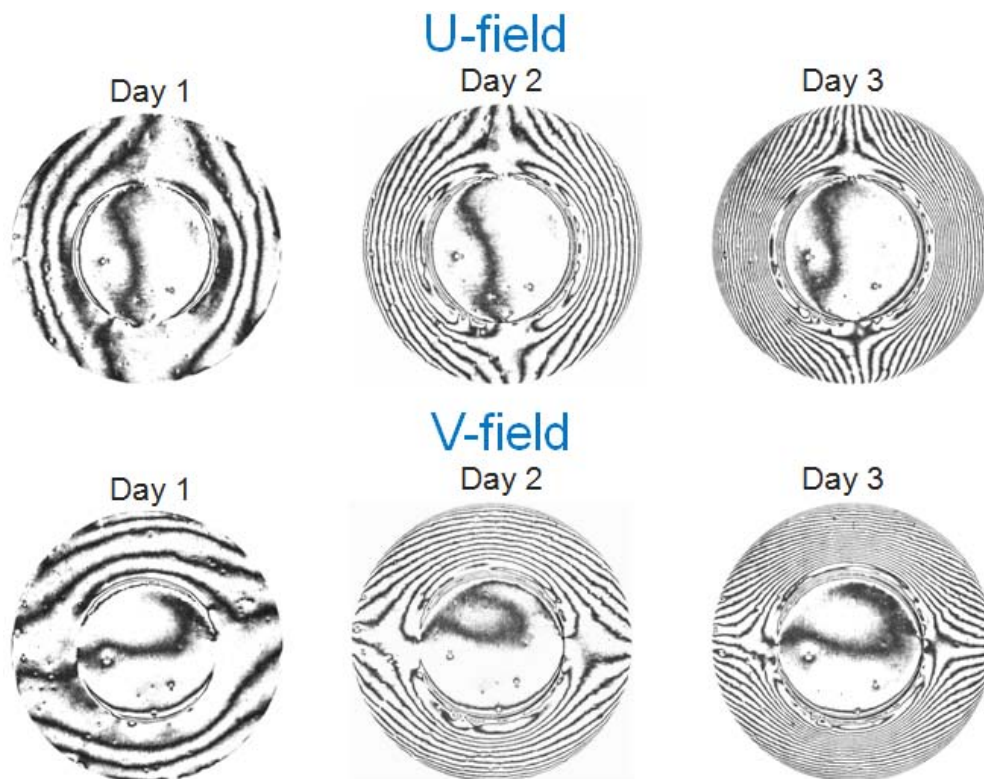


Figure 4-9. U&V-field moiré fringe patterns for ring test under RH60% and room temperature

The Day 2 and Day 3 moiré fringe patterns were analyzed through the automatic fringe analysis system and the full-field maps in x-y coordinates were shown as figure 4-10 for Day 2 and figure 4-12 for Day 3. A 3-D composite model with steel rod and cement paste was created in finite element analysis with the typical values $E=200$ GPa and $\nu=0.33$ for the steel rod in the test. FEA results were also included in the figures for the purpose of comparisons.

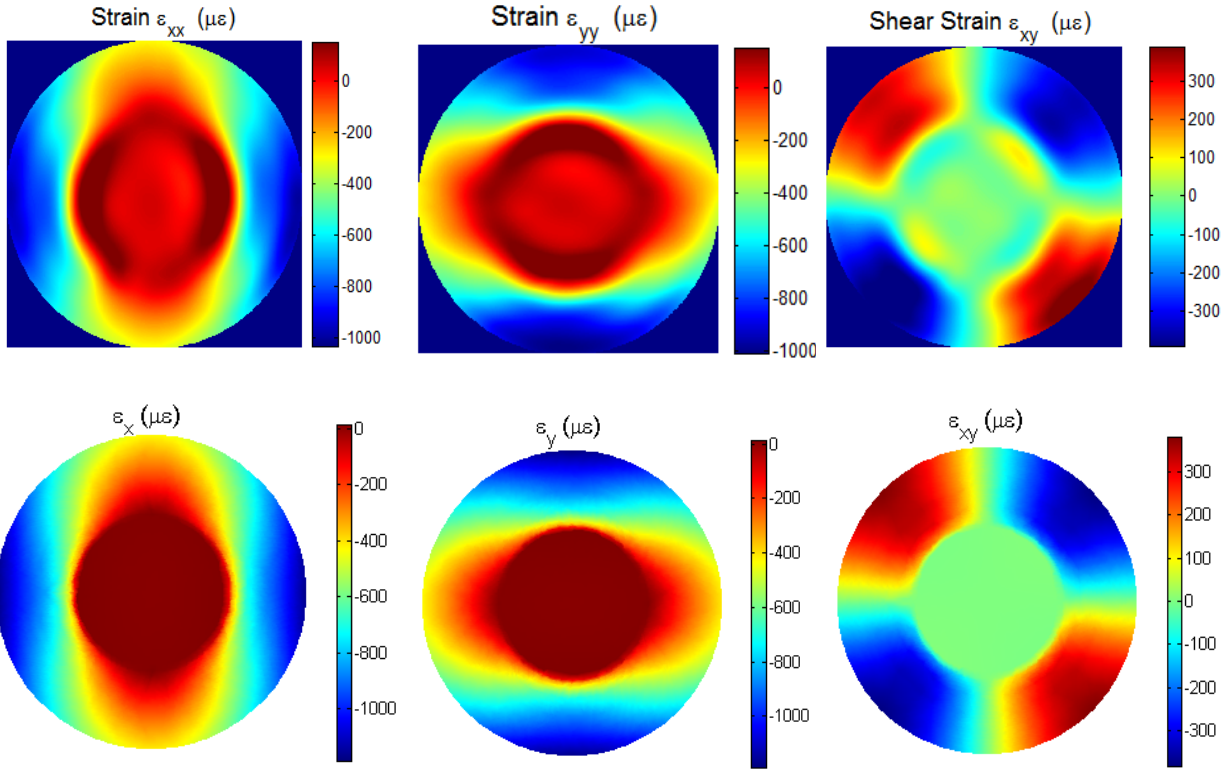


Figure 4-10. Experimental (above) and FEA (below) results of ring test on Day 2

From figure 4-10 or 4-11, the experimental result and FEA result matched well except in the magnitude around the interface between the steel rod and the cement paste. The shrinkage distribution along the horizontal centerline in the ϵ_{xx} map was plotted as figure 4-13. Clearly, there is larger discrepancy in magnitude around the interface.

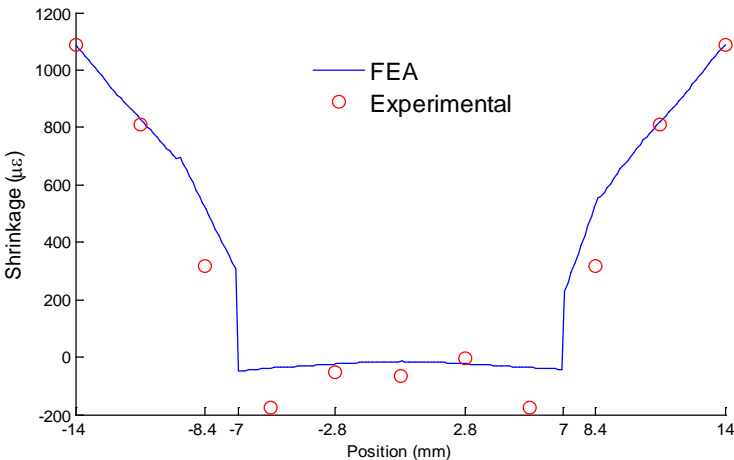


Figure 4-11. Experimental and FEA shrinkage distribution for Day 2

From figure 4-12, it can be seen that the maximum normal and shear strains moved toward the steel rod instead of remaining near the outer surface. The experimental result had good agreement with the result from FEA.

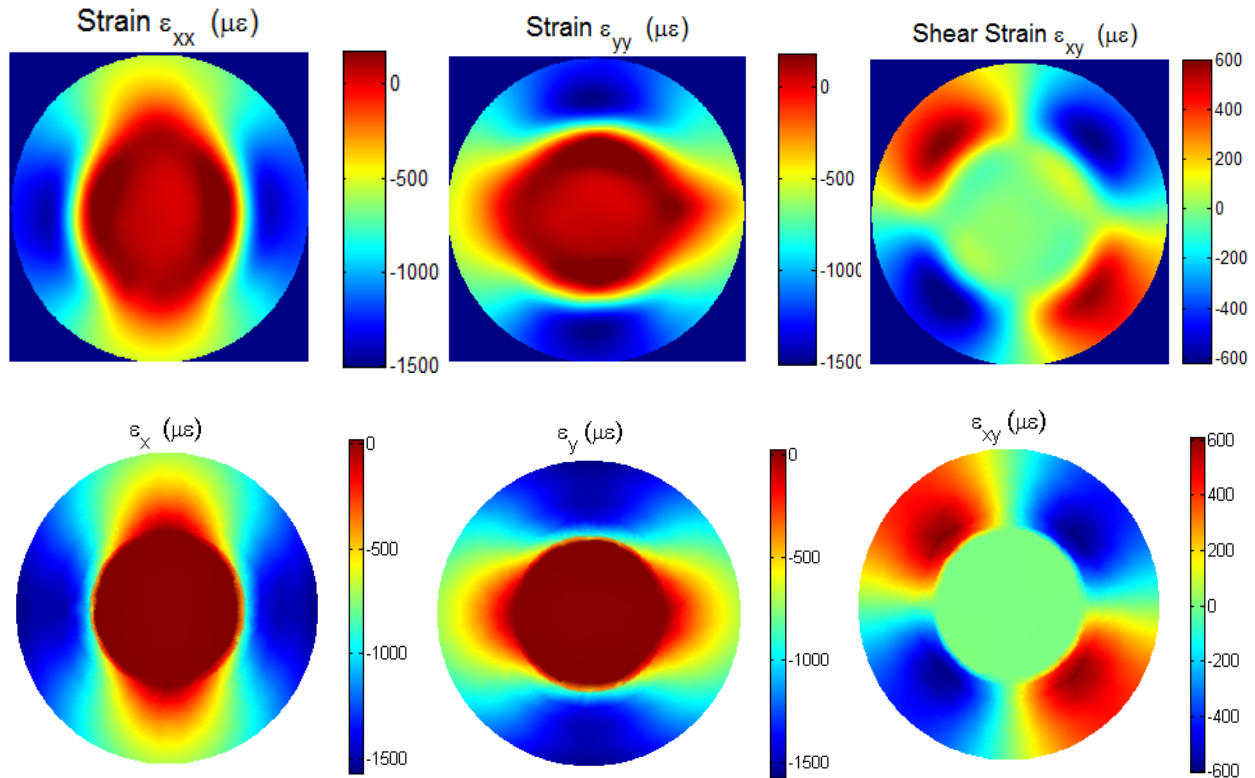


Figure 4-12. Experimental (above) and FEA (below) results of ring test on Day 3

The experimental and FEA full-field strain information on the cement paste only (the information on the steel ring not included) are shown as figure A-8 for Day 2 and figure A-9 for Day3 in Appendix.

4.4.3 Square Shape

The square-shape cement paste specimen with w/c=0.5 was made with the size of 25 mm in length and 14 mm in thickness. The same process was used to prepare grating on the surface the specimen. The specimen was stored in the chamber of 80% RH and room temperature for three day3 after demold. The U and V-field moiré fringe patterns from Day 1 to Day 4 were recorded as figure 4-13. The distribution of the normal strain in x-direction along the red line

which was indicated in figure 4-13 was plotted as shown in figure 4-14. The full-field experimental and FEA maps for Day 4 were shown as figure 4-15. However, the displacement and normal strain in y direction are not shown here due to symmetry.

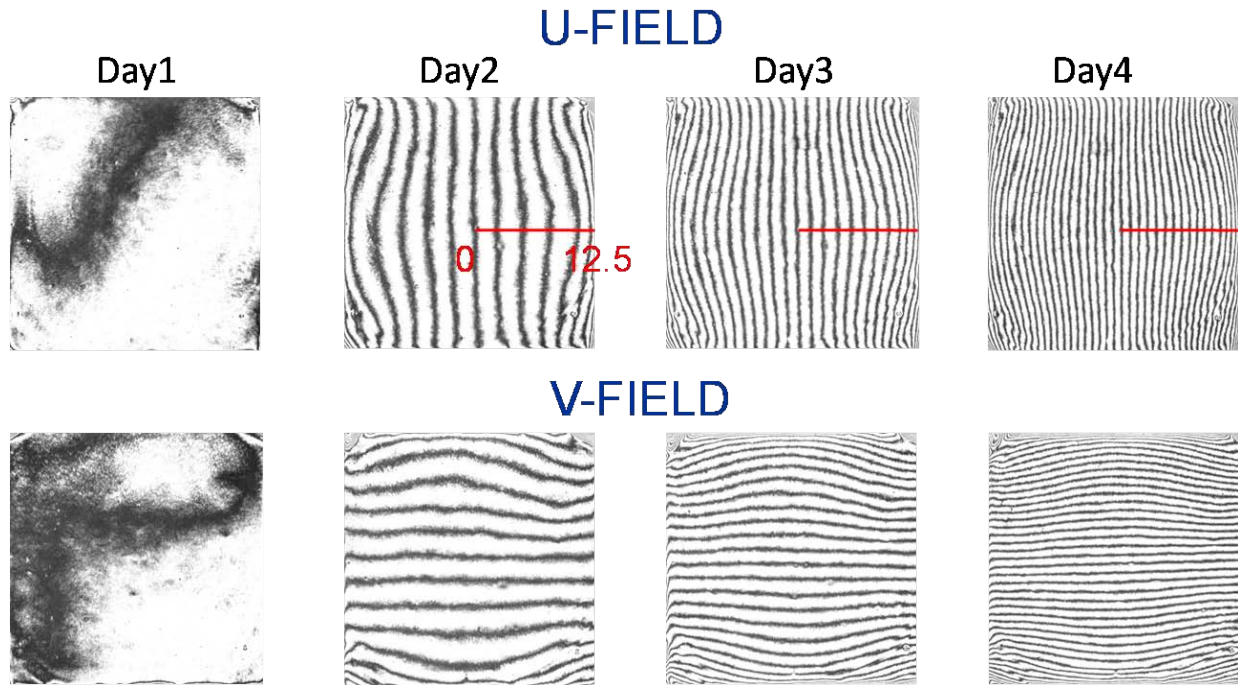


Figure 4-13. U and V-field moiré fringe patterns for the square specimen

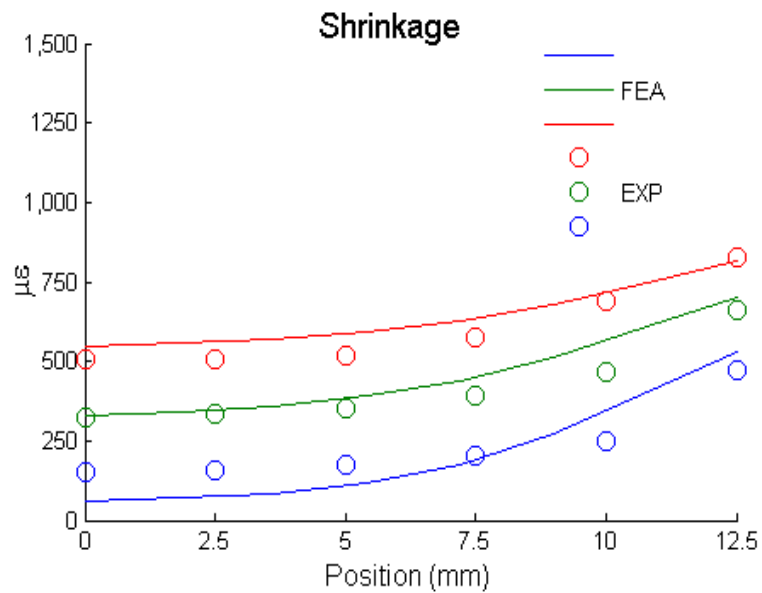


Figure 4-14. Distribution of normal strain in x-direction along the red line

From figure 4-14, the experimental result did not match well with FEA result for every day measurements. However, they are similar in the range of the magnitude and the trend. Figure 4-15 shows the maximum in-plane normal strain occurred in the four corners of the specimen. The maximum shear strain did not occur exactly in the corners but near the corners. FEA and the experimental results had good agreement in the displacement field.

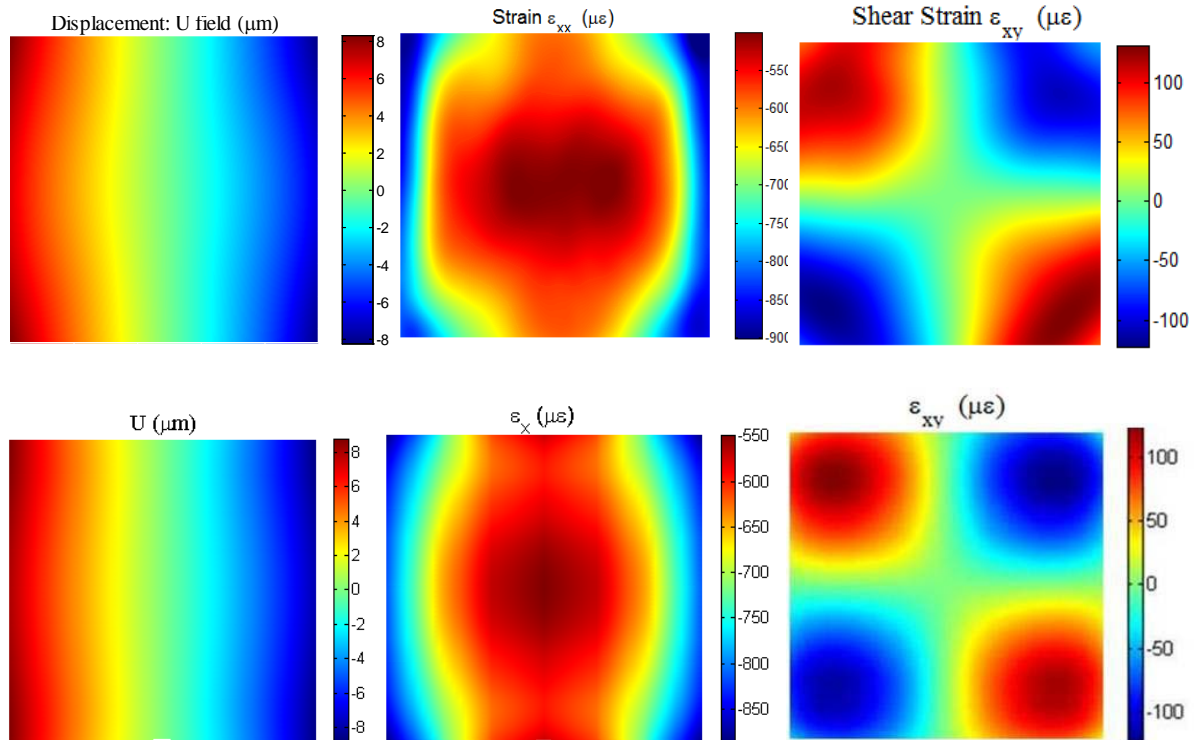


Figure 4-15. Experimental (above) and FEA (below) maps for square specimen on Day 4

4.4.4 Expansion on Day 1

4.4.4.1 In-plane deformation measurement

Instead of the measurement of shrinkage on Day 1, the measurement of expansion was obtained using CRM. In order to account for this phenomenon, FEA was performed and the boundary condition for drying effect was modified. The top surface was the surface with the diffraction grating where the moisture flux was blocked by the master grating. The side surface of the specimen was covered with the silicone rubber mold. Hence, the moisture fluxes only

diffused from the bottom surface of the specimen within day 1. 12 hour was assumed as drying duration. FEA result was compared with the result from the experiment of RH=50% and room temperature as figure 4-16.

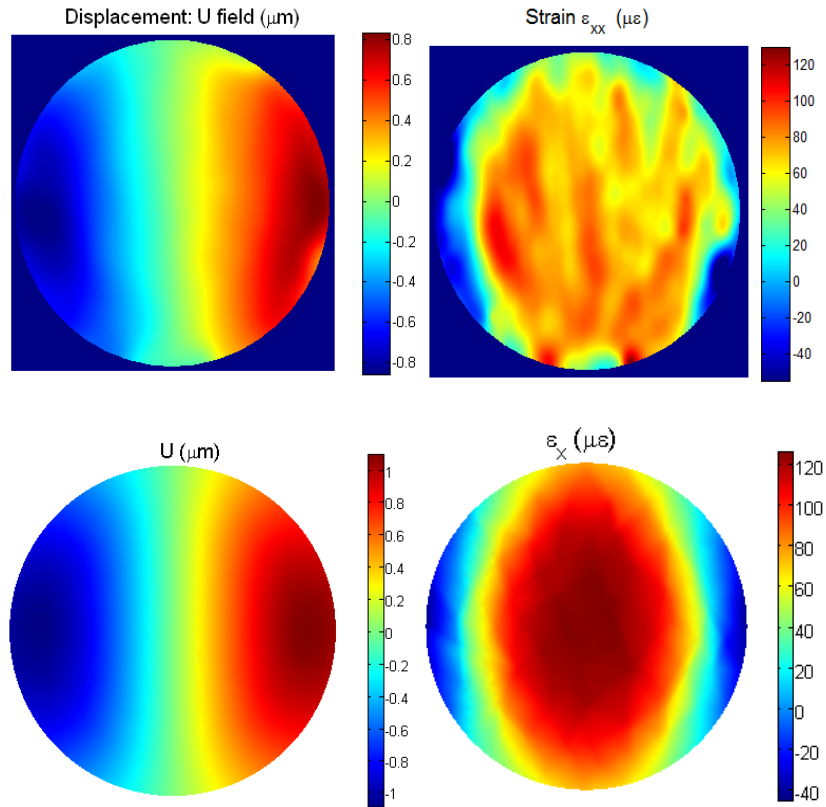


Figure 4-16. Experimental (above) and FEA (below) results for Day 1 measurement

The results show the U-field displacement map from the experiment has good agreement with that from FEA. The experimental U-field strain map was not smooth due to the difficulty in analyzing the fringe pattern with few fringes. However, it still indicates shrinkage occurred near the outer surface and expansion in the middle as FEA shows. Overall, it can be seen from the displacement map that the top surface of the specimen experienced the expansion once it was demolded. The explanation is that the bottom surface experience larger shrinkage than the top surface due to the fact that the drying started from the bottom surface. The differential shrinkage

through the thickness should cause the bending to the specimen. The top surface should experience some tension and the bottom surface compression.

4.4.4.2 Out-of-plane displacement simulation

In order to further prove the measurement of expansion on day 1 or bending effect, out-of-plane displacement was simulated by FEA as in figure 4-17. In the model, the top surface faced the positive z-direction. The map clearly shows the top surface has the convex shape. This was caused due to the bending of the specimen.

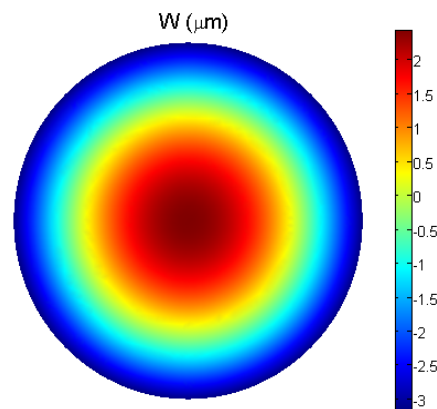


Figure 4-17. FEA result for out-of-plane displacement

4.4.5 Reinforced Concrete

Previously, the gravels were embedded into the cement paste in the gravel test. The result reflected the effect of gravels on the fringe densities at the positions of gravels. However, it is difficult to model the test with FEA not only because of the irregular shape and size of the gravels but also because of the unknown exact positions of the gravels. The cement paste specimen was reinforced with the four steel rods. The arrangement and the size of the rods are shown in figure 4-18. The positions of the steel rods in the mold are printed on the paper sheet. The sheet was attached on the back side of the master grating as shown in figure 4-20. Therefore, the rods and the mold could be located at the specific positions.

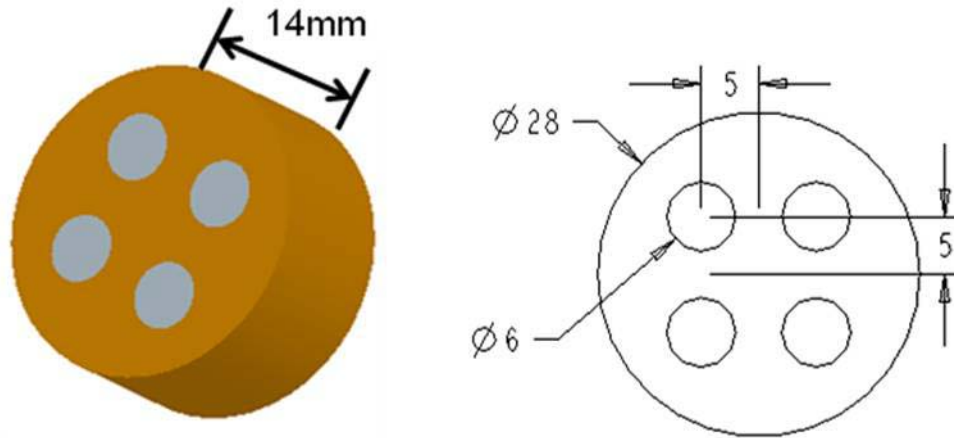


Figure 4-18. Size and arrangement of the steel rods in cement paste

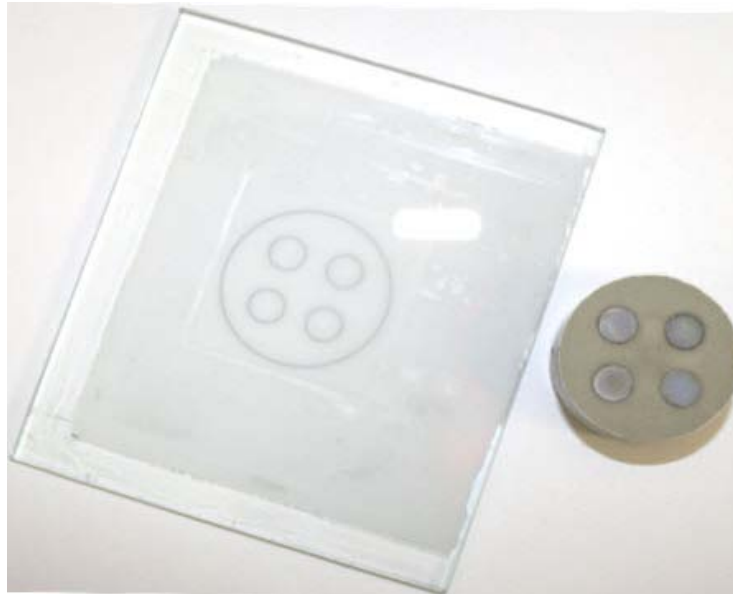


Figure 4-19. Master grating with the sheet on the back

The specimen was first stored in the drying conditions of RH80% and room temperature for one day. Then it was stored under RH60% and room temperature for another day. The moiré fringe patterns from Day 1 to Day 3 are shown in figure 4-20. The Day 2 and Day 3 moiré fringe patterns were analyzed through the automatic fringe analysis system and the full-field strain maps in x-y coordinates were shown as figure 4-22 for Day 2 and figure 4-23 for Day 3. A 3-D composite model with 4 steel rods and cement paste was created in finite element analysis with

the typical values $E=200$ GPa and $\nu=0.33$ for the steel rod in the test. FEA results are also included in the figures for the purpose of comparisons. However, the full-field maps do not show information concerning the steel rods not only because they are not the focus in the research but also because their deformation is insignificant compared with the portion of the cement paste according to the fringe patterns.

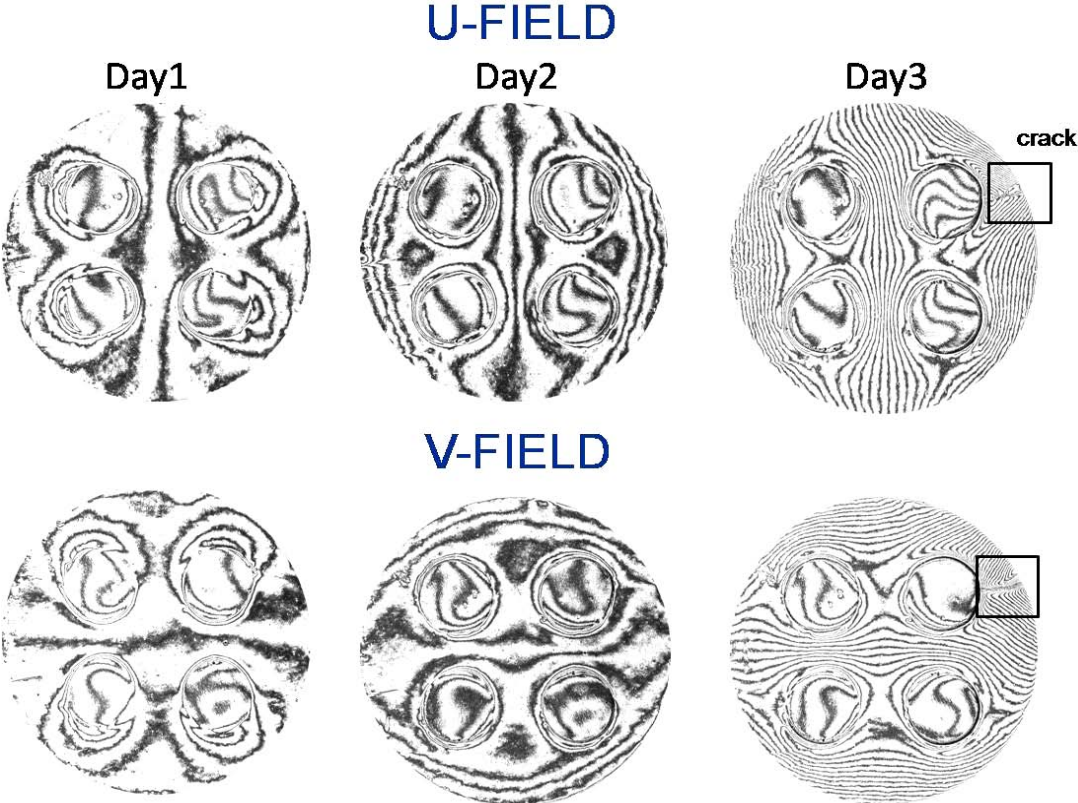


Figure 4-20. Moiré fringe patterns for reinforced concrete

The displacement fields in both x-y and polar coordinates and the strain fields in polar coordinate for Day 2 are not shown here but included in Appendix. From figure 4-21, the trend in the experimental result is similar to that in FEA. From figure 4-22, it can be seen that the experimental result and FEA result also matched well except in the area around the crack.

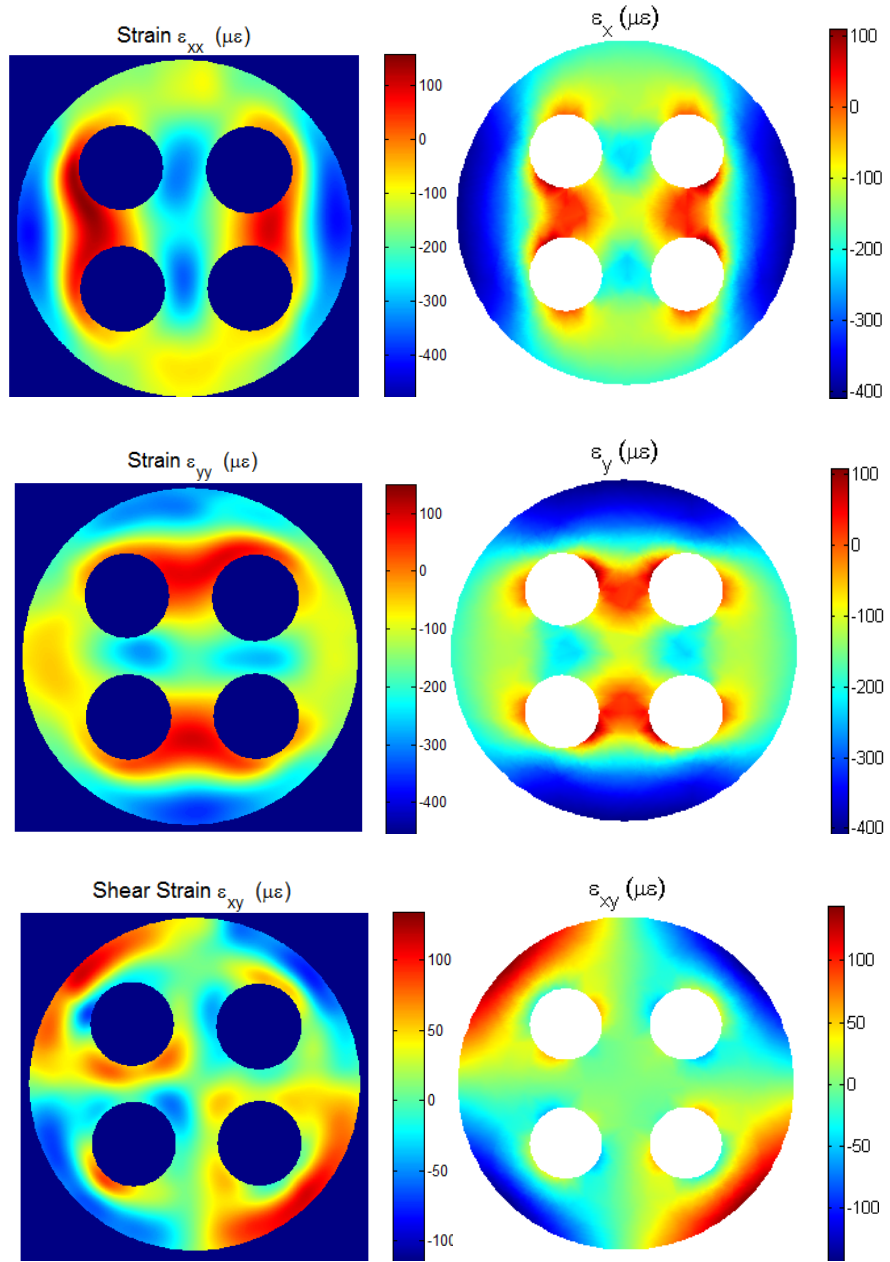


Figure 4-21. Experimental (left) and FEA (right) results for reinforced concrete on Day 2

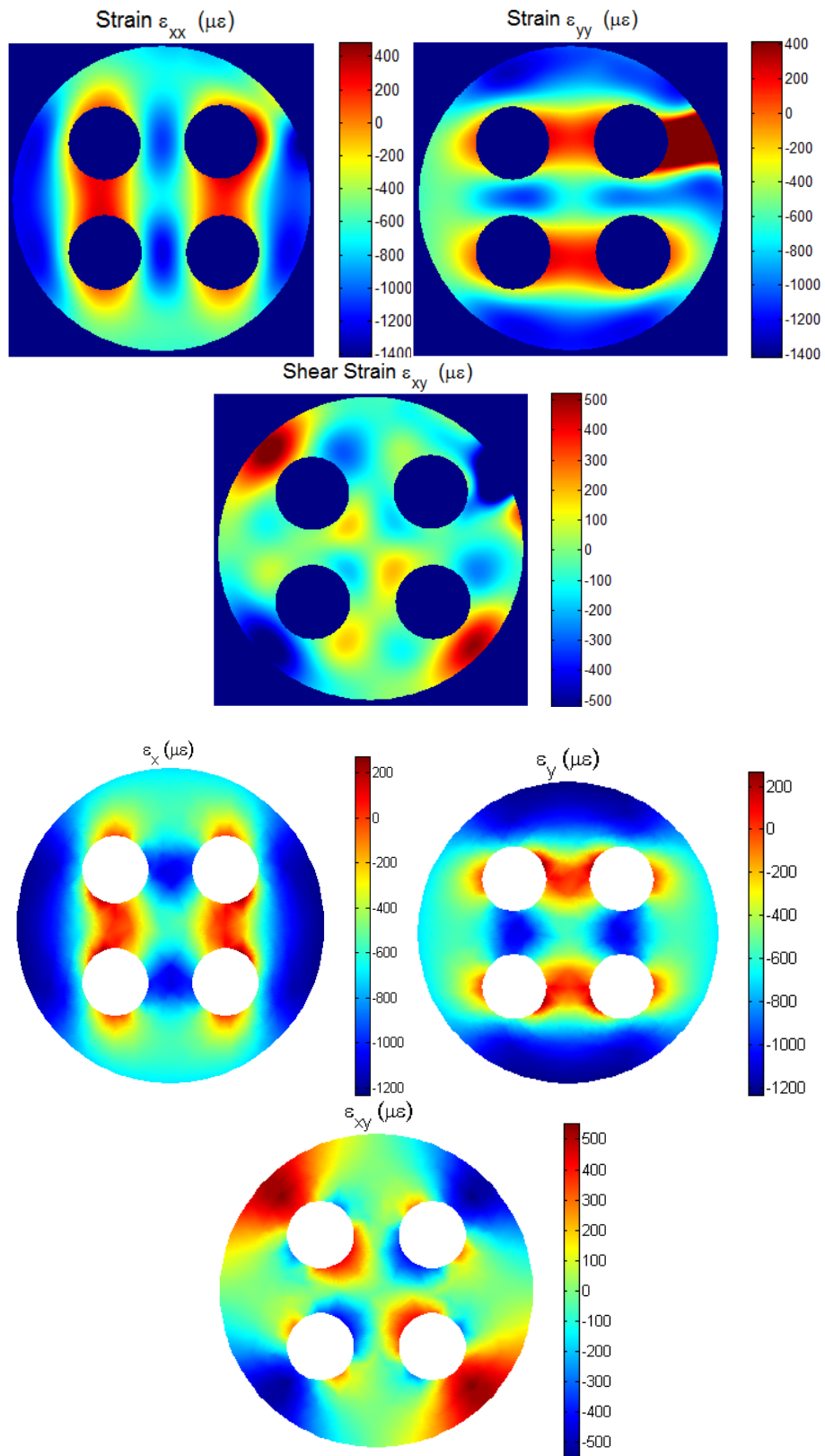


Figure 4-22. Experimental (above) and FEA (below) results for reinforced concrete on Day 3

4.5 Stress Development Prediction

As known, shrinkage influences the development of stress in concrete materials when internal and external constraints exist. Through the prediction of the stress, where and when cracks may occur can be predicted if tensile stress is available. Therefore, in this section, stress was predicted in both cases of free shrinkage and restrained shrinkage.

4.5.1 Free Shrinkage

The development of stress was modeled for the specimen under room temperature and RH80%. There were no external constraints in this case so that the specimen experienced shrinkage freely. Due to non-uniform shrinkage over the entire specimen, the stress should be distributed non-uniformly. The stresses developing on the surface with the grating were modeled as figure 4-23 with the plot of the stress distribution in polar coordinate from the center to the outer surface of the specimen and as figure 4-24 with the full-field maps of stresses in both x-y and polar coordinates for day 3 only. The radius stress was compressive near outer surface and was tensile stress in the middle. Also, the angular stress was larger than the radius stress. If cracks occur, they should initiate near the outer surface and propagate in radial direction at earlier time.

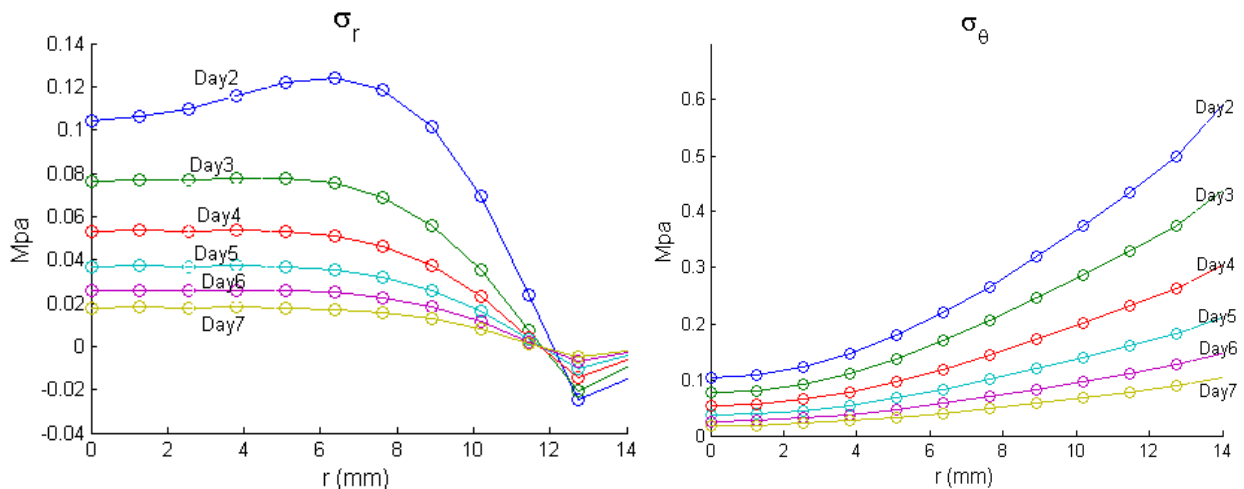


Figure 4-23. FEA result for stress development

From full-field maps in x-y coordinate, the normal stress distribution was different from the normal strain distribution.

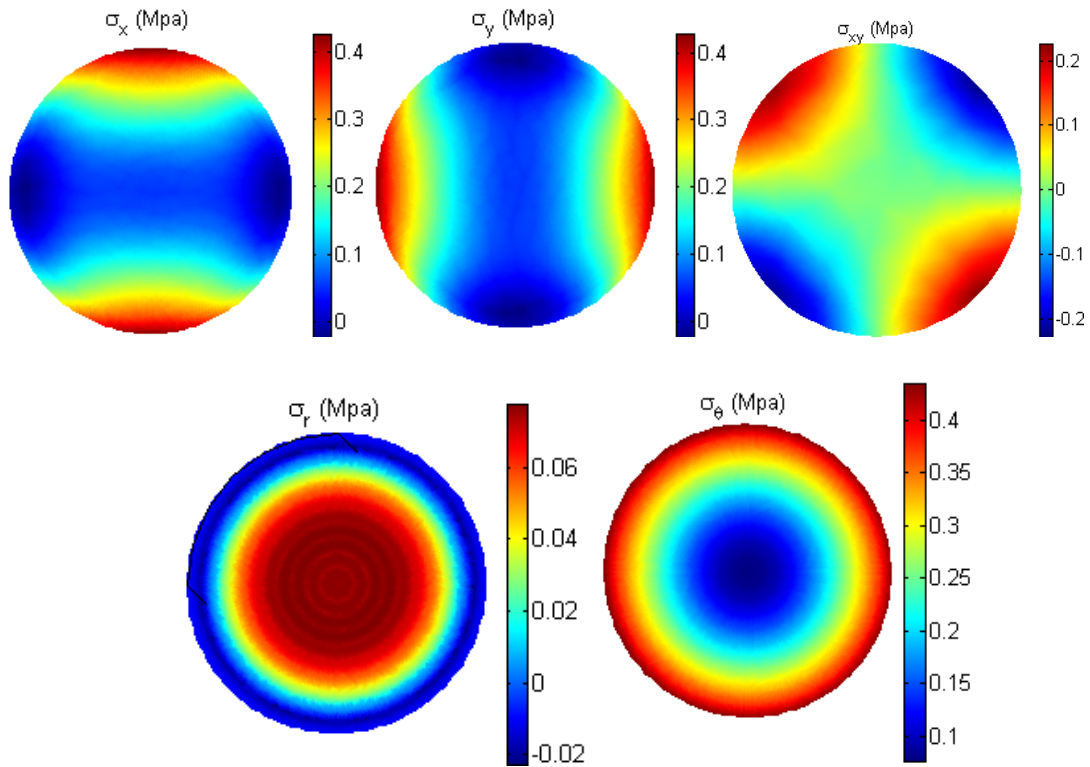


Figure 4-24. FEA results for full-field stress maps

It was also interesting to investigate the stress distribution in polar coordinate over the cross section of the specimen as figure 4-25. The FEA result shows the tensile stresses developed near the outer surface and the compressive stresses in the inner core of the specimen. This is due to the effect of internal constraints or the effect of stress self-equilibrating.

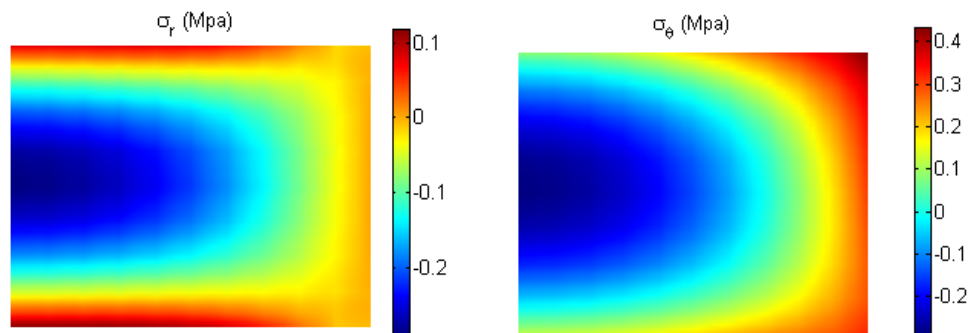


Figure 4-25. FEA results for stress maps over the cross section

4.5.2 Restrained Shrinkage

In this section, the ring test was used as the example of the restrained specimen. There were external constraints from the steel rod in the center so that the specimen did not experience shrinkage freely. The development of stress was modeled for the specimen under room temperature and RH60% in the ring test. The stresses developing on the surface with the grating were modeled as figure 4-26 with the plots of the stress distribution in polar coordinate from the inner surface to the outer surface of the specimen from day 2 to day 7 and as figure 4-27 with the full-field maps of stresses in both x-y and polar coordinates for day 3 only. The radius stress was tensile near the inner surface of the specimen and compressive in the rest area. The angular stress was always tensile stress and increased with time. Also, the angular stress was larger near the inner surface of the specimen. If cracks occur, they should initiate near the inner surface and in radial direction.

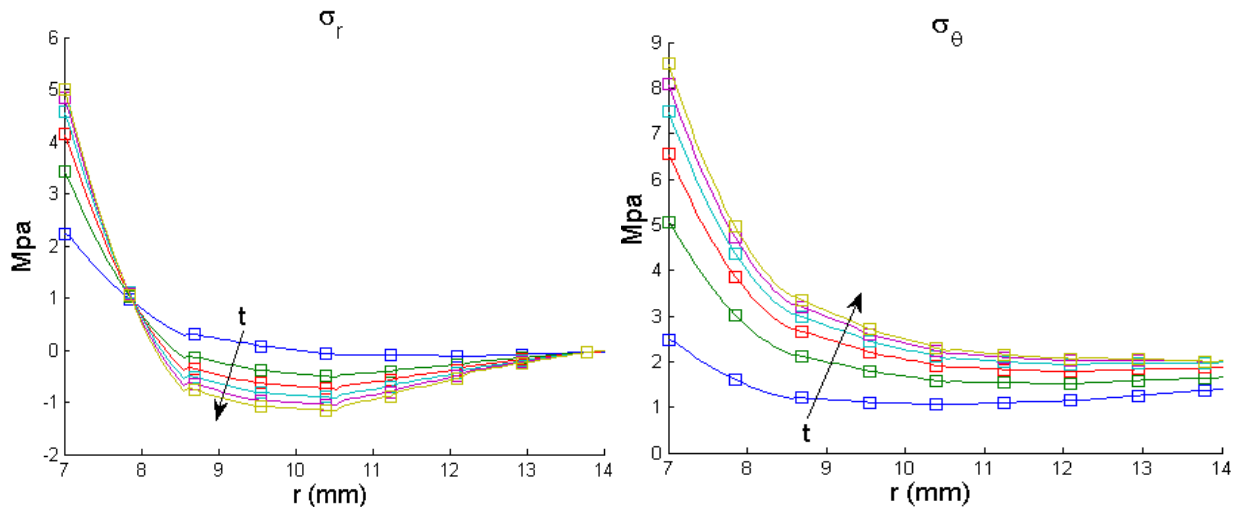


Figure 4-26. FEA results for stress development in the ring test of RH=60%

From the full-field maps, the shear stress distribution in x-y coordinate was quite similar to the shear strain distribution. However, the normal stress distribution was different from the normal strain distribution.

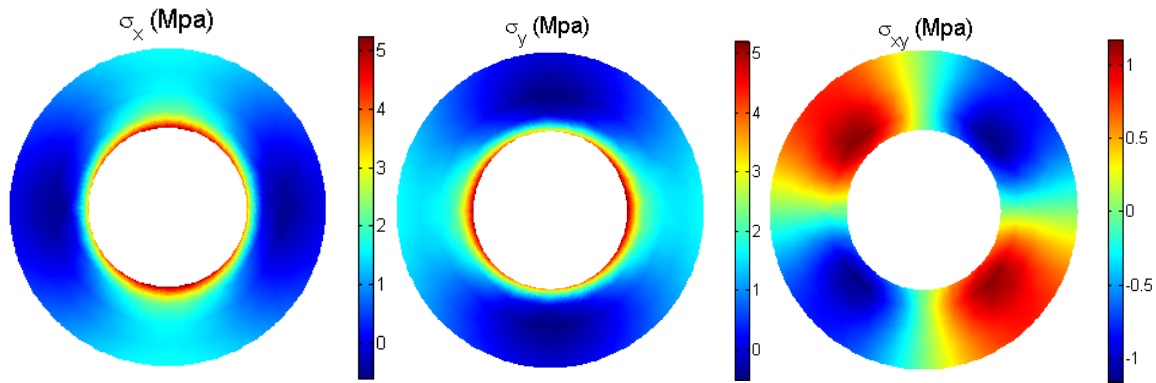


Figure 4-27. FEA results for full-field stress maps in ring test

The stress development was also predicted for the ring test under room temperature and RH0% because the cracks occurred in this experiment. The stresses developing on the surface with the grating were modeled as figure 4-28 with the plots of the stress distribution in polar coordinate from the inner surface to the outer surface of the specimen. But only the development with first day drying was shown because the cracks occurred during this period (between day 1 and day 2) in the experiment. In the experiment, the fact that the crack initiated near the outer surface and propagated in the radial direction was proved by this FEA.

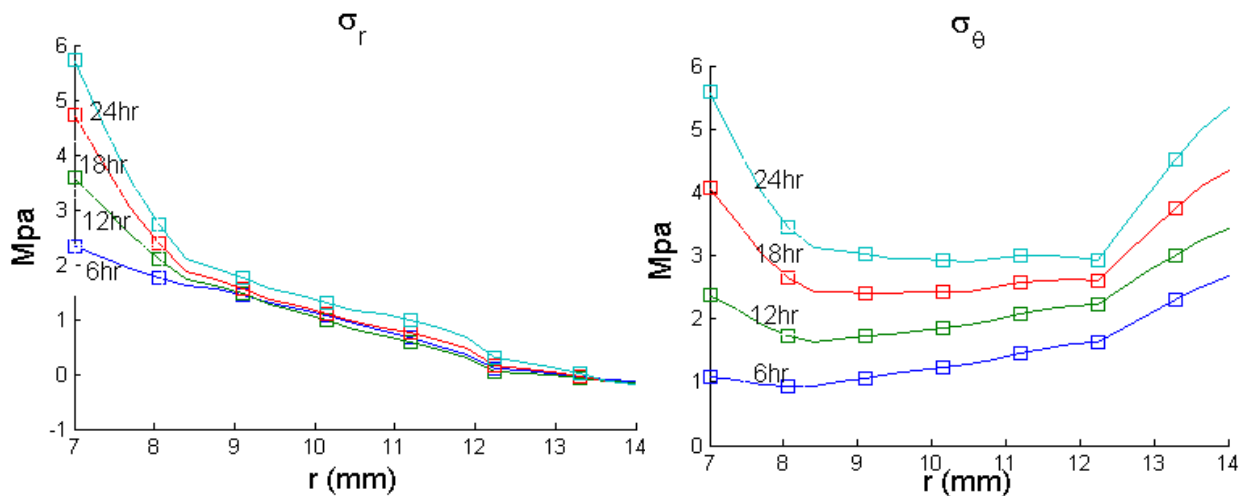


Figure 4-28. FEA results for stress development in the ring test of RH=0%

4.6 Results and Discussions

The inverse approach of combining FEA and optimization was used to determine the materials properties of shrinkage behavior in cement paste with $w/c=0.5$ under room temperature. The obtained materials properties were used to be the inputs in finite element model to predict the shrinkage behavior of cement paste in different conditions, such as different drying, geometric, or boundary conditions. The results from FEA and experiments match quite well in both the magnitude and the trend. Moreover, instead of modeling the shrinkage behavior in mortar or in the gravel test, the shrinkage behaviors in both the ring test and in the case of reinforced concrete were modeled using the composite models. The FEA results also show the good agreement with those from the experiments. Furthermore, the stress development in cement paste under drying was simulated using FEA. This can serve as the prediction of cracking occurrence if the tensile strength is given. To be summarized, the constructed FEA model with the obtained material properties is suitable for the simulation of shrinkage behavior in concrete materials according to the validation of the experimental results.

However, the material properties of shrinkage in concrete materials are very complicated and even unknown in many aspects. As a result, many things need to be considered and discussed here for constructing a more complete model in the future.

First, the material properties of cement paste should be dependent upon the composition, such as w/c ratio and cement type. The combination of the CRM and the inverse method can be applied to determine the shrinkage coefficient corresponding to their compositions. But the model needs to consider chemical shrinkage from hydration when w/c is below 0.4. That means the overall shrinkage cannot be modeled only by the phenomenon of moisture diffusion in the case of lower w/c ratio. The developed method combining CRM and the sealing of the specimen can be used to investigate the contribution of chemical shrinkage to total shrinkage or the ratio

between drying and chemical shrinkage. That will be useful in modeling the overall shrinkage in cement paste with lower w/c ratio.

Second, the shrinkage coefficient might not be constant, but dependent upon moisture content or relative humidity. But in the FEA model it was assumed constant for RH50~100%. This assumption was based on literature survey. Nevertheless, shrinkage coefficient may not be regarded as a constant for RH0 ~50%. Therefore, the complete understanding of shrinkage coefficient as a function of relative humidity is needed in the future so that the shrinkage behavior can be more accurately predicted for surrounding humidity below 50%.

The last but not the least, the materials properties may be temperature-dependent. However, the variation of temperature inside of the specimen was not considered in the FEA model due to the small size of the specimen. Hence, in the model the temperature is assumed constant over the entire specimen as surrounding temperature. In the future study, the further investigation of shrinkage coefficient as a function of temperature and the temperature variation inside of the specimen is needed so that the shrinkage behavior can be more accurately predicted for the specimen in larger size. The more thorough FEA model including heat transfer should be used later.

CHAPTER 5 CONCLUSIONS & FUTURE WORKS

5.1 Conclusions

The methodology of CRM has been successfully applied to the measurement of overall shrinkage which develops in concrete materials during drying and hydration, and also to the measurement of nondrying shrinkage which develops in sealed concrete materials. The procedure to prepare diffraction grating on the specimen, which is the key part in the CRM, has been well developed. The process of grating replication is simplified to the uttermost and thus is very repeatable. The use of RTV 6428 silicone rubber master grating provides the weak bonding between the master and the specimen gratings. This helps the separation of the specimen from the master substrate and prevents the damage on the specimen grating. Also, the RTV 6428 master gratings are easier to be replicated in better quality and with higher hardness than RTV 615. More importantly, the use of RTV 6428 reduces the possibility of the bubbles on the specimen grating. The experimental setup of PEMI II helped align the gratings and obtain the phase-shifted fringe patterns more precisely. The chamber setup provides stable drying conditions and is easy for other researchers to recreate.

There are many advantages in the CRM technique, such as non-destruction, non-intrusion high-sensitivity, and non-reinforcement. Although this technique is nondestructive, a thin layer of epoxy grating covered on the surface of the concrete specimen may prevent the diffusion of moisture. The result is different with the actual strain distribution of a natural concrete specimen without epoxy layer quantitatively. Digital image correlation (DIC) would be a technique to not avoid moisture exchange with the environments. However, this technique would not help when the shrinkage measurement is less than 500 microstrains, such as in the drying condition of high humidity, in the measurement of mortar with high aggregate quantity or in the chemical

shrinkage measurement under higher w/c ratio. Therefore, high sensitivity moiré interferometry is a more sound technique to investigate shrinkage behavior in concrete materials.

On the other hand, the automated fringe analysis system is a nice tool to help obtain the full-field displacement and strain information. This image processing method not only reduce much time in analyzing the data but also provided a way to compare between experimental and FEA results in the forms of the full-field maps.

Although CRM gave a fine piece of the experimental results, the materials properties of shrinkage were not able to be directly obtained from the 2-D in plane deformation measurement on the surface of the specimen. Hence, the 3-D FEA model was created under some assumptions to match the boundary conditions and the geometry of the specimen with the experiments. Due to the geometry of the specimen in the tests, the advantage of axisymmetry was used in the FEA model. Then an inverse approach was developed to fit the experimental results with the numerical results from FEA to determine the materials properties. The constructed FEA model was further validated through some other experiments. And the stress development can be simulated automatically in the FEA model. That is very useful in predicting when and where cracks could occur. Also, the deformation in the 3-D views or in the cross-section views can be demonstrated in the FEA model. This is for the investigation of shrinkage behavior inside of the specimen.

5.2 Future Works

Some works are brought out here for the future research in both the experimental and numerical aspects.

Experimentally, the more tests can be performed to explore the other influential factors on shrinkage, such as wind speed, admixture, and cement type, by using the CRM. Moreover, digital image correlation is a potential technique due to the recent improvements and

developments in optical equipments and image processing technique. Likewise, the FEA model can be created with the modified boundary condition on the speckled surface. The results from FEA can be compared with DIC results. Another advantage is that DIC can provide out-of-plane deformation information which cannot be obtained in moiré interferometry.

Numerically, chemical shrinkage as a function of w/c ratio, aggregate quantity, temperature and time can be modeled with the mathematical expression. But it requires more tests for abundant experimental data. Also, the composite model of cement paste and randomly-distributed sands can be created to simulate the shrinkage behavior in mortars. Mortars are considered as composite materials. Sands act like fibers, and cement pastes like matrix. But the size and the mechanical properties of sand particles need to be determined first. The simulating results can be compared with the results from the CRM.

APPENDIX
CRM MOIRE FRINGE PATTERNS AND FRINGE ANALAYIS RESULTS

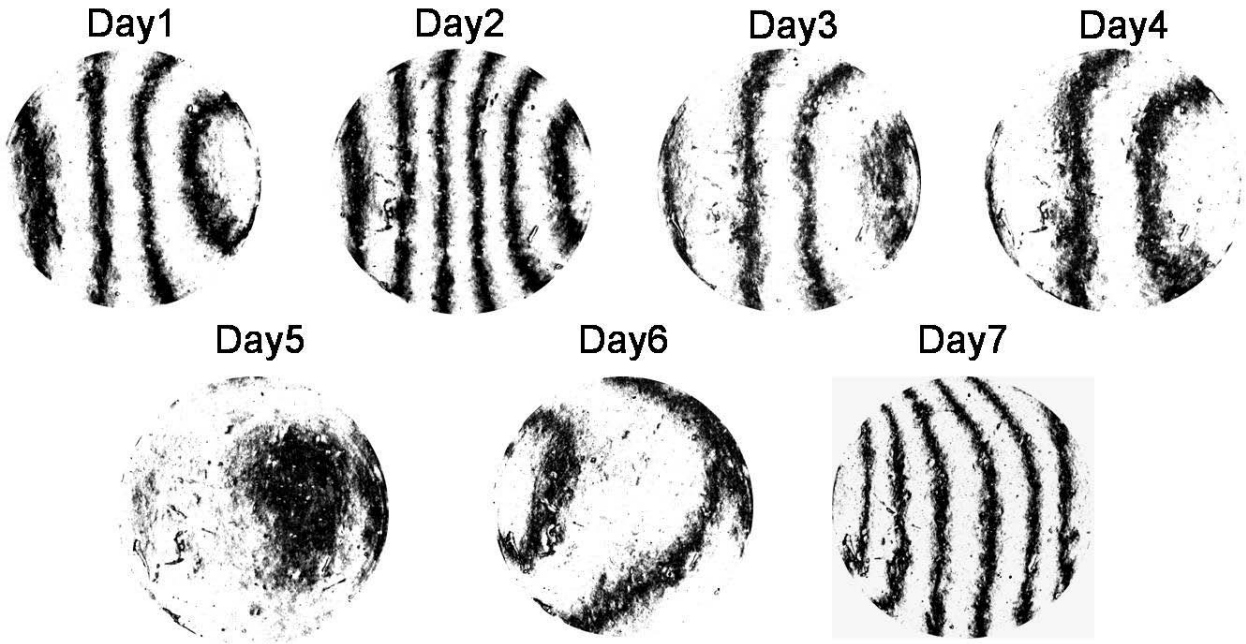


Figure A-1. U-field Moiré fringe patterns for $w/c=0.6$ in sealed condition

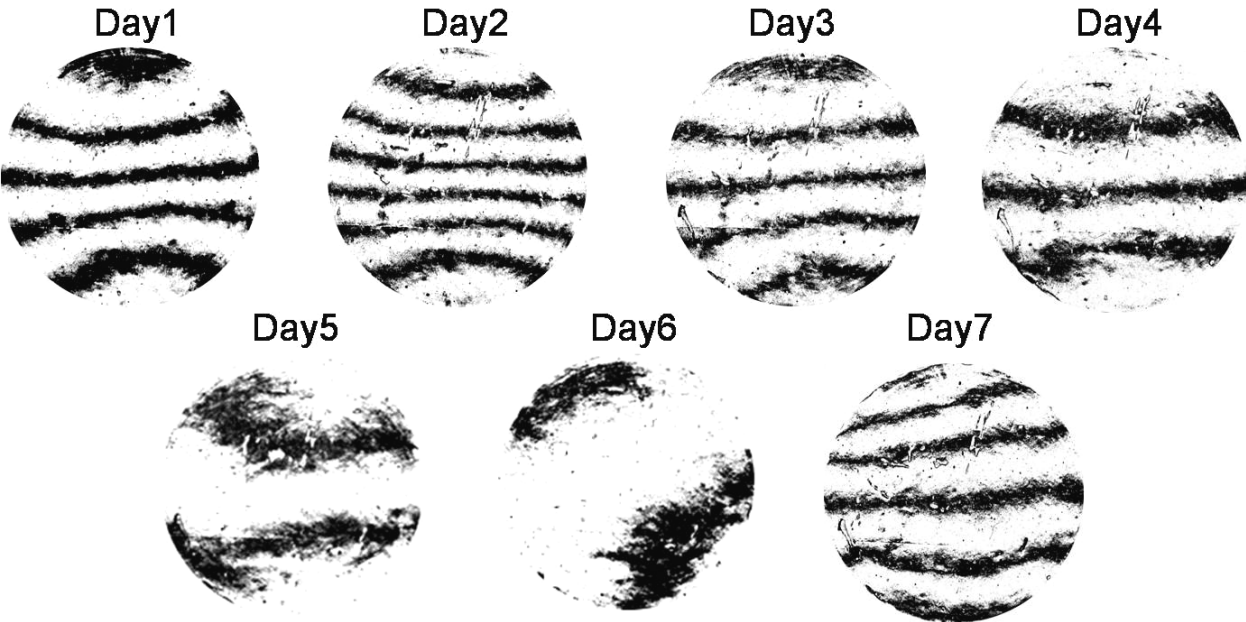


Figure A-2. V-field Moiré fringe patterns for $w/c=0.6$ in sealed condition

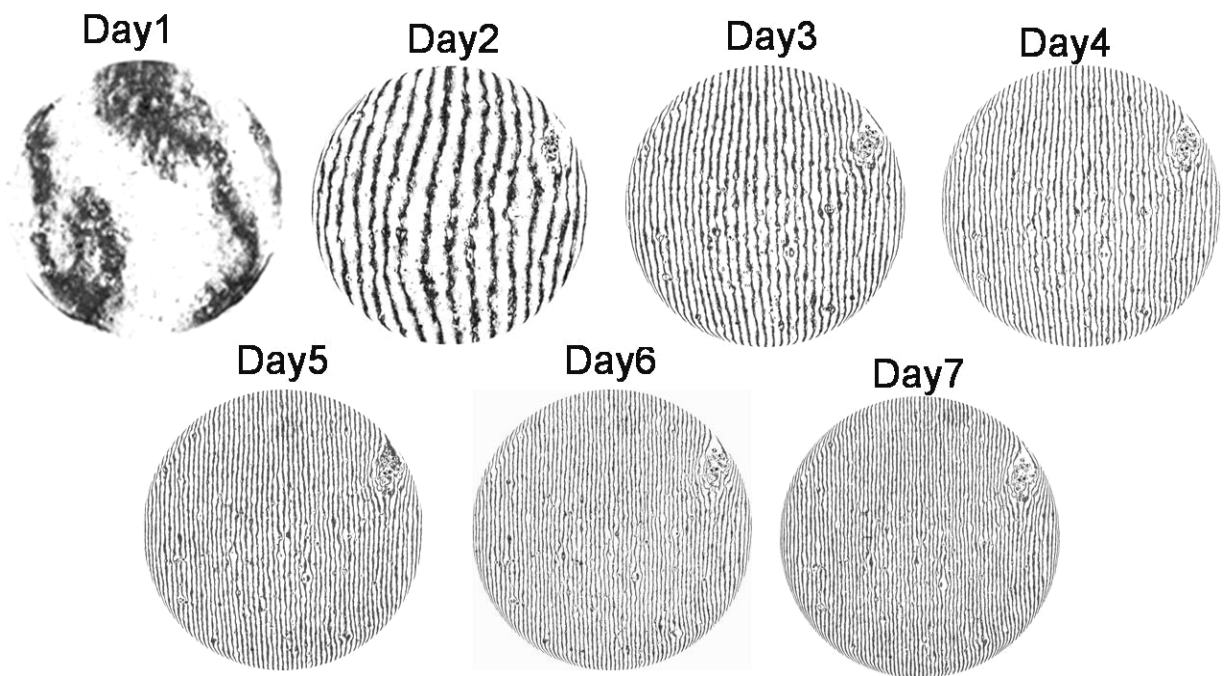


Figure A-3. U-field Moiré fringe patterns under 80% RH and 23°C

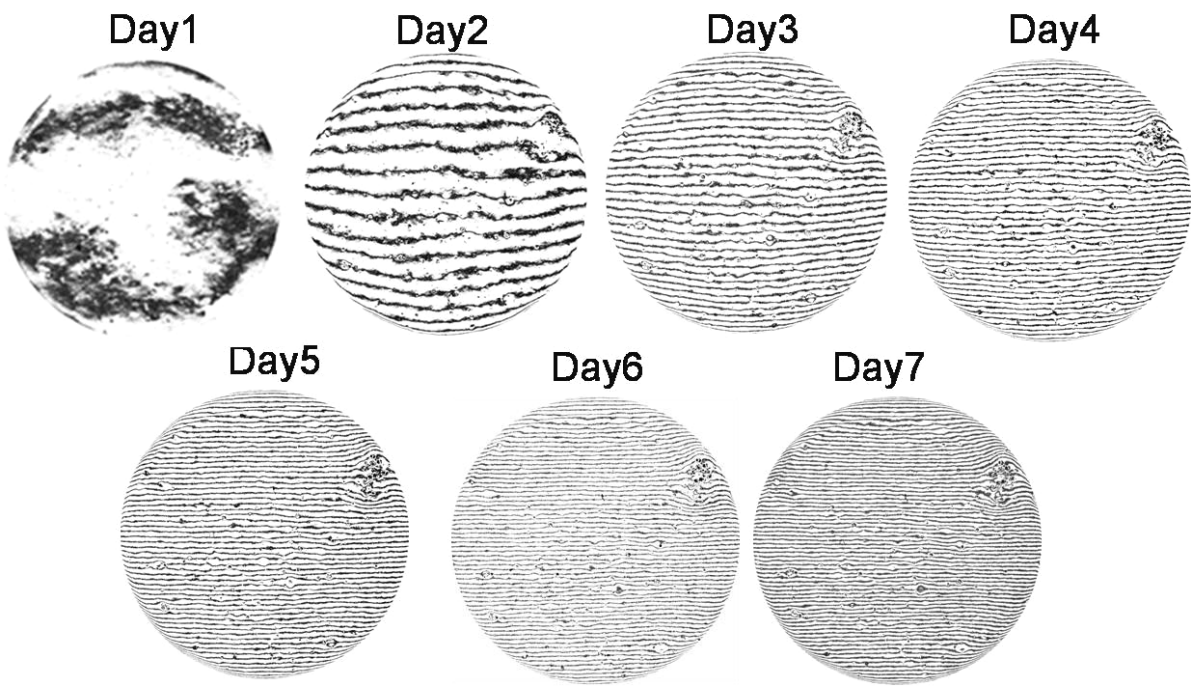


Figure A-4. V-field Moiré fringe patterns under 80% RH and 23°C

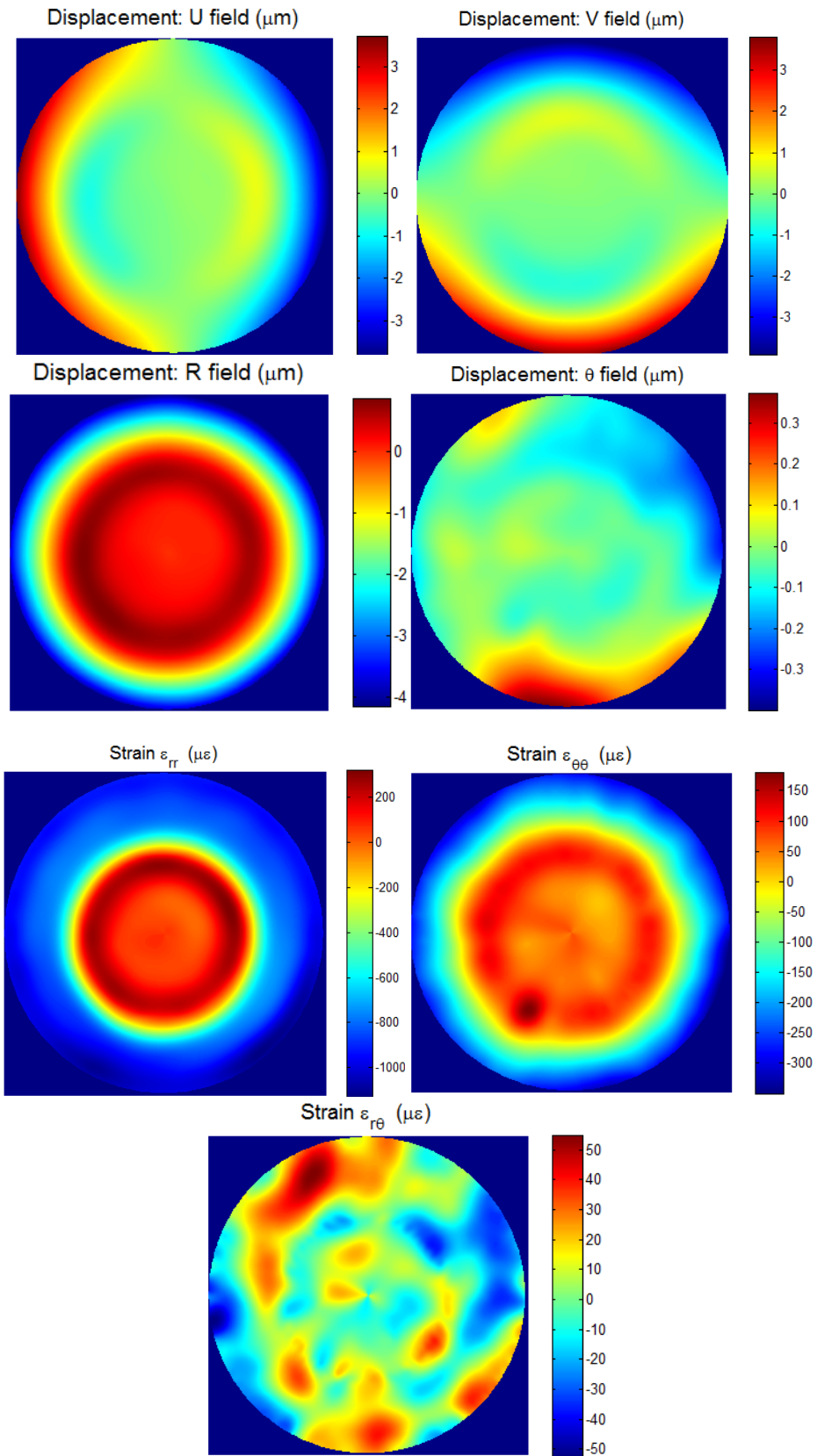


Figure A-5. Additional full-field maps for ring test on Day 2

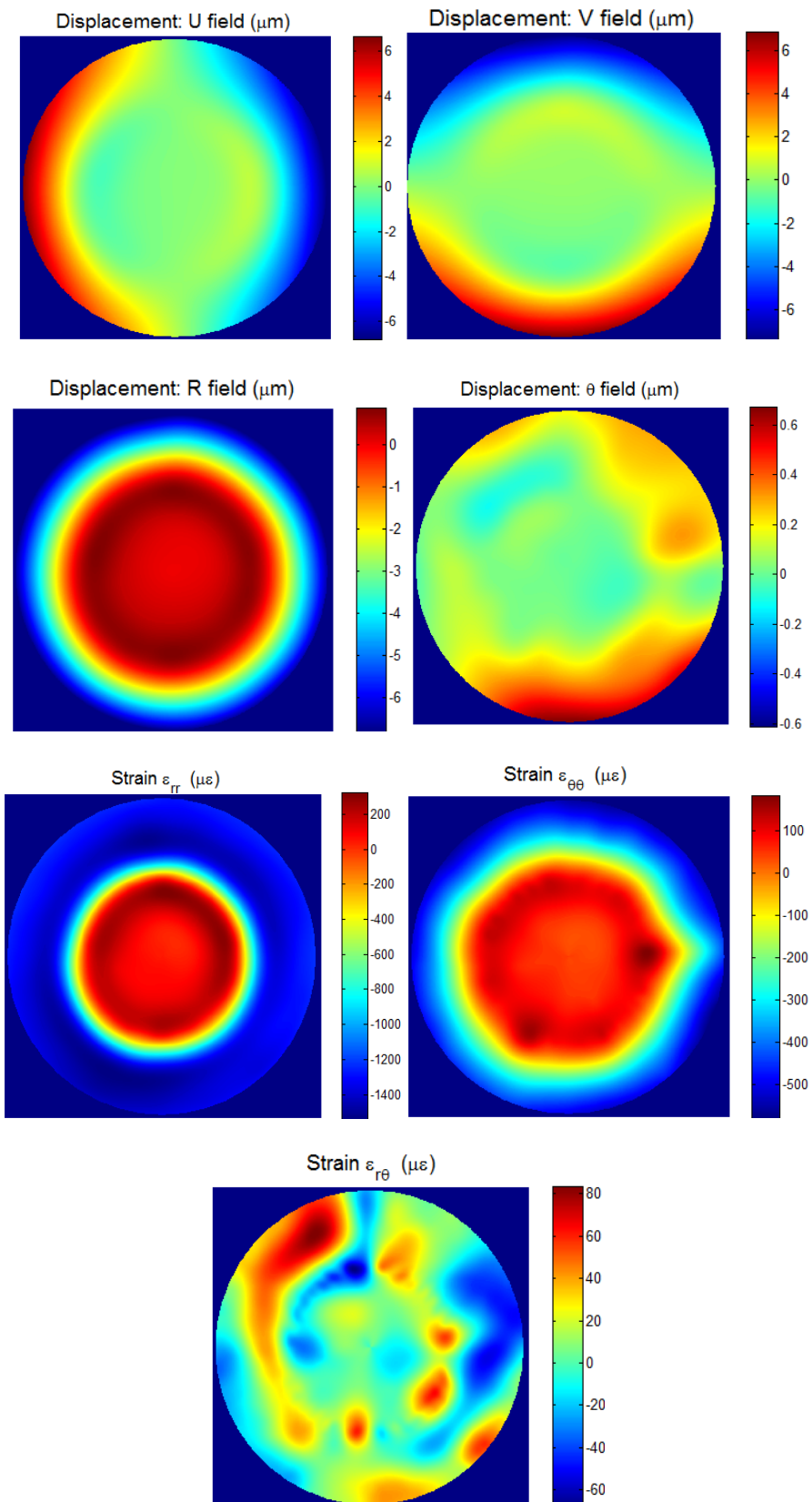


Figure A-6. Additional full-field maps for ring test on Day 3

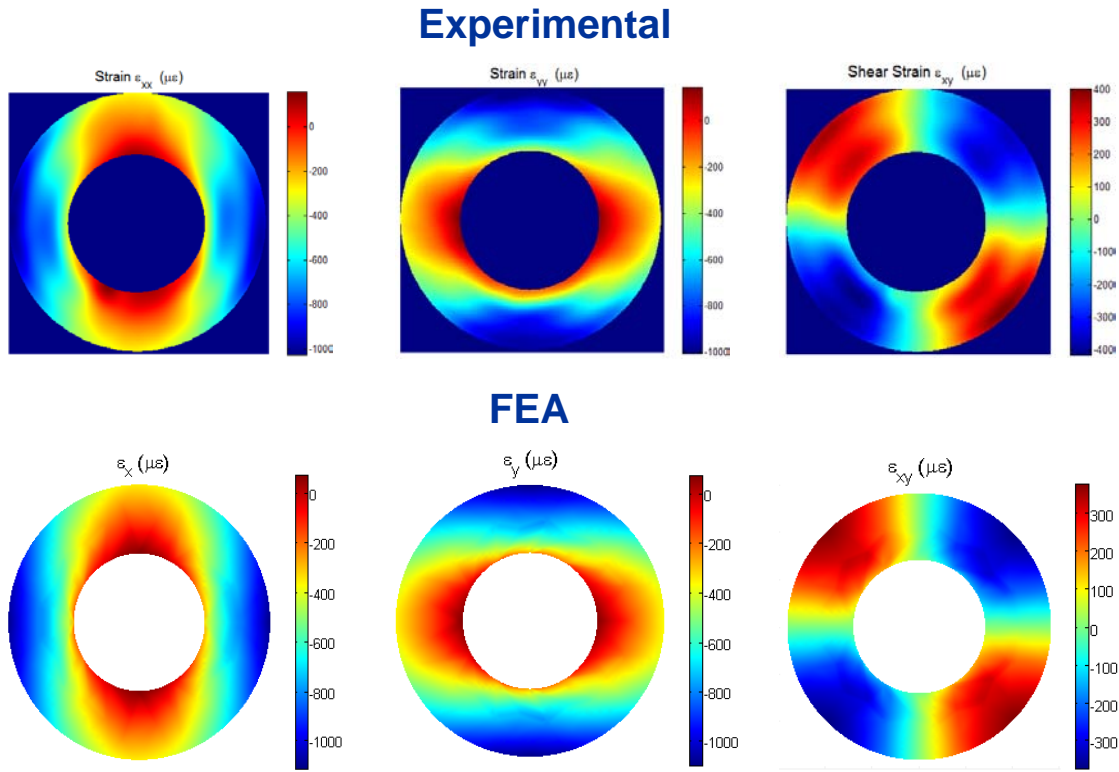


Figure A-7. The full-field strain maps of cement paste only in ring test on Day 2

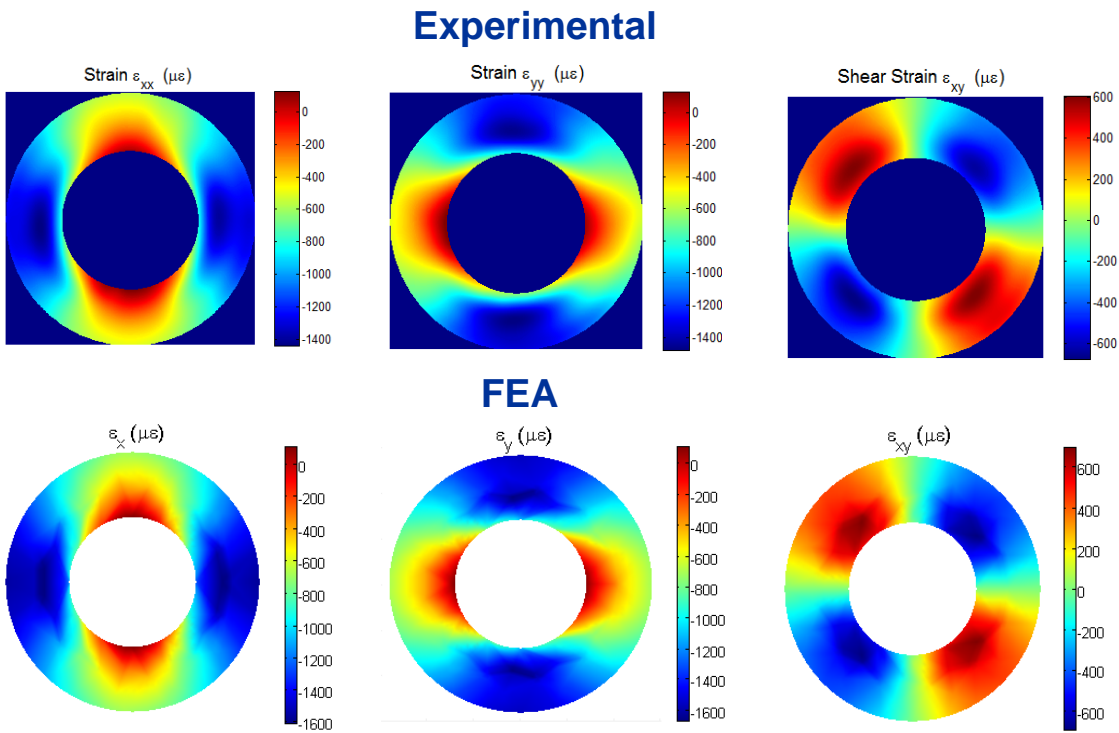


Figure A-8. The full-field strain maps of cement paste only in ring test on Day 3

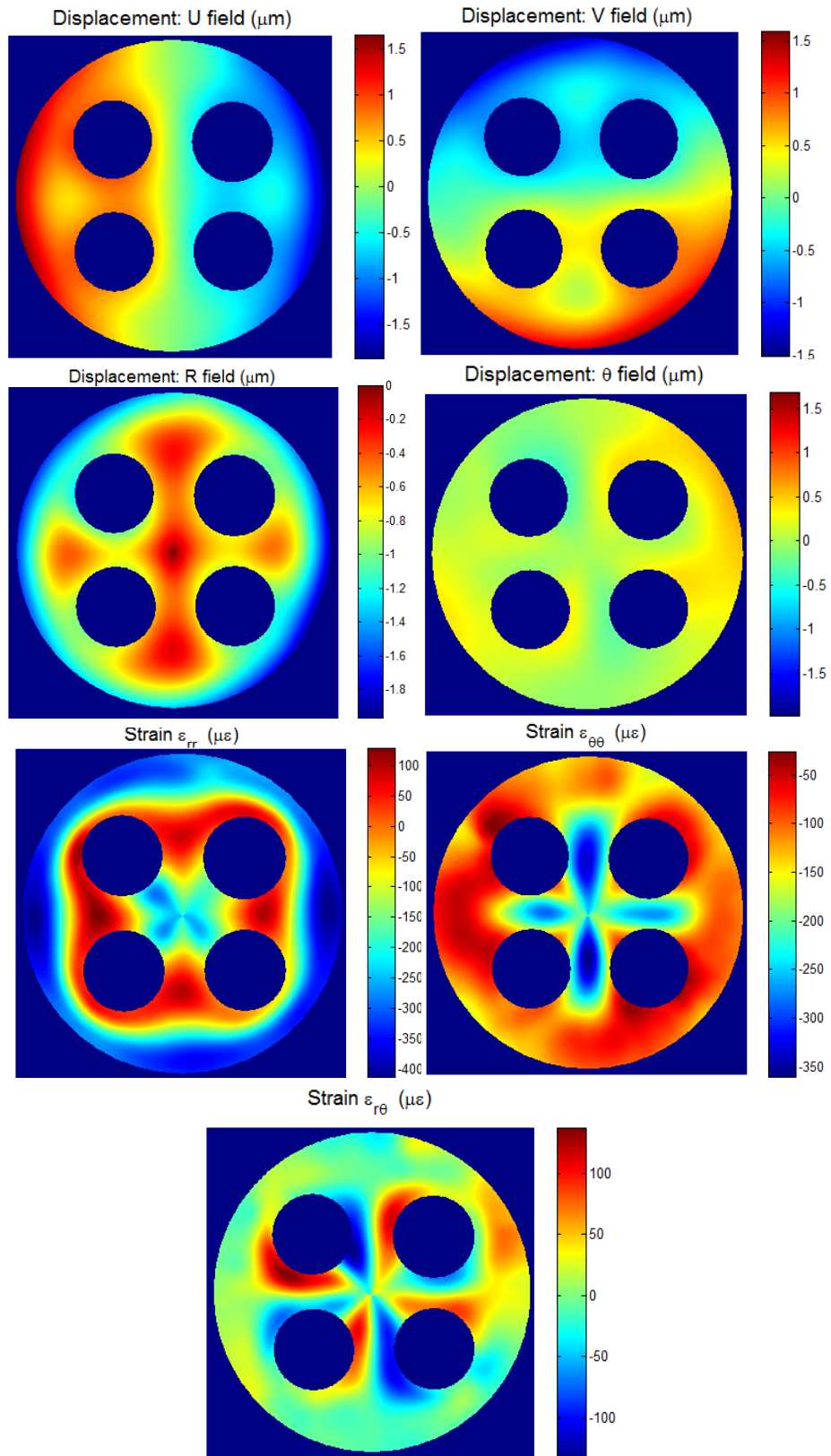


Figure A-9. Additional full-field strain maps for reinforced concrete on Day 2

LIST OF REFERENCES

1. ACI 224R-01 Control of cracking in concrete structures. ACI committee report.
2. Sa C., Benboudjema F, Thiery M, Sicard J (2008) Analysis of microcracking induced by differential drying shrinkage. *Cement and Concrete Composites* 30:947-956.
3. Mokarem DW (2002) Development of concrete shrinkage performance specification. Dissertation, Academic, Virginia Polytechnic Institute and State University, Civil and Environmental Engineering.
4. Mindess S, Young JF, Darwin D (2003) *Concrete*, Second Edition, Prentice Hall, New Jersey.
5. Mangat PS, Azari MM (1990) Plastic shrinkage of steel fiber reinforced concrete. *Materials and Structures* 23(135):186-195.
6. Shaeles CA, Hoover KC (1988) Influence of mix proportions on plastic shrinkage cracking in thin slabs. *ACI Mater J* 85:495-504.
7. Branch J, Hannant DJ, Mulheron M (2002) Factors affecting the plastic shrinkage cracking of high strength concrete. *Magazine of Concrete Research* 54(5):347-354.
8. Erlin B, William H (2004) Carbonation of concrete. *Concrete Construction-World of Concrete*. 49(8):22.
9. Fumiaki M, Yoshimichi A, Sumio S (2004) Calcium silicate structure and carbonation shrinkage of a tobermorite-based material. *Cement and Concrete Research* 34(7):1251-1257.
10. Shideler JJ (1963) Carbonation shrinkage of concrete masonry units. *Research and Development Laboratories Journal* 5(3):36-51.
11. Sakata K, Shimomura T (2004) Recent progress in research on and evaluation of concrete creep and shrinkage in Japan. *Journal of Advanced Concrete Technology* 2(2): 133–140.
12. Viktor V, Gintaris K, Darius B (2008) Shrinkage in reinforced concrete structure: a computational aspect. *Journal of Civil Engineering and Management* 14(1):49-60.
13. Jensen OM, Bentz DP, Lura P (2004) *Autogenous deformation of concrete*, American Concrete Institute, Michigan.
14. Zhang M.H, Tam CT, Leow MP (2003) Effect of water-to-cementitious materials ratio and silica fume on the autogenous shrinkage of concrete. *Cement and Concrete Research* 33(10):1687-1694.

15. Veronique BB, Pierre M, Abdelhafid M, Ahmed L, Noureddine R (2006) Autogenous deformations of cement pastes: Part II. w/c effects, micro-macro correlations, and threshold values. *Cement and Concrete Research* 36(1):123-136.
16. Pierre M, Veronique BB, Ahmed L, Abdelhafid K (2006) Autogenous deformations of cement pastes: Part I. temperature effects at early age and micro-macro correlations. *Cement and Concrete Research* 36(1):110-122.
17. Kohno K, Okmoto T, Iskawa Y, Sibata T, Mori H (1999) Effects of artificial lightweight aggregate on autogenous shrinkage of concrete. *Cement and Concrete Research* 29(4):611-614.
18. Tazawa E, Miyazawa S (1997) Influence of constituents and composition on autogenous shrinkage cementitious materials. *Magazine of Concrete Research* 49(178):15-22.
19. Tazawa E, Miyazawa S (1995) Influence of cement and admixture on autogenous shrinkage of cement paste. *Cement and Concrete Research* 25(2):281-287.
20. Millard MJ, Kurtis KE (2008) Effects of lithium nitrate admixture on early-age cement hydration. *Cement and Concrete Research* 38(4):500-510.
21. Bhal NS, Mital MK (1996) Effect of relative humidity on creep and shrinkage of concrete. *The Indian Concrete Journal* 21-27.
22. Masami S, Shuichi S (1987) Effect of wind action on early shrinkage of concrete. *Proceedings of The Japan Congress on Materials Research* 161-170.
23. Azenha M, Maekawa K, Ishida T (2007) Drying of induced moisture losses from mortar to the environment. Part I: experimental research. *Materials and Structures* 40:801-811.
24. Barr B, Hoseinian SB, Beygi M.A (2003) Shrinkage of concrete stored in natural environments. *Cement and Concrete Composites* 25(1):19-29.
25. Alshamsi, M., Imran, H.D., Bushlaibi, A.(2005) Drying Shrinkage of Concrete Samples Exposed to Extreme Hot Weather. *Proceedings of the International Conference on Cement Combinations for Durable Concrete* 357-362.
26. ACI 209.1R-05 Report on Factors Affecting Shrinkage and Creep of Hardened Concrete.
27. Bissonnette B, Pierre P, Pigeon M (1999) Influence of key parameters on drying shrinkage of cementitious materials. *Cement and Concrete Research* 29:1655-1622.
28. Barr B, Hoseinian SB, Beygi MA (1984) Evaporation of water from fresh mortar and concrete at different environmental conditions. *ACI Journal* 81(42):560-565.
29. Almudaiheem JA, Hansen W (1987) Effect of specimen size and shape on drying shrinkage of concrete. *ACI Materials Journal* 84(2):130-135.

30. Saleh AA, Rajeh ZA (2006) Effects of drying conditions, admixtures and specimen size on shrinkage strains. *Cement and Concrete Research* 36:1985-1991.
31. Zhou M, Wang J, Zhu L (2008) Effects of manufactured-sand on dry shrinkage and creep of high-strength concrete. *Journal Wuhan University of Technology, Materials Science Edition* 23(2):249-253.
32. ASTM C157/C157M-06 Standard Test Method for Length Change of Hardened Hydraulic-Cement Mortar and Concrete.
33. Mokarem DW, Weyers RE, Lane DS (2005) Development of a shrinkage performance specifications and prediction model analysis for supplemental cementitious material concrete mixtures. *Cement and Concrete Research* 35:918-925.
34. Kim JK, Lee CS (1998) Prediction of drying shrinkage in concrete. *Cement and Concrete Research* 28:985-994.
35. Yang Y, Sato R, Kawai K (2005) Autogenous shrinkage of high strength concrete containing silica fume under drying at early ages. *Cement and Concrete Research* 35:449-456.
36. Habel WR, Hofmann D, Hillemeier B (1997) Deformation measurements of mortars at early ages and of large concrete components on site by means of embedded fiber-optic microstrain sensors. *Cement and Concrete Composites* 19:81-102.
37. Volker S, Evelyn S, Thomas K (2004) Experimental investigation into early age shrinkage of cement paste by using fibre bragg gratings. *Cement and Concrete Composites* 26:473-479.
38. Allan CL, Childs PA, Berndt R, Macken T, Peng GD, Gowripalan N (2007) Simultaneous measurement of shrinkage and temperature of reactive powder concrete at early-age using fibre bragg grating sensors. *Cement and Concrete Composites*, 29:490-497.
39. Lura P, Jensen OM (2005) Measuring techniques for autogeneous strain of cement paste. *Proc Knud Hojgaard Conference on Advanced Cement-Based Materials*, Lyngby, Denmark, June.
40. Pease BJ, Hossain AB, Weiss WJ (2004) Quantifying volume change stress development and cracking due to self-desiccation, In *ACISP-220: Autogenous deformation of concrete*, American Concrete Institute, Farmington Hills, Mich.
41. Sant G, Lura P, Weiss J (2006) Measurement of volume change in cementitious materials at early age-review of testing protocols and interpretation of results. *Transportation Research Record* 197:21-29.

42. Avril S, Ferrier E, Vautrin A, Hamelin P, Surrel Y (2004) A full-field optical method for the experimental analysis of reinforced concrete beams repaired with composites. *Composites, Part A* 35:873-884.
43. Avril S, Vautrin A, Hamelin P, Surrel Y (2005) A multi-scale approach for crack width prediction in reinforced beams repaired with composites. *Composites Science and Technology* 65:445-455.
44. Avril S, Vautrin A, Surrel Y (2004) Grid method: application to the characterization of cracks. *Experimental Mechanics* 44(1):37-43.
45. Cao SY, Chen JF, Pan JW, Sun N (2007) EPSI measurement of bond-slip relationships of FRP-concrete interface. *Journal of Composites for Construction* 11(2):150-160.
46. Chen J, Jin G, Meng L (2007) Application of digital correlation method to structure inspection. *Tsinghua Science and Technology* 12(3):237-243.
47. He S, Feng Z, Rowlands RE (1997) Fracture process zone analysis of concrete using moiré interferometry. *Experimental Mechanics* 37(3):367-373.
48. Yu CT, Kobayashi AS, Hawkins NM (1993) Energy-dissipation mechanisms associated with rapid fracture of concrete. *Experimental Mechanics* 37(5):205-211.
49. Yilmazturk F, Kulur S, Pekmezci BY (2003) Measurement of shrinkage in concrete samples using digital photogrammetric methods. *The International Archives of the Photogrammetry, Remote Sensing and Spatial Information Sciences* 34 Part XXX.
50. Neubeuer CM, Bergstrom TB, Sujata K, XI Y, Gaboczcie EJ, Jennings HM (1997) Drying shrinkage of cement paste as measured in an environmental scanning electron microscope and comparison with microstructural models. *Journal of Material Science* 32:6415-6427.
51. Bazant ZP, Najjar LJ (1971) Drying of concrete as a nonlinear diffusion problem. *Cement and Concrete Research* 1(1):461-73.
52. Wittmann FH (1977) The fundamentals of a model for the description of concrete characteristics. *Schriftenreihe Deutscher Ausschuss für Stahlbeton, Heft 290*, Berlin:43-101.
53. Wittmann X, Sadouki H, Wittmann FH (1989) Numerical evaluation of drying test data. *Transactions 10th Int. Conf. on Struct. Mech. in Reactor Technology, SMiRT-10*, R:71-89.
54. Bazant ZP, Najjar LJ (1972) Nonlinear water diffusion in nonsaturated concrete. *Materials and Structures* 5(25):3-20.
55. Sakata K (1983) A study on moisture diffusion in drying and drying shrinkage of concrete. *Cement and Concrete Research* 13(2):216-224.

56. Ayano T, Wittmann FH (2002) Drying, moisture distribution, and shrinkage of cement-based materials. *Materials and Structures* 35:134-1140.
57. Xi Y, Bazant ZP, Jennings HM (1994) Moisture diffusion in cementitious materials-adsorption isotherms. *Advanced Cement Based Materials* 1:248-257.
58. Xi Y, Bazant ZP, Molina L, Jennings HM (1994) Moisture diffusion in cementitious materials-moisture capacity and diffusivity. *Advanced Cement Based Materials* 1:258-266.
59. Quyang Z., Wan B (2008) Modeling of moisture diffusion in FRP strengthened concrete specimens. *Journal of Composites for Construction* 2(4):426-434.
60. West PR, Holmes N (2005) Predicting moisture movement during the drying of concrete floors using finite elements. *Construction and Building Materials* 19:674-681.
61. Jang C, Han B (2009) Analytical solutions of gas transport problems in inorganic/organic hybrid structures for gas barrier applications. *Journal of Applied Physics* 105(093532).
62. Sheban MA, Ababneh AN, Fulton SR (2006) Numerical simulation of moisture diffusion in concrete. *Joint International Conference on Computing and Decision Making in Civil and Building Engineering*, June14-16, 1015-1024.
63. Persson B (1997) Self-desiccation and its importance in concrete technology. *Materials and Structures* 30:293-305.
64. Yang QB, Zhang SQ (2004) Self-desiccation mechanism of high-performance concrete. *Journal of Zhejiang University Science* 5(12):1517-1523.
65. Jiang Z, Sun Z, Wang P (2006) Internal relative humidity distribution in high-performance cement paste due to moisture diffusion and self-desiccation. *Cement and Concrete Research* 36:320-325.
66. Kim JK, Lee CS (1999) Moisture diffusion of concrete considering self-desiccation at early ages. *Cement and Concrete Research* .29:1921-1927.
67. Bhal NS, Mital MK (1996) Effect of relative humidity on creep and shrinkage of concrete. *Indian Concrete Journal* 70(1):21–27.
68. Mehta PK, Monteiro PJ (1986) *Concrete Structure, Properties, and Materials*. Prentice Hall, New Jersey.
69. Bazant ZP (1995) Creep and shrinkage prediction model for analysis and design of concrete structures—model B3. *Materials and Structures* 28:357– 365.
70. Gardner NJ, Lockman MJ (2001) Design provisions for drying shrinkage and creep of normal-strength concrete. *ACI Materials Journal* 98:159– 167.

71. Alvaredo AM, Helbling A, Wittmann FH (1995) Shrinkage data of drying concrete. Building Materials Report No.4.
72. Sakata K (1993) Prediction of concrete creep and shrinkage, creep and shrinkage of concrete. Proceedings of the Fifth International RILEM Symposium, Barcelona, Spain, September 6–9, 649– 654.
73. Goel R, Kumar R, Paul DK (2007) Comparative study of various creep and shrinkage prediction models for concrete. Journal of Materials in Civil Engineering 19(3):249–260.
74. Eguchi K, Teranishi K (2005) Prediction equation of drying shrinkage of concrete based on composite model. Cement and Concrete research 35:483–493.
75. Gawin D, Pesavento F, Schrefler BA (2006) Hygro-thermo-chemo-mechanical modeling of concrete at early ages and beyond. Part II: shrinkage and creep of concrete. International Journal for Numerical Methods in Engineering 67:332–363.
76. Wang Z, Cardenas-Garcia J., Han B (2005) Inverse method to determine elastic constants using a circular disc and moiré interferometry. Experimental Mechanics 45(1):27–34.
77. Cardenas-Garcia JF, Shabana YM (2005) An inverse problem finite-element-method-based approach to the hole drilling method in photoelasticity. Proceedings of the 2005 SEM Conference and Exhibition on Experimental and Applied Mechanics 33.
78. Cardenas-Garcia JF, Ekwaro-Osire S, Berg JM, Wilson WH (2005) Non-linear least-squares solution to the Moiré hole method problem in orthotropic materials. Part I. residual stresses. Experimental Mechanics 45(1):301–313.
79. Cardenas-Garcia JF, Ekwaro-Osire S, Berg JM, Wilson WH (2005) Non-linear Least-squares solution to the Moire´ hole method problem in orthotropic materials. Part II. Material elastic constants. Experimental Mechanics 45(4):314–324.
80. Cho S, Cardenas-Garcia JF, Chasiotis I (2005) Measurement of nano displacements and elastic properties of MEMS via the microscopic hole method. Sensors and Actuators A120:136-171.
81. Grediac M (2004) The use of full-field measurement methods in composite material characterization: interest and limitations. Compos: Part A 35:751–761.
82. Fu G, Moosa AG (2002) An optical approach to structural displacement measurement and its application. Journal of Engineering Mechanics 128(5):511–520.
83. Chock JMK, Kapania RK (2003) Load updating for finite element models. AIAA Journal 41(9):1667–1673.
84. Sanayei M, Saletnik MJ (1996) Parameter estimation of structures from static strain measurements. I. Formulation. Journal of Structural Engineering, ASCE 122(5):555–562.

85. Shkarayev S, Krashantisa R, Tessler A (2001) An inverse interpolation method utilizing in-flight strain measurements for determining loads and structural response of aerospace vehicles. 3rd International Workshop on Structural Health Monitoring, September 12–14, Stanford, California.
86. Padmanabhan S, Huner JP, Kumar AV, Ifju PG (2006) Load and boundary condition calibration using full-field strain measurement. *Experimental Mechanics* 46:569–578.
87. Post D, Han, B, Ifju PG (1994) *High Sensitivity Moiré: Experimental Analysis for Mechanics and Materials*, Springer-Verlag, New York.
88. Dally JW, Riley WF (1997) *Experimental Stress Analysis Fourth Edition*, College House Enterprise, Knoxville.
89. Han B, Post D, Kumar AV, Ifju PG (2006) Moire interferometry for engineering mechanics: current practices and future developments. *Journal of Strain Analysis* 36(1):101-116.
90. Ifju PG, Masters JE, Jackson WC (1995) The use of moiré interferometry as an aid to standard test-method development for textile composite materials. *Composites Science and Technology* 53:155-163.
91. Ifju PG, Kilday BC, Niu X, Liu SC (1999) A novel method to measure residual stresses in laminated composites. *Journal of Composite Materials* 33(16):1511-1524.
92. Ifju PG, Niu X, Kilday BC, Liu SC, Ettinger SM (2000) Residual strain measurement in composites using the cure-reference method. *J. Exp. Mechanics* 40:22-30.
93. Strickland NM, Yin W, Ifju PG (2007) Residual strain measurement analysis of woven composites using phase shifting. *Proceedings of the 2007 SEM annual Conference and Exposition on Experimental and Applied Mechanics* 3:1855-1860.
94. Yin W, Strickland NM, Ifju PG (2008) Residual strain measurement and residual stress prediction of woven composites. *11th International Congress and Exhibition on Experimental and Applied Mechanics* 2:687-694.
95. Liu SC (1999) Residual stress characterization for laminated composites. Ph.D. Dissertation, University of Florida, Gainesville, Florida.
96. Huntley JM (1998) Automated fringe pattern analysis in experimental mechanics: a review. *Journal of Strain Analysis* 33(2):105-125.
97. Speriatu ML (2005) Temperature dependent mechanical properties of composite materials and uncertainties in Experimental Measurement. Dissertation, Academic, UF, Mechanical and Aerospace Engineering.
98. Gonzalez RC, Woods RE, Eddins SL (2003) *Digital Image Processing Using MATLAB*. Prentice Hall, New York.

99. Ghiglia DC, Pritt MD (1998) Two-Dimensional Phase Unwrapping: Theory, Algorithm, and Software, Wiley, New York.
100. Duchon J Splines (1976) Minimizing rotation-invariant semi-norms in Sobolev spaces. In Constructive Theory of Functions of Several Variables 1:85-100 (Springer Berlin / Heidelberg).
101. Donato G, Belongie S. (2002) Approximate thin plate spline mappings. Computer Vision - Eccv Pt Iii 2002, 2352: 21-31.
102. Barrodale, I., et al. (1993) Warping Digital Images Using Thin Plate Splines. Pattern Recognition 26(2):375-376.
103. Guo, H. Jiang J.Y., Zhang L.M. (2004) Building a 3D morphable face model by using thin plate splines for face reconstruction. Advances in Biometric Person Authentication Proceedings 3338:258-267.
104. Lewis G (1977) Humidity fixed points of binary saturated aqueous solutions. Journal of Research of the National Bureau Standard 81A(1):89-96.
105. Comite Euro-International du Beton (1993) CEB-FIP Model Code 1990. 68–69.

BIOGRAPHICAL SKETCH

Tzu-Chau Chen, from Taipei, Taiwan, was a doctoral student in Mechanical Engineering at University of Florida. He completed his undergraduate study in mechanical engineering at National Taiwan University in 2000. After receiving his bachelor's degree, Chen performed his military service in R.O.C Army until March, 2002. In August, 2003, Chen went to UCLA and majored in MEMS. He received his master's degree in spring, 2005. In fall, 2005, he transferred to University of Florida to pursue his doctoral degree, specializing in experimental stress analysis. Chen's research interests include moiré interferometry, digital image correlation, concrete & composite materials, and finite element analysis.